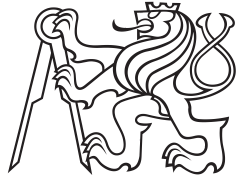


Doctoral Thesis



Czech
Technical
University
in Prague

Faculty of Mechanical Engineering
Department of Fluid Dynamics and Thermodynamics

Aeroacoustic Characteristics of Boundary-Layer Regimes

Ing. Jakub Suchý

Study Program: Mechanical Engineering
Study Field: Thermomechanics and Fluid Mechanics

Supervisors:
doc. Ing. Tomáš Hyhlík, Ph.D. (2021–),
prof. Ing. Jiří Nožička, CSc. (2016–2021)

Prague, November 2023

Acknowledgements

First and foremost, I would like to express my gratitude to the late Professor Jiří Nožička for his guidance and valuable recommendations during the initial and research stages of this work. I would also like to thank Associate Professor Tomáš Hyhlík for his support and advice during the final stages of preparing this thesis. Many thanks also go to my colleagues from the Department of Fluid Dynamics and Thermodynamics for their help and support, especially during the experimental work.

Financial support for the research was provided by the internal grant agency of Czech Technical University in Prague: SGS18/125/OHK2/2T/12 (*Examination of a possibility using the wind tunnel of the department 12112 for aeroacoustic measurement*), SGS20/112/OHK2/2T/12 (*Experimental and numerical investigation in applied fluid mechanics 2020-2021*), and SGS22/099/OHK2/2T/12 (*Experimental and numerical research in applied fluid mechanics 2022-2023*).

Declaration

I hereby declare that this work is entirely my own work and that I have cited all sources I have used.

Prague, November 4, 2023

Prohlašuji, že jsem předloženou práci vypracoval samostatně, a že jsem uvedl veškerou použitou literaturu.

V Praze 4. listopadu 2023

Abstract

The aeroacoustics of the boundary layer is a relatively new field of study that considers the boundary layer as a source of sound. This thesis aims to extend the theory of the aeroacoustic characteristics of the boundary layer during the initial stage of the transition from a laminar to a turbulent boundary-layer state. The fundamental theoretical background of fluid dynamics is introduced first, followed by a literature survey on boundary-layer aeroacoustics. A novel theoretical approach is presented, an acoustic source method, for solving the frequency characteristics of the boundary layer in the initial phase of the transition. The proposed model is based on the theory of single-mode linear instability. The last part of the thesis describes experiments performed in a non-aeroacoustic wind tunnel facility. The experimental results obtained on a NACA 0012 airfoil at zero angle of attack are compared with the results obtained from the proposed method of solution of frequency characteristics. The theoretical and experimental results agree closely with each other and with the results obtained from the empirical model of Brooks, Pope, and Marcolini.

Keywords: laminar boundary layer, boundary-layer aeroacoustics, Tollmien–Schlichting waves, linear instability, acoustic feedback

Supervisors:

doc. Ing. Tomáš Hyhlík, Ph.D. (2021–),
prof. Ing. Jiří Nožička, CSc. (2016–2021)

Czech Technical University in Prague
Faculty of Mechanical Engineering
Technická 4,
Praha 6, 160 00

Abstrakt

Aeroakustika mezní vrstvy je relativně nový studijní obor, který se zabývá mezní vrstvou jako zdrojem zvuku. Tato práce si klade za cíl rozšířit teorii aeroakustických charakteristik mezní vrstvy během počáteční fáze přechodu ze stavu laminární mezní vrstvy do stavu turbulentní mezní vrstvy. Nejprve jsou představeny základní teoretické základy dynamiky tekutin, poté následuje literární přehled o aeroakustice mezní vrstvy. Tato práce představuje nový teoretický přístup, metodu akustického zdroje, k řešení frekvenčních charakteristik mezní vrstvy v počáteční fázi přechodu. Navržený model je založen na teorii lineární nestability. Poslední část práce se zabývá experimentem, který je navržen s ohledem na aerodynamický tunel, který není primárně určen pro aeroakustický experiment. Experimentální výsledky získané na NACA 0012 při nulovém úhlu náběhu jsou porovnány s výsledky získanými z navržené metody řešení frekvenčních charakteristik. Teoretické a experimentální výsledky se velmi dobře shodují mezi sebou a s výsledky získanými z empirické metody dle Brookse, Popea a Marcoliniho.

Klíčová slova: laminární mezní vrstva, aeroakustika mezní vrstvy, Tollmienovy-Schlichtingovy vlny, lineární nestabilita, akustická zpětná vazba

Překlad názvu: Aeroakustická charakteristika režimů mezní vrstvy

Contents

1 Introduction	1		
1.1 Structure of the Thesis	2		
2 Introduction to Aerodynamics and Acoustics	3		
2.1 Fundamental Equations of Fluid Dynamics	3		
2.1.1 Balance of Mass	3		
2.1.2 Balance of Momentum	3		
2.1.3 Balance of Energy	4		
2.1.4 Vorticity	4		
2.1.5 Stream Function	5		
2.1.6 Fluid Model	5		
2.2 Laminar and Turbulent Flow	6		
2.3 Reynolds Decomposition	7		
2.3.1 Reynolds-Averaged Navier–Stokes Equations	7		
2.4 Boundary Layer	8		
2.4.1 Boundary-Layer Parameters	9		
2.4.2 Shape Parameter	10		
2.4.3 Reynolds Number	10		
2.5 Laminar Boundary Layer	10		
2.5.1 Prandtl’s Boundary-Layer Equations	11		
2.5.2 Falkner–Skan Boundary Layer	12		
2.6 Boundary-Layer Transition	14		
2.7 Stability of the Boundary Layer	15		
2.7.1 Linear Stability	16		
2.8 Boundary-Layer Separation	17		
2.8.1 Laminar Boundary-Layer Separation Bubble	17		
2.9 Introduction to Acoustics	17		
2.9.1 Sound Pressure Level	18		
2.10 Summary	18		
3 Literature Survey and Objectives of the Study: Aerodynamically Generated Sound	20		
3.1 Aerodynamically Generated Sound	20		
3.1.1 Lighthill’s Analogy	20		
3.1.2 Solution of Lighthill’s Equation	20		
3.1.3 Howe Theory	21		
3.1.4 Empirical Model of Brooks, Pope, and Marcolini	21		
3.2 Boundary-Layer Noise	22		
3.2.1 Laminar Boundary-Layer Instability Noise	23		
3.2.2 Turbulent Boundary-Layer Trailing-Edge Noise	27		
3.2.3 Summary	28		
3.3 Objectives of the Thesis	29		
Methods for Achieving the Objectives	29		
4 Laminar Boundary-Layer Instability Noise	31		
4.1 Falkner–Skan Laminar Velocity Profiles	32		
4.1.1 Solution of the Falkner–Skan Equation	33		
4.1.2 Summary	35		
4.2 Stability: Orr–Sommerfeld Equation	37		
4.2.1 Chebyshev Method	37		
4.2.2 Temporal Stability	40		
4.2.3 Spatial Stability	43		
4.2.4 Conclusion	46		
4.3 Spatial Instability in the Boundary Layer of an Airfoil	47		
4.3.1 Boundary-Layer Development	47		
4.3.2 Linear Perturbation	49		
4.3.3 Growth Rate	50		
4.3.4 Transition in a Laminar Separation Bubble	50		
4.4 Noise Source in a Laminar Boundary Layer	50		
4.4.1 Tonal Noise Frequency Model	54		
4.4.2 Conclusion	55		
4.5 Acoustic Feedback	56		
5 Experiment	58		
5.1 Wind Tunnel	58		
5.2 Measurement Methods	59		
5.3 Measurement Setup	59		
List of Main Components	60		
5.3.1 Free-Field Microphones Setup	61		
5.3.2 Airfoil Microphones Setup	61		
5.3.3 Velocity Calibration	64		
5.4 Processing of Measured Data	65		
5.4.1 Selected Measured Spectra	66		
5.5 Conclusion	69		
6 Results and Discussion	70		
6.1 Dominant Frequency of NACA 0012	70		

6.1.1 BPM Empirical Model	70
6.1.2 Tonal Frequency Comparison	71
6.1.3 Discussion on the Strouhal Number Length Scale	74
6.2 Acoustic Feedback	75
7 Conclusions	77
7.1 Application of the Thesis Results	78
7.2 Brief Summary of the Thesis Objectives	78
7.3 Future Work	79
Bibliography	81
Author's References	89
Appendix A Derivation of the Basic Aeroacoustic Equations of the Boundary Layer	90
A.1 Derivation of Lighthill's Equation	90
A.2 Source Term for the Boundary Layer	91
Appendix B Supplementary Results	93
B.1 Neutral Curve of the Blasius Boundary Layer	93
B.2 Boundary-Layer Thickness	94
B.3 Instability Noise Peak Frequency for NACA 0012	95

Figures

<p>2.1 Schematic illustration of the boundary layer at a flat plate [21]. 9</p> <p>2.2 Falkner–Skan equation boundary-layer velocity profiles. 13</p> <p>2.3 Boundary layer natural transition [27, p. 377]. 14</p> <p>2.4 Curves of neutral stability for a plane boundary layer [21]. 15</p> <p>3.1 Laminar boundary-layer vortex-shedding noise as it was observed by Paterson in 1973 [44]. 24</p> <p>3.2 Dual-feedback model proposed by Arcondoulis et al. [61]. 26</p> <p>4.1 Detail at local minimum of $\frac{\partial^2 f}{\partial \eta^2}(0)$ as a function of shape factor. 34</p> <p>4.2 Local minimum of $\frac{\partial^2 f}{\partial \eta^2}(0)$ as a function of Hartree parameter β. 35</p> <p>4.3 The H–β plot for the Falkner–Skan boundary layer. 35</p> <p>4.4 Dependency of $\frac{\partial^2 f}{\partial \eta^2}(0)$ on the shape factor H. 36</p> <p>4.5 <i>Argand diagram</i> of the complex phase velocity as a solution to the temporal stability problem. 41</p> <p>4.6 Temporal stability of the Blasius boundary layer, i.e., $H = 2.56$, $\beta = 0$. The curves are iso-curves of constant phase velocity (blue) and constant growth/decay rate (black). 42</p> <p>4.7 <i>Argand diagram</i> of complex phase velocity for the Blasius boundary layer (i.e., $H = 2.56$, $\beta = 0$) for three different cases. 44</p> <p>4.8 Spatial stability of the Blasius boundary layer, i.e., $H = 2.56$, $\beta = 0$. The curves shown are iso-curves of constant phase velocity (blue) and constant growth/decay rate (black). 45</p> <p>4.9 Amplitude functions of the least stable/most unstable modes of the Blasius boundary layer, i.e., $H = 2.56$, $\beta = 0$, for three different cases (with the same conditions as in Fig. 4.7). 46</p>	<p>4.10 Shape factor along NACA 0012 for four different Reynolds numbers (5 000, 10 000, 50 000, and 100 000) based on the chord length L. <i>Obtained using XFOIL</i>. 48</p> <p>4.11 Displacement thickness along NACA 0012 for four different Reynolds numbers (5 000, 10 000, 50 000 and 100 000). <i>Obtained using XFOIL</i>. 48</p> <p>4.12 Velocity outside the boundary layer along NACA 0012 for a Reynolds number of 50 000. <i>Obtained using XFOIL</i>. 49</p> <p>4.13 Field of acoustic sources in the boundary layer $Q(x, y)_{\text{RMS}}$ of NACA 0012 with 6.62 m/s freestream velocity and perturbation frequency 293 Hz. The red curve is the local boundary-layer displacement thickness ($\delta^*/\delta_{L_{\text{TE}}}$) and the green curve is the local conventional boundary-layer thickness ($\delta/\delta_{L_{\text{TE}}}$). The displacement and conventional thicknesses are both normalized to the boundary-layer length scale at the trailing edge ($\delta_{L_{\text{TE}}}$). 53</p> <p>4.14 Comparison of the proposed tonal model with the model of the maximal growth of Tollmien–Schlichting waves for velocity 6.62 m/s (Reynolds number $Re_L = 44143$). 55</p> <p>5.1 Positioning of the microphones inside the airfoil. 60</p> <p>5.2 Free-field Microtech Gefell M370 microphone. 61</p> <p>5.3 CMC-4015-25L100 microphone. 61</p> <p>5.4 The electrical circuit used to power the electret microphones with a low-pass filtered power supply. 62</p> <p>5.5 The stripboard with the electrical circuit for the electret microphones. 63</p> <p>5.6 Electret microphones inside the test airfoil segment. 63</p> <p>5.7 The calibration of the airspeed with the Pitot-static probe. 64</p>
---	--

5.8 Study of the effect of time interval length for data recording.	65
5.9 First selected spectrum at freestream velocity 7.59 m/s.	67
5.10 Second selected spectrum at freestream velocity 8.56 m/s.	67
5.11 Third selected spectrum at freestream velocity 10.99 m/s.	68
5.12 Fourth selected spectrum at freestream velocity 14.87 m/s.	68
5.13 Fifth selected spectrum at freestream velocity 22.64 m/s.	69
6.1 Measured, empirical, and simulation peak frequency for velocities below the predicted transition in the laminar separation bubble.	71
6.2 Measured, empirical, and simulation peak Strouhal number for velocities below the predicted transition in the laminar separation bubble. The characteristic length used to define the Strouhal number is based on the conventional boundary-layer thickness.	72
6.3 Primary and secondary tones in all measured points	73
6.4 Dominant tones' Strouhal number based on two different length scales: the displacement thickness δ^* and the conventional thickness δ_{99}	74
6.5 Feedback length based on experimentally obtained Δf and the theoretical feedback length, which is equal to the distance from the first occurrence of instability to the trailing edge.	76

Tables

4.1 Selected parameters of the Falkner–Skan equation for different shape factors.	36
6.1 The mean value and standard deviation of the obtained results in the predicted laminar boundary-layer state.	72
6.2 Measured difference Δf between the peak frequency and secondary frequency.	75
B.1 Flat plate marginal stability solution	93
B.2 NACA 0012 boundary-layer thickness at the trailing edge.	94
B.3 NACA 0012 prediction of peak frequencies based on the method of maximal amplitude growth and associated properties of the linear stability analysis.	95
B.4 NACA 0012 prediction of peak frequencies based on the method of acoustic sources (the method proposed in this thesis) and associated properties of linear stability analysis.	96

Nomenclature

A, a	=	arbitrary function
c	=	convective velocity (of sound wave or disturbance)
C	=	capacitance of condenser
\mathbf{C}	=	constants of characteristic polynomial
c_p, c_v	=	specific heat capacity at constant pressure, volume
e	=	internal energy
h	=	enthalpy
H	=	shape factor
f_i	=	volume forces
f	=	arbitrary function
f	=	frequency
f	=	Falkner–Skan function
i	=	imaginary unit
k	=	streamwise wave number
L	=	characteristic length (e.g., chord length)
L_F	=	acoustic feedback length
N	=	number of collocation points of the Chebyshev domain
N_{crit}	=	critical exponent of the amplification factor of the $e^{N_{\text{crit}}}$ method
p	=	pressure
Q	=	acoustic source term
R	=	resistance
Re	=	Reynolds number
Re_L	=	Reynolds number with chord length as characteristic length
St	=	Strouhal number
t	=	time
T	=	temperature
T	=	time period
T_{ij}	=	Lighthill stress tensor
u, v	=	velocity
U, V	=	base velocity
x, y, z	=	Cartesian spatial coordinates
β	=	Hartree parameter
γ	=	isentropic exponent
δ	=	conventional boundary-layer thickness
δ^*	=	boundary-layer displacement thickness
δ^{**}	=	boundary-layer momentum thickness
δ_{ij}	=	Kronecker delta
δ_{ijk}	=	extended Kronecker delta
δ_L	=	boundary-layer length scale
ζ	=	bulk viscosity
η	=	non-dimensional coordinate
$\hat{\eta}$	=	non-dimensional coordinate transformed to Chebyshev domain
κ	=	arbitrary variable
μ	=	dynamic viscosity
ν	=	kinematic viscosity

ρ	=	density
τ_{ij}	=	viscous stress tensor
τ_w	=	wall shear stress
Φ	=	amplitude function
ϕ	=	transformed amplitude function
φ	=	phase shift
Ψ	=	stream function
$\vec{\omega}$	=	vorticity
ω	=	angular frequency
\mathcal{A}	=	amplification factor
\mathcal{D}	=	derivative operator of the Chebyshev method
\mathcal{F}	=	frequency model function

Indices

e	=	variable outside the boundary layer
i, j, k, l, m	=	iterative indices
i	=	imaginary part of a complex number
r	=	real part of a complex number
RMS	=	root-mean-square value
TE	=	trailing edge
x, y	=	spatial indices
∞	=	freestream
δ^*	=	non-dimensional boundary layer parameter based on the displacement thickness
η	=	non-dimensional boundary layer parameter based on the scale δ_L

Abbreviations

BPM	=	empirical model of Brooks, Pope, and Marcolini
RMS	=	root mean square
SPL	=	sound pressure level



Chapter 1

Introduction

Sound is one of the physical phenomena that can be perceived directly by human beings, although an observer does not necessarily need to be in close proximity to a source of sound. Usually, humans can readily distinguish between loud and quiet sounds, and between discrete high- and low-pitch tones in an emitted acoustic spectrum. Sound can be described as an acoustic wave that propagates through a medium. The acoustic wave causes a small perturbation in the local static pressure field. Such an acoustic wave can be generated, for example, by vibrating surfaces or by certain local changes in the pressure field. A solid object placed in a moving fluid (e.g., an airfoil in an air flow) produces changes in the pressure field, which can be propagated to the far field in the form of an acoustic wave.

The boundary layer is defined as a thin viscous layer around an object placed in a moving fluid [1]. One of the main goals of studying the boundary layer is to understand transitions from laminar to turbulent regimes. For these investigations, it is usually necessary to conduct multiple measurements. Intrusive measurement techniques affect the flow, so there can be no certainty that the transition to the turbulent boundary layer is not caused by the measurement device itself.

Aeroacoustics is a relatively new field of study that aims to understand both aerodynamically generated sound and the effects of sound on fluid flow. Sir James Lighthill (1924–1998) is considered one of the pioneers in the field of aeroacoustics. His papers *On sound generated aerodynamically I* and *II* [2, 3] are the two most important and fundamental works in this discipline. The formal solution of his theory in the presence of a solid boundary was later published by his student Samuel Newby Curle (1930–1989) in *The influence of solid boundaries upon aerodynamic sound* [4]. Lighthill's work was later extended and generalized by John Ffowcs Williams and D. L. Hawkings in *Sound generation by turbulence and surfaces in arbitrary motion* [5]. These pioneering works laid the foundations of modern aeroacoustics, which is partly a branch of aerodynamics and partly of acoustics.

This thesis aims to describe the boundary layer as a source of aerodynamic noise, and to study the effects of the boundary-layer transition in the early stages on the acoustic field. This research extends the current aeroacoustic theory and experimentally validates the new theoretical findings, contributing

to the field of fundamental research into the aeroacoustics of the boundary layer.

Since the boundary layer develops near walls in the flow of every viscous fluid, the aims of thesis are focused on the external flow around flat plates and surfaces with small curvature.

■ 1.1 Structure of the Thesis

This thesis can be divided into two main parts. The first part consists of a brief introduction to the key concepts and nomenclature of fluid dynamics that are necessary to establish the main theoretical background for the literature survey. This theoretical background is also necessary for the formulation of the theoretical model presented in this thesis.

This is followed by a literature survey and a summary of key findings in the field. This literature survey focuses on the aeroacoustics of the boundary layer and concludes with the formulation of the main objectives of the thesis in Section 3.3.

The first chapter of the second part of this thesis (i.e., Chapter 4) focuses on theoretical modeling of the boundary-layer instability noise. In this chapter, the main proposed aeroacoustic model of the instability noise is established. For this extension of the current aeroacoustic model, the key theoretical findings from Chapter 2 and the recent developments in the aeroacoustic field outlined in Chapter 3 are used.

This is followed by a description of the setup of an experiment (Chapter 5), which is required to validate the novel aeroacoustic model. The experiment was designed for a non-aeroacoustic wind tunnel facility with the goal of obtaining the frequency footprint of the boundary-layer noise.

The results obtained from the theoretical and experimental work are then analyzed and compared in Chapter 6, and the conclusions of the thesis are presented in Chapter 7.

Chapter 2

Introduction to Aerodynamics and Acoustics

2.1 Fundamental Equations of Fluid Dynamics

Fluid dynamics is generally described by fundamental balance laws: balance of momentum, balance of mass, and balance of energy. With knowledge of fluid behavior (i.e., equations of state), the full system of equations describing fluid dynamics can be established.

In this chapter, a brief introduction of the fundamental governing equations of fluid dynamics is provided to establish the necessary background and nomenclature. A more detailed derivation of these equations is beyond the scope of this thesis.

2.1.1 Balance of Mass

The first balance law, which is also the most intuitive, is the *balance of mass*. This can be described as follows: In the flow field, the total mass must remain constant, unless there is a sink or source that adds or removes mass. The derivation of the mathematical form is presented in almost every textbook on fluid dynamics (e.g., [6]). Eq. (2.1) is a differential form of the balance of mass of compressible fluids under unsteady flow conditions with no source or sink:

$$\frac{\partial \rho}{\partial t} + \frac{\partial (\rho v_x)}{\partial x} + \frac{\partial (\rho v_y)}{\partial y} + \frac{\partial (\rho v_z)}{\partial z} = 0 \quad (2.1)$$

2.1.2 Balance of Momentum

The first attempt to formulate a *quantity of motion* was made by Descartes in his 1644 work *Principles of Philosophy*; however, his definition of this property is based only on the size and velocity of the body in question [7]. Descartes also formulated some laws of motion, which are very similar to the laws used in today's Newtonian physics. Descartes' explanation of his laws was the immutability of God; however, Descartes' ideas laid the foundation for the formulation of *Newton's laws of motion* [7].

In 1687, Sir Issac Newton published his *Philosophiæ Naturalis Principia Mathematica* [8], in which he formulated his laws of motion. The quantity of motion, the *momentum*, was defined based on the mass and velocity (not on size and velocity like in Descartes' definition). Based on Newton's second law of motion, Claude-Louis Navier and George Gabriel Stokes derived the mathematical formulation of the balance of momentum in *Newtonian fluids*.

Today, the momentum balance equations in fluid dynamics are called the *Navier–Stokes equations*¹. The derivation of these equations is now part of all basic textbooks on fluid dynamics, for example [6]. The Navier–Stokes equation for the compressible fluid flow of a Newtonian fluid is as follows:

$$\frac{\partial(\rho v_i)}{\partial t} + \frac{\partial(\rho v_i v_j)}{\partial x_j} = -\frac{\partial p}{\partial x_i} + \frac{\partial \tau_{ij}}{\partial x_j} + f_i \quad (2.2)$$

The terms f_i are body forces, and τ_{ij} denotes the viscous stress, which can be defined as follows:

$$\tau_{ij} = \mu \left(\frac{\partial v_i}{\partial x_j} + \frac{\partial v_j}{\partial x_i} - \frac{2}{3} \delta_{ij} \frac{\partial v_k}{\partial x_k} \right) + \zeta \delta_{ij} \frac{\partial v_k}{\partial x_k} \quad (2.3)$$

where μ is the dynamic viscosity and ζ is the bulk viscosity.

2.1.3 Balance of Energy

To complete this set of fundamental balance equations, the balance of energy should be established. The *enthalpy* is an energy quantity defined as the sum of the internal energy e and the external (pressure) energy p/ρ [6]:

$$h = e + \frac{p}{\rho} \quad (2.4)$$

The enthalpy form of the energy balance equation [9], neglecting heat transfer and body forces, is

$$\frac{\partial(\rho h)}{\partial t} + \frac{\partial(\rho h v_j)}{\partial x_j} = \frac{\partial p}{\partial t} + v_j \frac{\partial p}{\partial x_j} + \tau_{ij} \frac{\partial v_i}{\partial x_j} \quad (2.5)$$

2.1.4 Vorticity

One of the quantities used in flow dynamics is vorticity. Mathematically, the vorticity is defined as the curl of the velocity field:

$$\vec{\omega} = \nabla \times \vec{v} \quad (2.6)$$

The vorticity equation is derived by taking the curl of the momentum equation, Eq. (2.2). For an incompressible fluid, the vorticity equation can be simplified as follows:

$$\frac{\partial \vec{\omega}}{\partial t} - \nabla \times (\vec{v} \times \vec{\omega}) = \nabla \times \vec{f} + \mu \cdot \nabla^2 \vec{\omega} \quad (2.7)$$

¹In some works, the Navier–Stokes equations also include the balance of mass, i.e., Eq. (2.1).

where the term $\vec{v} \times \vec{\omega}$ is called the *Lamb vector* and, for two-dimensional incompressible flow, can be written as $-(\vec{\omega} \cdot \nabla)\vec{v}$. This leads to a two-dimensional vorticity equation for the flow of an incompressible fluid:

$$\frac{\partial \vec{\omega}}{\partial t} + \vec{v}(\vec{\omega} \cdot \nabla) = \nabla \times \vec{f} + \mu \nabla^2 \vec{\omega} \quad (2.8)$$

This equation describes the generation of vorticity, and can be applied to study the vorticity around an airfoil, which is generated in the force field (the curl of the force field) and is destroyed by the viscous forces.

■ 2.1.5 Stream Function

The two-dimensional *stream function* $\Psi(x, y)$ is defined as the flux across a line between two arbitrary points A and P from right to left, as defined by Lamb [10], for velocity components u and v in the x - and y -directions, respectively:

$$\Psi(x, y) = \int_A^P (u dy - v dx) \quad (2.9)$$

Using the total differential of the stream function Ψ , the relation between the velocities (u, v) and the stream function Ψ can be found [6]:

$$u = \frac{\partial \Psi}{\partial y} \quad (2.10a)$$

$$v = -\frac{\partial \Psi}{\partial x} \quad (2.10b)$$

Since, by its definition, the stream function always satisfies the continuity equation, using the stream function to describe a flow field of inviscid fluid is usually convenient.

■ 2.1.6 Fluid Model

The definition of the fluid physical model is crucial to obtaining some of the basic physical properties. Since the scope of this thesis is limited to the flow of air under standard conditions, it is sufficient to model air as an ideal gas. The equation of state of the ideal gas (2.11) describes the link between three state variables (pressure, temperature, and density), via the specific gas constant $r = 287.05 \text{ J K}^{-1} \text{ kg}^{-1}$ [11]:

$$\frac{p}{\rho} = r \cdot T \quad (2.11)$$

Air is considered not only a thermally perfect gas², but also a calorically perfect gas, so the heat capacity at constant pressure c_p and the heat capacity at constant volume c_v are constant (i.e., they do not change with temperature or pressure).

²A thermally perfect gas is one that obeys the equation of state for an ideal gas.

The ratio of heat capacity at constant pressure to heat capacity at constant volume is the isentropic exponent

$$\gamma = \frac{c_p}{c_v} \quad (2.12)$$

For air as a calorically perfect gas, $\gamma = 1.4$. The dynamic viscosity of the air can be obtained using the Sutherland equation [11]:

$$\mu = \frac{\beta_S \cdot T^{3/2}}{T + S} \quad (2.13)$$

where $S = 110.4 \text{ K}$ and $\beta_S = 1.458 \cdot 10^{-6} \text{ kg} \cdot \text{m}^{-1} \cdot \text{s}^{-1} \cdot \text{K}^{-1/2}$ are constants [11].

Among the important properties of a fluid is the speed of sound. This is the convective speed of an acoustic wave, so is of great importance for aeroacoustics. The sound wave is assumed to be isentropic, so the definition of the speed of sound for the ideal gas is [12]

$$c^2 = \left(\frac{\partial p}{\partial \rho} \right)_s = \frac{\gamma p}{\rho} \quad (2.14)$$

Based on the first law of thermodynamics and the assumption of isentropic flow, the relationship between instantaneous pressure, density, and speed of sound can be obtained [12]:

$$\frac{\partial p}{\partial t} + v_i \cdot \frac{\partial p}{\partial x_i} = \frac{\gamma p}{\rho} \left(\frac{\partial \rho}{\partial t} + v_i \cdot \frac{\partial \rho}{\partial x_i} \right) \quad (2.15)$$

2.2 Laminar and Turbulent Flow

Laminar flow is commonly described in the literature as *smooth and regular* [6, p. 152], [13, p. 415]. However, this definition is not entirely accurate. The definition of laminar flow adopted in this thesis is based on the stability of the flow under external perturbations, which leads to the following definition: Laminar flow is a type of flow in which external disturbances are damped, so that they do not grow and eventually vanish. This means that, in laminar flow, there is the possibility of the existence of a perturbation of flow from the base value. If such a perturbation has no significant impact on the flow field (and this is assumed in most cases), this perturbation is usually neglected.

However, turbulent flow is quite different. Perturbations from the base value (or time-averaged value) are a key attribute of turbulent flow. However, the existence of a perturbation itself is not enough to define turbulent flow. The basic description of turbulent flow is that the fluid particles move in a random and irregular manner; there are seven characteristic features for turbulence, as defined by Tennekes and Lumley [14]:

- Irregularity
- Diffusivity

- Large Reynolds numbers
- Three-dimensional vorticity fluctuations
- Dissipation
- Continuum
- Turbulent flows are flows (i.e., “Turbulence is not a feature of fluids but of fluid flow” [14]).

■ 2.3 Reynolds Decomposition

Since the time-averaged value was mentioned in the previous section as part of the definition of turbulent flow, it should also be properly defined. The idea of decomposing a time-dependent quantity into a time-averaged value and a fluctuating value was developed by Osborne Reynolds [15]. The *Reynolds decomposition* of an arbitrary variable $a(x_i, t)$ can be written as

$$a(x_i, t) = A(x_i) + a'(x_i, t) \quad (2.16)$$

where $A(x_i)$ is the time-averaged value and $a'(x_i, t)$ represents the fluctuations. The definition of the time-averaged quantity is [16]

$$A(x_i) = \lim_{T \rightarrow \infty} \frac{1}{T} \int_0^T a(x_i, t) dt \quad (2.17)$$

In real cases, the time interval T cannot approach infinity; it must be significantly large compared to the time scales of the fluctuations. The definition of time-averaged value implies that the time-averaged fluctuations of the variable a are

$$\overline{a'}(x_i, t) = 0 \quad (2.18)$$

The Reynolds decomposition (Eq. (2.16)) can be applied to each quantity in the flow field: the density, pressure, and velocity. For example, the Reynolds decomposition of the velocity v_i is

$$v_i = V_i + v'_i \quad (2.19)$$

where V_i is the time-averaged value of the velocity and v'_i represents the velocity fluctuations about the time-averaged value.

■ 2.3.1 Reynolds-Averaged Navier–Stokes Equations

Applying the Reynolds decomposition to the continuity equation (Eq. (2.1)) and the momentum equations (Eq. (2.2)) for the flow of an incompressible fluid without body forces yields the Reynolds-Averaged Navier–Stokes (RANS) equations [16]:

$$\frac{\partial(\rho V_i)}{\partial x_i} = 0 \quad (2.20)$$

$$\frac{\partial(\rho V_i)}{\partial t} + \frac{\partial}{\partial x_j} (\rho V_i V_j + \overline{\rho v'_i v'_j}) = -\frac{\partial \bar{p}}{\partial x_i} + \frac{\partial \bar{\tau}_{ij}}{\partial x_j} \quad (2.21)$$

where $\bar{\tau}_{ij}$ is the mean viscous stress tensor, defined by

$$\bar{\tau}_{ij} = \mu \left(\frac{\partial V_i}{\partial x_j} + \frac{\partial V_j}{\partial x_i} \right) \quad (2.22)$$

The term $-\overline{\rho v'_i v'_j}$ in Eq. (2.21) is called the *Reynolds stress* and is one of the main subjects of turbulence modeling [17, 18].

2.4 Boundary Layer

The *boundary layer* is defined as a thin layer of viscous fluid in motion near a solid wall. In the boundary layer, the effects of the frictional forces are important. The fluid adheres to the wall under the *no-slip condition*. This is an important assumption, and it defines significant difference between the flow of a real fluid and an ideal fluid [1, p. 3]. The concept of the boundary layer was first presented by Ludwig Prandtl in Heidelberg in his 1904 paper *On the motion of fluids with very little friction* (English translation of the original paper from German) [19, p. 77–84]. Prandtl’s idea was to divide the flow field into two regions—one in which the friction is so small that it may be neglected, and one in which there is a large variation in velocity caused by the friction. The second region is now called the *boundary layer*; however, Prandtl used this term in his original work only once, preferring the term *transition layer*. Since this could cause confusion with the transition region to turbulence, this term was later dropped [19]. He also formulated the assumption of the no-slip condition.

An illustration of the velocity profile in the boundary layer is shown in Fig. 2.1. Since the original formulation of the boundary layer hypothesis, which was one of the most important achievements in modern aerodynamics³, there has been a major development of boundary-layer models, experimental research, and computational simulations.

The boundary-layer flow can be described using the following attributes [16]:

- Diffusive transport of momentum in the parallel flow direction is much smaller than convection and is negligible
- The velocity component in the parallel flow direction is much higher than in other directions
- The pressure gradient across the flow is much lower than in the principal flow direction

³Some would say that this achievement was worthy of a Nobel Prize; however, it was rumored that the Nobel Prize Committee was reluctant to award prizes in the field of classical physics [20].

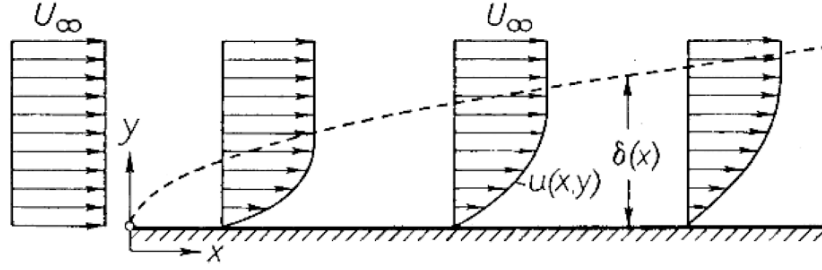


Figure 2.1: Schematic illustration of the boundary layer at a flat plate [21].

2.4.1 Boundary-Layer Parameters

A boundary layer is defined as a thin imaginary layer, whose thickness is not formulated based on geometrical considerations, but rather on the fluid dynamics characteristics of the boundary-layer flow. The main attribute of the boundary-layer flow is its velocity profile. This and other flow parameters are used to define the basic parameters of the boundary layer.

The *conventional thickness* of the boundary layer is defined as the perpendicular distance from the solid boundary (i.e., the surface) to the point where the local flow velocity is equal to 99% of the velocity outside the boundary layer [22]:

$$\delta = \delta(v_x = 0.99U_e) \quad (2.23)$$

where U_e is the velocity outside the boundary layer in the principal x -direction.

The *displacement thickness* for a compressible fluid is defined as follows [22]:

$$\delta^* = \int_0^\delta \left(1 - \frac{\rho v_x}{\rho_e U_e}\right) dy \quad (2.24)$$

where ρ_e is the fluid density outside the boundary layer. The displacement thickness has two physical interpretations [22]: First, it is proportional to the missing mass flow due to the presence of the boundary layer. Second, it is the distance by which the inviscid flow is displaced in the presence of the boundary layer.

The *momentum thickness* for a compressible fluid is defined as follows [22]:

$$\delta^{**} = \int_0^\delta \frac{\rho v_x}{\rho_e U_e} \left(1 - \frac{v_x}{U_e}\right) dy \quad (2.25)$$

The momentum thickness can be physically interpreted as the distance by which the solid surface must be displaced in an inviscid fluid flow to have the same momentum flow rate as in the boundary layer.

The ratio of the displacement thickness to the momentum thickness is called the *shape parameter*:

$$H = \frac{\delta^*}{\delta^{**}} \quad (2.26)$$

■ 2.4.2 Shape Parameter

The shape parameter has a significant meaning in the classification of the boundary-layer velocity profile. On the basis of its value, the regime (or state) of the boundary layer can be determined as laminar or turbulent [21]. In the case where the shape factor is equal to 1, there is no boundary layer present and the flow past the wall can be described as an inviscid potential flow:

- $H = 1$: Potential Flow
- $H = 2.59$: Blasius boundary layer velocity profile (i.e., a laminar boundary layer on a flat plate)
- $H \leq 1.4$: Turbulent boundary layer [21, p. 585]

The values of the shape parameter in the range between the laminar and turbulent regions are characteristic of the transition region [23].

The boundary-layer separation is described in Section 2.8; however, the shape factor can also be used to identify the boundary-layer separation. For a laminar boundary layer, a shape factor around $H = 4$ (based on the Falkner–Skan equation; see Section 2.5.2) indicates separation. However, because of the rapid growth of the displacement thickness before the separation point, this shape factor may not be reliable for the experimental measurement, and the shape parameter based on the energy thickness can be used instead [24].

The above list of values of the shape factor is merely an approximation, for example, M. Drela in XFOIL [25] used $H = 3.8$ to identify laminar boundary-layer separation and $H = 1.8$ for turbulent boundary-layer separation.

■ 2.4.3 Reynolds Number

One of the most important similarity numbers in fluid dynamics is the *Reynolds number*. The Reynolds number indicates the significance of inertia over viscous forces. The higher the Reynolds number, the more important the inertial force. The common definition of the Reynolds number is

$$Re_L = \frac{\rho \cdot v \cdot L}{\mu} \quad (2.27)$$

where v is the velocity, μ is the dynamic viscosity, and ρ is the density of the fluid. The characteristic length L can be subject to discussion; however, for a boundary layer, it should be the length connected to the shear layer (i.e., some boundary-layer thickness). The distance from the leading edge to some point on the surface (or trailing edge) is used as the characteristic length in many cases. This distance is connected to the thickness of the boundary layer, since the latter increases with distance from the leading edge [21, p. 31].

■ 2.5 Laminar Boundary Layer

Initially, every boundary layer starts in the laminar state of flow. Later, based on the external and internal flow parameters, the boundary layer can

transition (Section 2.6) from this laminar state to a turbulent state or can separate (Section 2.8).

2.5.1 Prandtl's Boundary-Layer Equations

Prandtl not only proposed the concept of the boundary layer but also developed the simplification of the Navier–Stokes equation for boundary-layer flow. However, Prandtl did not provide a detailed explanation of this process during his presentation in Heidelberg in 1904. A more detailed explanation can be found in a work by his student H. Blasius, *Boundary layers in fluids with small friction* (English translation [19, p. 107–142]). In fact, Prandtl's concept of the boundary layer was somewhat forgotten until Blasius' solution surfaced in 1908 [20].

The thickness of the boundary layer is denoted as δ , and because the velocity in the direction parallel to the surface (v_x) increases with the distance from the surface, Blasius formulated the following proportional relations [19, p. 107–142]:

$$\frac{\partial v_x}{\partial y} \propto \frac{1}{\delta}; \quad \frac{\partial^2 v_x}{\partial y^2} \propto \frac{1}{\delta^2}$$

Blasius also stated that when $\partial v_x/\partial x$ is on the order of one⁴, based on the continuity equation (Eq. (2.1)), the derivative $\partial v_y/\partial y$ is also on the order of one (or proportional to $1/L$; see the footnote). This leads to the following proportional relations:

$$v_y \propto \delta; \quad \frac{\partial^2 v_y}{\partial y^2} \propto \frac{1}{\delta}$$

The derivative of the pressure field $\partial p/\partial x$ is proportional to one (or $1/L$; see the footnote) and $\partial p/\partial y$ is proportional to δ [19, p. 107–142].

Recalling the Navier–Stokes equations (Eq. (2.2)) for two-dimensional steady flow of an incompressible fluid (i.e., $\partial v_i/\partial t = 0$, $\partial \rho/\partial t = 0$) and without mass forces (i.e., $f_i = 0$), and substituting in the viscous stress of a Newtonian fluid, Eq. (2.3), the balance of momentum equations are as follows:

$$\rho \left(v_x \frac{\partial v_x}{\partial x} + v_y \frac{\partial v_x}{\partial y} \right) = -\frac{\partial p}{\partial x} + \mu \left(\frac{\partial^2 v_x}{\partial x^2} + \frac{\partial^2 v_x}{\partial y^2} \right) \quad (2.28a)$$

$$\rho \left(v_x \frac{\partial v_y}{\partial x} + v_y \frac{\partial v_y}{\partial y} \right) = -\frac{\partial p}{\partial y} + \mu \left(\frac{\partial^2 v_y}{\partial x^2} + \frac{\partial^2 v_y}{\partial y^2} \right) \quad (2.28b)$$

Based on Blasius' proportional analysis, in Eq. (2.28a), the second derivatives satisfy, with the assumption that $\delta \ll 1$ (or $\delta \ll L$), the relation

$$\frac{\partial^2 v_x}{\partial x^2} \ll \frac{\partial^2 v_x}{\partial y^2}$$

⁴If it is assumed that there is a boundary-layer development from the leading edge, this can be analogously assumed to be proportional to $\partial v_x/\partial x \propto 1/L$, where L is the length of the immersed surface. However, in Blasius' original derivation, he did not proceed with this length scale.

In the second Eq. (2.28b), the only remaining term is the pressure derivative with respect to y :

$$\rho \left(v_x \frac{\partial v_x}{\partial x} + v_y \frac{\partial v_x}{\partial y} \right) = -\frac{\partial p}{\partial x} + \mu \cdot \frac{\partial^2 v_x}{\partial y^2} \quad (2.29a)$$

$$\frac{\partial p}{\partial y} = 0 \quad (2.29b)$$

The equations (2.29) are called *Prandtl's boundary-layer equations* or simply the *boundary-layer equations*.

There are many possible approaches to solving the boundary-layer equations. Blasius proposed a solution for zero pressure gradient ($\frac{\partial p}{\partial x} = 0$), the well-known *Blasius solution* [19, p. 107–142]. This is based on the principle of mechanical similarity. Using this similarity method, it is possible to transform Prandtl's partial differential equations into a single third-order ordinary differential equation (called the *Blasius equation*, in this case). Unfortunately, the zero pressure gradient is a limited case with only one shape for the velocity profile. (The shape factor for the Blasius boundary layer is 2.59.)

In 1931, Falkner and Skan [26] derived, using a more general approach and the differential Bernoulli's equation instead of the zero pressure gradient ($\frac{\partial p}{\partial x} = 0$), a third-order ordinary differential equation with parameter β .

2.5.2 Falkner–Skan Boundary Layer

Prandtl's boundary-layer equations (Eq. (2.29)) are partial differential equations; using the similarity transformation, they can be reduced to ordinary differential equations [27]. One of the most well-known families of similarity solutions is the Falkner–Skan boundary layer. This solution was derived by Falkner and Skan [26] in 1931, and six years later it was numerically calculated by Hartree [28].

Using the differential form of Bernoulli's equation to express the pressure gradient along the x -axis yields

$$-\frac{1}{\rho} \frac{\partial p}{\partial x} = U_e \frac{\partial U_e}{\partial x} \quad (2.30)$$

The velocity outside the boundary layer $U_e(x)$ is used as the scaling factor for the velocity in the direction parallel to the wall. The factor $\delta_L(x)$ is used as a boundary-layer thickness scale. The stream function is then defined as follows:

$$\Psi = U_e(x) \delta_L(x) f(\eta) \quad (2.31)$$

where η is defined as a non-dimensional coordinate in the y -direction ($\eta = y/\delta_L$). Falkner and Skan assumed a flow over a wedge, which can be in a potential flow described as a function of a power of a complex coordinate (a *power law*) [29]. This key assumption is included in the main similarity expressions for U_e as a scaling factor $(x/L)^m$, where L is the length of the wedge:

$$U_e = U_\infty (x/L)^m \quad (2.32)$$

Falkner and Skan found that the similarity is achieved when $\eta = C \cdot y \cdot x^a$, where C is an arbitrary constant, which makes η non-dimensional and a consistent with the power-law, i.e., $m = 2a + 1$ [29]. Constant C can be chosen to be consistent with the Blasius boundary-layer solution [19, p. 107–142], when $m = 0$. The boundary-layer thickness scale is then

$$\delta_L = \frac{y}{\eta} = \sqrt{\frac{2}{m+1} \cdot \frac{\nu(x/L)}{U_e}} \quad (2.33)$$

By substituting the velocity components (Eq. (2.10a) and (2.10b)), with the stream function in Eq. (2.31), into the Prandtl equation, Eq. (2.29), the *Falkner–Skan boundary-layer equation*⁵ is found [26]:

$$f''' + f f'' + \beta (1 - f'^2) = 0 \quad (2.34)$$

$$\beta = \frac{2m}{m+1} \quad (2.35)$$

The boundary conditions for the Falkner–Skan equations are $f(0) = f'(0) = 0$ and $\lim_{\eta \rightarrow \infty} f'(\eta) = 1$. Physical solutions of the Falkner–Skan boundary layer exist only in the range $-0.198838 \leq \beta \leq 4/3$ [28]. In Fig. 2.2, some selected velocity profiles with different shape factors are shown.

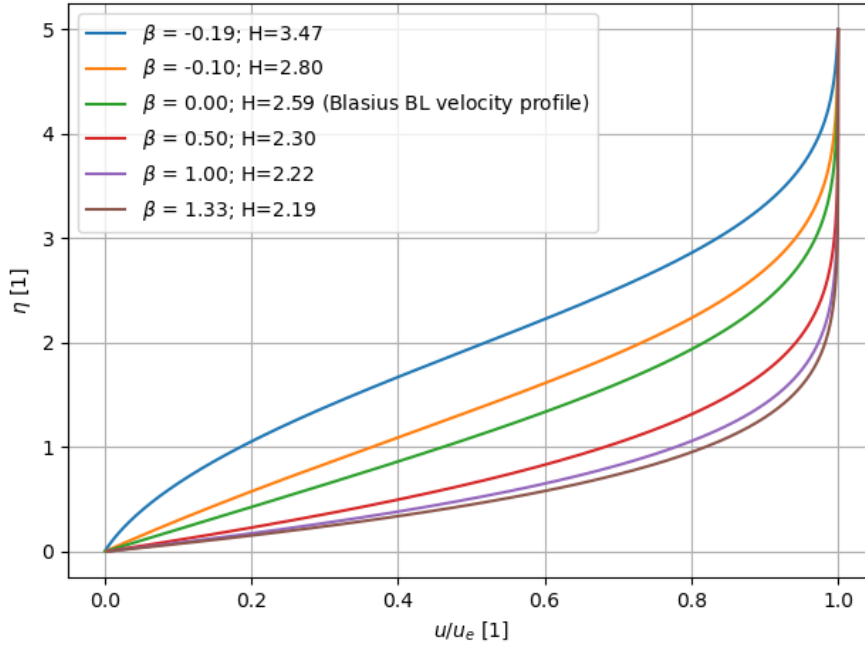


Figure 2.2: Falkner–Skan equation boundary-layer velocity profiles.

⁵The description of the Falkner–Skan equation presented in this thesis is not a full derivation. Falkner and Skan had to derive the equation using a more general approach, because they did not know the scaling factor δ_L , which is an important result of their work.

2.6 Boundary-Layer Transition

As the Reynolds number increases, the boundary-layer flow experiences a *transition* from laminar to turbulent flow. This is of key importance for fluid dynamics [21] and is influenced by a number of parameters; the most important are the Reynolds number, the outer flow pressure distribution, the wall roughness, and the intensity of turbulence [21].

There are three possibilities for the boundary-layer transition from laminar to turbulent states [27]:

- Natural transition
- Bypass transition
- Separated-flow transition

In a natural transition, there are four stages of transition before the fully turbulent boundary layer is developed (see Fig. 2.3). For the bypass transition, the boundary-layer flow may skip the first two stages (Tollmien–Schlichting waves and spanwise vorticity generation) [27]. In the case of laminar separated flow, the transition may occur in the separated flow and then the flow may reattach to the wall.

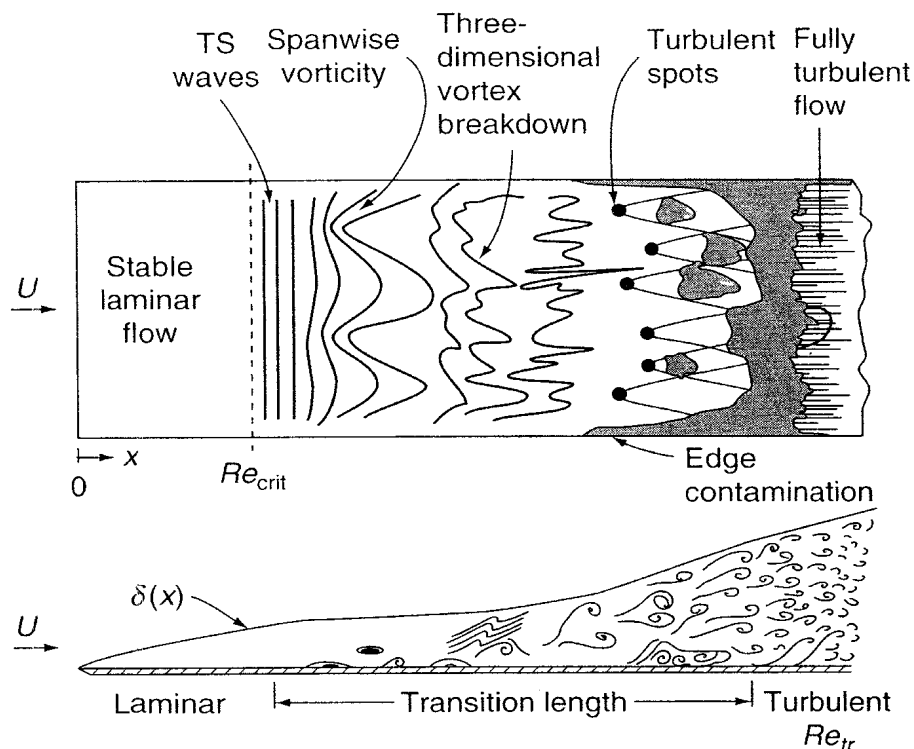


Figure 2.3: Boundary layer natural transition [27, p. 377].

The natural transition of the boundary layer contains the following steps [27, 21]:

1. Laminar flow
2. Unstable Tollmien–Schlichting waves—amplification of small perturbations
3. Three–dimensional waves and vortex formation
4. Vortex decay
5. Formation of turbulent spots
6. Fully turbulent flow

Even in the turbulent boundary layer, there is a small viscous sublayer. The previously mentioned no-slip condition must be maintained. In the turbulent boundary layer, the Blasius and Falkner–Skan boundary-layer models are no longer valid. The turbulent boundary-layer mean velocity profile can be described using the law of the wall [6]. However, this description is not sufficient for studying the aeroacoustics of the boundary layer because there is no information about the fluctuation component of the velocity (or pressure).

2.7 Stability of the Boundary Layer

An investigation of the stability of the laminar boundary layer when subject to flow perturbation is crucial to determine the location of the start of the natural transition to the turbulent state.

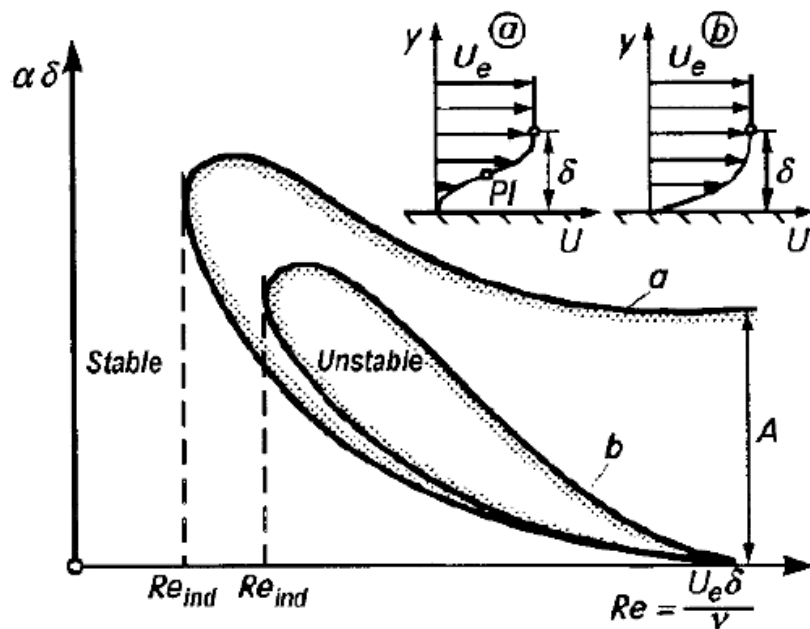


Figure 2.4: Curves of neutral stability for a plane boundary layer [21].

The concept of marginal boundary-layer stability is shown in Fig. 2.4, where there are neutral curves for two different types of velocity profile and instability (*inviscid instability*: curve *a*; *viscous instability*: curve *b*) [21].

2.7.1 Linear Stability

The simplest model of the stability of the boundary layer is *linear stability*. The main concept of the stability analysis is based on the solution of the laminar base flow to which a small disturbance is added. The disturbance can be defined, for example, in the form of a stream function $\Psi(x, y)$ of one mode⁶ [21]:

$$\Psi = \Phi(y) \cdot e^{i(kx - \omega t)} \quad (2.36)$$

where $\Phi(y)$ is the complex amplitude function of the perturbation stream function, k is the streamwise wave number, and ω is the angular frequency. The complex phase speed is $c = \omega/k$. Based on Eq. (2.10a) and Eq. (2.10b), the perturbation velocity field can be described as follows:

$$u' = \frac{\partial \Psi}{\partial y} = \frac{\partial \Phi}{\partial y} \cdot e^{i(kx - \omega t)} \quad (2.37a)$$

$$v' = -\frac{\partial \Psi}{\partial x} = -ik\Phi \cdot e^{i(kx - \omega t)} \quad (2.37b)$$

The complex phase velocity is

$$c = \frac{\omega}{k} = c_r + i \cdot c_i \quad (2.38)$$

where c_r is the real phase velocity of the disturbance and c_i is its growth ($c_i > 0$) or decay ($c_i < 0$) rate.

Assuming the flow is parallel to the x -direction (i.e., $V = 0$), substituting the equations (2.37a) and (2.37b) into the Navier–Stokes equations yields the *Orr–Sommerfeld equation* [13, 27, 30]:

$$(U(y) - c) \left(\frac{\partial^2 \Phi}{\partial y^2} - k^2 \Phi \right) - \Phi \frac{\partial^2 U}{\partial y^2} + \frac{i\nu}{k} \left(\frac{\partial^4 \Phi}{\partial y^4} - 2k^2 \frac{\partial^2 \Phi}{\partial y^2} + k^4 \Phi \right) = 0 \quad (2.39)$$

The trivial solution of Eq. (2.39) is $\Phi(y) = 0$. Nontrivial solutions depend on solving the standard eigenvalue problem and obtaining the associated eigenfunctions Φ [13].

Tollmien–Schlichting Waves

The natural transition from the laminar boundary layer to the turbulent boundary layer starts with the occurrence of Tollmien–Schlichting waves [27]. A Tollmien–Schlichting wave is an unstable perturbation wave, i.e., the perturbations grow either in time or in space [30].

⁶The conventional nomenclature for the perturbation stream function uses the prime symbol (i.e., Ψ'); however, since only this perturbation stream function will be used in the following chapters, the prime symbol is omitted.

These waves are named in honor of Walter Tollmien and Hermann Schlichting⁷, who independently showed that the Orr–Sommerfeld equation has unstable modes for flow without inflection points [30].

■ 2.8 Boundary-Layer Separation

Boundary-layer separation is a phenomenon in which the flow stops following the shape of the immersed body. At the point of separation, the streamlines leave the wall [21]. This point is defined based on the position where the gradient of velocity at the wall normal to the wall is zero.

$$\left(\frac{\partial v_x}{\partial y}\right)_w = 0 \quad (2.40)$$

This is directly connected to the shear stress on the wall, which is, based on Newton’s law of viscosity, also zero:

$$\tau_w(x_{\text{sep}}) = 0 \quad [\text{N m}^{-2}] \quad (2.41)$$

■ 2.8.1 Laminar Boundary-Layer Separation Bubble

If boundary-layer separation occurs while the boundary layer is still in the laminar state, the separation is called *laminar boundary-layer separation*. In the separated region, a transition from a laminar to a turbulent boundary layer may occur. The turbulent detached boundary layer may be able to reattach to the boundary surface [24, 31]. This phenomenon is called a *laminar boundary-layer separation bubble*.

Dovgal et al. [32] conducted a comprehensive study of laminar boundary-layer separation bubbles with non-stationary behavior. One of their important conclusions was the following: “Small-amplitude oscillations excited in the separation bubble produce a disturbance of the natural laminar flow profile which can be an order of magnitude higher than the local amplitude of the instability wave” [32]. This is an important statement because small disturbances can essentially be amplified in the laminar separation bubble. This disturbance itself also has some influence on the transition in the separation bubble.

■ 2.9 Introduction to Acoustics

An introduction to some basic concepts in linear acoustics is needed for a full understanding of the following parts of this thesis. Sound waves are small and weak perturbations of static pressure that propagate through a flow field. For the investigation of sound waves, the density and pressure fields are expressed

⁷Tollmien (1900–1968) and Schlichting (1907–1982) were students of Prandtl [20].

in terms of acoustic density and pressure fluctuations about their respective mean values, ρ_0 and p_0 :

$$\rho' = \rho - \rho_0 \quad (2.42)$$

$$p' = p - p_0 \quad (2.43)$$

The sound wave is propagated to the acoustic far field according to the wave equation,

$$\frac{\partial^2 \rho'}{\partial t^2} - c_\infty^2 \frac{\partial^2 \rho'}{x_i^2} = 0 \quad (2.44)$$

where c_∞ is the speed of sound and small isentropic density perturbations are assumed [12]. The solution of this equation can be obtained using a standard numerical approach (or an analytical approach in a few special cases). The sound source in the wave equation can be incorporated into the boundary conditions or by introducing a source term on the right-hand side of Eq. (2.44):

$$\frac{\partial^2 \rho'}{\partial t^2} - c_\infty^2 \frac{\partial^2 \rho'}{x_i^2} = Q(x_i, t) \quad (2.45)$$

where $Q(x_i, t)$ is the scalar *source term*.

2.9.1 Sound Pressure Level

In many industrial applications, the decibel (dB) unit is used as a scale of *sound level*. This quantity is usually interpreted as the *sound pressure level* (SPL), which is defined in the following equation [33, p. 130]:

$$\text{SPL} = 20 \cdot \log_{10} \left(\frac{p'}{p_{\text{ref}}} \right) \quad (2.46)$$

where the reference pressure is $p_{\text{ref}} = 20 \cdot 10^{-5}$ Pa for air; for water, the reference pressure is $p_{\text{ref}} = 10^{-6}$ Pa [33]. In air, for example, pressure fluctuations of magnitude 1 Pa correspond to an SPL of 94 dB.

The sound could be periodic or a single impulse. In cases of repeating acoustic noise, the *root-mean-square* value of the acoustic pressure (i.e., pressure fluctuations) is used:

$$p'_{\text{RMS}} = \sqrt{\frac{1}{T} \int_0^T (p(t) - p_0)^2 dt} \quad (2.47)$$

where p_0 is the time-averaged value of the pressure (i.e., the mean value). The sound pressure is then obtained using the relation (2.46).

2.10 Summary

In this chapter, the key fluid dynamics concepts relevant to the aeroacoustics of the boundary layer were outlined, as well as some important definitions for acoustics.

The transition from a laminar boundary layer to a turbulent boundary layer and Tollmien–Schlichting waves were described. Tollmien–Schlichting waves are present in the boundary layer from an early phase of the boundary-layer transition. Because of their wavelike character, they are of great importance to the aeroacoustic theory of the boundary layer. Additionally, the effect of laminar separation bubbles in the presence of linear instabilities (disturbances) cannot be neglected.

Chapter 3

Literature Survey and Objectives of the Study: Aerodynamically Generated Sound

3.1 Aerodynamically Generated Sound

In 1952, Lighthill proposed the fundamental theory of aerodynamically generated noise [2, 3]. His theory is today known as *Lighthill's analogy*. A different approach was proposed by Goldstein [34] by linearizing the momentum and continuity equations. Powell [35] introduced the vortex sound theory, which was later extended by Howe [36].

In one of the first applications of Lighthill's analogy, Proudman [37], and later Lilley [38], derived a simple approach to obtain the acoustic power of isotropic turbulence.

3.1.1 Lighthill's Analogy

Lighthill's equation is derived by subtracting the divergence of the momentum equation (Eq. (2.2)) from the time derivative of the continuity equation (Eq. (2.1)) and substituting the density with its fluctuations (Eq. (2.42)):

$$\frac{\partial^2 \rho'}{\partial t^2} - c_\infty^2 \frac{\partial^2 \rho'}{\partial x_i^2} = \frac{\partial^2 T_{ij}}{\partial x_i \partial x_j} \quad (3.1)$$

Here, T_{ij} is the *Lighthill stress tensor*, defined as follows:

$$T_{ij} = \rho v_i v_j - \tau_{ij} + (p' - \rho' \cdot c_\infty^2) \cdot \delta_{ij} \quad (3.2)$$

where τ_{ij} is the *compressive stress tensor* defined in Eq. (2.3), ρ' is the density fluctuation, ρ is the density, p' is the pressure fluctuation, c_∞ is the speed of sound, and δ_{ij} is the Kronecker symbol. Because of the importance of Lighthill's analogy, a full derivation is provided in Appendix A.1.

3.1.2 Solution of Lighthill's Equation

The formal solution of Lighthill's equation (3.1) in the case with no solid boundaries is as follows [4]:

$$\rho'(\vec{x}, t) = \frac{1}{4\pi c_0} \frac{\partial^2}{\partial x_i \partial x_j} \int_V \frac{T_{ij}(\vec{y}, t_r)}{r} dV(\vec{y}) \quad (3.3)$$

where $r = |\vec{x} - \vec{y}|$, $t_r = t - r/c_0$, and c_0 is the speed of sound.

Curle [4] derived a formal solution of Lighthill's equation in the presence of a solid boundary:

$$\rho'(\vec{x}, t) = \frac{1}{4\pi c_0} \frac{\partial^2}{\partial x_i \partial x_j} \int_V \frac{T_{ij}(\vec{y}, t_r)}{r} dV(\vec{y}) - \frac{1}{4\pi c_0} \frac{\partial}{\partial x_i} \int_S \frac{P_i(\vec{y}, t_r)}{r} dS(\vec{y}) \quad (3.4)$$

where $P_i = -n_j p_{ij}$ is the force per unit area exerted on the fluid by the solid boundaries in the direction x_i [4]. This solution was later extended by Ffowcs Williams and Hawkins [5] for a surface in arbitrary motion.

Curle's solution (3.4) of Lighthill's equation (3.1) is sometimes called *Curle's analogy*. The first term on the right-hand side is the sum of all quadrupoles, while the second term consists of dipoles. This second term accounts for all the diffraction and reflection of the quadrupoles at the solid boundary [4, 39, 40].

This solution is convenient because, for many industrial applications, the first term is negligible and so the numerical solution consists only of the surface integral of pressure fluctuations. Nevertheless, to understand the mechanism of noise generation in the boundary layer, it is necessary to evaluate the source term in Lighthill's equation. However, it must be remembered that all source terms in the boundary layer are reflected by the solid surface.

3.1.3 Howe Theory

Powell [35] discussed the significance of vorticity for incompressible fluids in motion. His idea was later extended by Howe [36]. For a low Mach number, a constant mean density value, and zero entropy fluctuations (i.e., an isentropic flow field), the Howe equation takes the following form [12]:

$$\frac{1}{c_\infty^2} \frac{\partial^2 h_0}{\partial t^2} - \frac{\partial^2 h_0}{\partial x_i^2} = \nabla \cdot (\vec{\omega} \times \vec{v}) \quad (3.5)$$

This wave equation is very similar to the wave equation of Lighthill, Eq. (3.1). In this equation, h_0 is the stagnation enthalpy, and the source term on the right-hand side is the divergence of the Lamb vector (see Section 2.1.4). This approach can be useful in cases where it is possible to calculate the Lamb vector.

3.1.4 Empirical Model of Brooks, Pope, and Marcolini

Unlike the previously mentioned aeroacoustic theories, Brooks, Pope, and Marcolini [41] conducted an extensive experimental study of the *self-noise* of the NACA 0012 airfoil. They investigated the noise generation and emission of this airfoil under different flow conditions, and described five basic *self-noise* mechanisms:

- Turbulent boundary-layer trailing-edge noise
- Separation-stall noise

- Laminar boundary-layer vortex-shedding noise
- Tip vortex formation noise
- Trailing-edge bluntness vortex-shedding noise

For each of these noise generation mechanisms, they published measured (1/3 octave band) SPLs, a proposed scaling method, and a scaled SPL spectrum. Their scaling method is based on the boundary-layer parameters, such as the conventional and displacement thicknesses, and the empirical spectral shape function.

This method is quite effective, and for some applications, it is the only available method [12]. However, this empirical spectral scaling approach is based on the measurement of only one airfoil shape.

3.2 Boundary-Layer Noise

The typical representatives of objects around which a boundary layer develops are flat plates or thin airfoils. The airfoil self-noise mechanism was described by Brooks et al. [41]. The airfoil self-noise directly connected to the boundary layer can be separated into categories based on the mechanism:

- Laminar boundary-layer (instability) noise
- Separated flow noise
- Turbulent boundary-layer noise

Brooks, et al. [41] described *tip vortex formation noise* as one of the airfoil self-noise mechanisms. Since this type of noise is related to the formation of the tip vortex, and not the state of the boundary layer, it is not considered a boundary-layer noise mechanism. Similarly, *trailing-edge bluntness noise* is connected to the formation of vortices behind the airfoil, so is not considered a mechanism for the generation of boundary-layer noise.

Glegg and Devenport [12] proposed a method to evaluate the right-hand side of Lighthill's equation (Eq. (3.1)) for low Mach numbers, in which case the fluid is considered nearly incompressible.

For homentropic flow, it is assumed that pressure fluctuations are directly proportional to density fluctuations [12], as stated in the following equation:

$$p' = \rho' c_\infty^2 \quad (3.6)$$

This condition and the definition of the Lighthill stress tensor (Eq. (3.2)) lead to a modified right-hand side of the wave equation for homentropic flow of an incompressible fluid [12, 42]:

$$Q(x_i, t) = \frac{\partial^2 T_{ij}}{\partial x_i \partial x_j} = \rho_\infty \frac{\partial^2 (v_i v_j)}{\partial x_i \partial x_j} - \mu \frac{\partial^2}{\partial x_i \partial x_j} \left(\frac{\partial v_i}{\partial x_j} + \frac{\partial v_j}{\partial x_i} \right) \quad (3.7)$$

Since the fluid is assumed to be incompressible, the last term of Eq. (3.7) is zero (based on the continuity equation (2.1)):

$$Q(x_i, t) = \frac{\partial^2 T_{ij}}{\partial x_i \partial x_j} = \rho_\infty \frac{\partial^2 (v_i v_j)}{\partial x_i \partial x_j} \quad (3.8)$$

This equation is rather important because no further approximation is made: the only assumptions are incompressible fluid and homentropic flow. The source term is related to the unsteady part of the Reynolds stress of this flow.

Using Reynolds' decomposition $v_i = V_i + v'_i$ and the boundary-layer flow assumptions—two-dimensional flow with $V_2 = 0$, and V_1 being a function of x_2 only—the source term for the boundary-layer noise is as follows (the derivation of this source term is given in Appendix A.2):

$$Q(x_i, t) = 2\rho_\infty \frac{\partial V_1}{\partial x_2} \frac{\partial v'_2}{\partial x_1} + \rho_\infty \frac{\partial v'_j}{\partial x_i} \frac{\partial v'_i}{\partial x_j} \quad (3.9)$$

The first term is called the *mean shear–turbulence interaction term* and the second is the *mean turbulence–turbulence interaction term* [42].

This decomposition was used by Landahl in 1975 [43] to describe *large-scale* damped traveling shear waves and *small-scale intermittent motion*. One of his assumptions for the bursts was that the dimensions of these structures are small compared to the wavelength of radiated sound; it can therefore be treated as a *compact noise source*. The small-scale disturbances are also convected by the large-scale disturbances [43].

■ 3.2.1 Laminar Boundary-Layer Instability Noise

One of the mechanisms of boundary-layer noise that has been described is laminar boundary-layer instability noise. The first systematic experimental study was carried out by Paterson et al. [44] in 1973 on NACA 0012 and NACA 0018 airfoils. Based on their experimental investigation, they derived a law for the frequency of a discrete tone $f = 0.011U_\infty^{1.5}/(L\nu)^{0.5}$, where U_∞ is the freestream velocity, L is the chord length of the airfoil, and ν is the viscosity. This is also related to the Strouhal number¹ of the vortex street, so they suggested that the noise was generated by the vortex wake behind the airfoil. The dependence of the emitted acoustic frequency on velocity described by Paterson et al. [44] is shown in Fig. 3.1.

¹The Strouhal number is given by $St = 2 \cdot f \cdot \delta / U_\infty$, based on the dimension of twice the thickness of the boundary layer at the trailing edge [44].

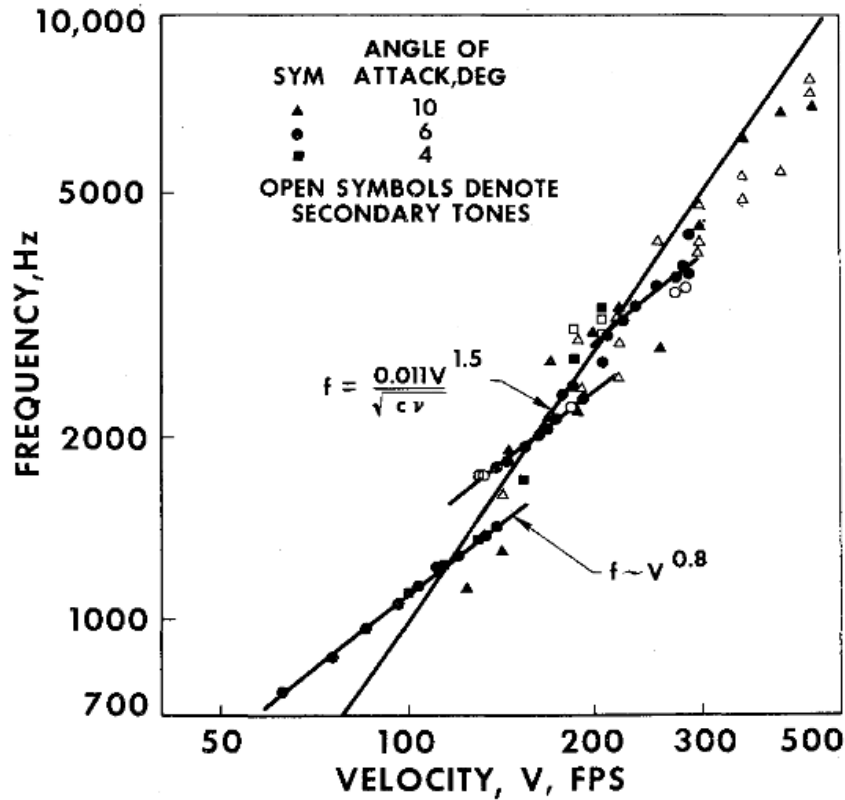


Figure 3.1: Laminar boundary-layer vortex-shedding noise as it was observed by Paterson in 1973 [44].

This generation mechanism was argued against by Tam [45], who in 1974 proposed a *self-excited feedback loop* formed by the acoustic field, the boundary layer, and the wake flow. Tam showed that the primary and secondary frequencies observed by Paterson et al. lie in the hydrodynamic instability region of the Blasius boundary-layer profile.² The proposed noise source is located downstream in the wake, in the region where the instabilities of the boundary layer cause strong lateral vibration.

Longhouse [46] experimentally investigated the vortex-shedding noise for axial fans and concluded that it is significantly reduced when the boundary layer is tripped. This finding is in agreement with that of Paterson et al. To observe the vortex-shedding noise, the boundary layer at the trailing edge must not be in the turbulent state.

Arbey and Bataille [47] (in 1983) found discrepancies between Tam's feedback loop and Fink's theory [48], and proposed a new phase-loop condition for discrete frequencies:

$$\frac{f_n L}{c_r} \left(1 + \frac{c_r}{c_\infty - U_\infty} \right) = n + \frac{1}{2} \quad (3.10)$$

²Paterson et al. based their research on NACA 0012 and NACA 0018 airfoils. The Blasius boundary-layer velocity profile is a rough approximation of the velocity profiles for these airfoils.

where L is the feedback length, c_r is the convective disturbance velocity, c_∞ is the speed of sound, and U_∞ is the freestream velocity.

Lowson et al. [49] obtained experimental data and discovered an occurrence of Tollmien–Schlichting waves in the boundary layer of NACA 0012 without vortex-shedding noise. Therefore, the presence of the Tollmien–Schlichting waves in the boundary layer is not a sufficient condition for vortex-shedding noise. After further study, they found a correlation between the existence of a laminar separation bubble and the occurrence of laminar vortex-shedding noise.

Nash et al. [50] conducted laser Doppler anemometry and acoustic measurements, which showed a high correlation between strongly amplified instabilities and the trailing-edge separated flow region on the pressure surface and the acoustic field. The same authors conducted deeper theoretical work in [51] and connected the frequency of vortex-shedding noise to the frequency of instabilities (i.e., Tollmien–Schlichting waves) on the pressure surface of the airfoil. They also identified an important role for the laminar separation bubble, which is needed to amplify the incoming Tollmien–Schlichting waves.

Desquesnes et al. [52] performed direct numerical simulation (DNS) of the two-dimensional compressible Navier–Stokes equations. One of their conclusions was the determination of the role of the suction side, which was neglected by the previous researchers. One of their hypotheses was that the phase change of hydrodynamic instabilities on the pressure and suction sides affects the amplitude of the sound wave.

Kingan and Pearse [53] used the XFOIL software, by M. Drela [25], to determine the *shape parameters*, and thus the *Falkner–Skan velocity profiles*, along the pressure side of an airfoil. These velocity profiles were used to solve the problem of linear stability (Orr–Sommerfeld equation) and find the modes of the Tollmien–Schlichting waves, which they connected with the frequency of the vortex-shedding noise.

Plogmann et al. [54] conducted an experimental study of NACA 0012 using the oil-flow visualization technique. They confirmed previous findings on the existence of a laminar separation bubble near the trailing edge and the effect of tripping the boundary layer to mitigate this type of noise. They investigated the influence of suction-side tripping near the leading edge on the main feedback loop. However, they did not observe any difference in the tonal noise produced by the laminar boundary-layer vortex shedding.

Chong et al. [55] conducted experimental research on laminar boundary-layer instability noise. They found that the SPL of the instability noise may not be determined solely by Tollmien–Schlichting wave amplification. Chong et al. [56] also investigated the tonal noise generated by the airfoil if the trailing edge is serrated and found, significantly, that the serration reduces this noise.

Golubev et al. [57] performed a remote microphone probe (RMP) measurement on the NACA 0012 airfoil to determine wall-pressure spectra and compare them to the far field. Furthermore, the effects of weak upstream turbulence were studied, with the conclusion that suppression of tonal noise

is related to acoustic feedback.

Pröbsting et al. [58, 59] experimentally investigated tonal noise generation in 2014. Their research aimed to provide an experimental background for the DNS performed by Desquesnes et al. [52] using the particle image velocimetry (PIV) method. They concluded that multiple tones arise not only from phase modulation of fluctuations (as proposed by Desquesnes et al. [52]) but also from periodic modulation of the fluctuation amplitude. Pröbsting and Yarusevych [60] investigated the laminar separation bubble in more detail using two-component PIV measurements. They stated that amplified disturbances in the laminar separated bubble play a crucial role in the mechanism of the boundary-layer transition and that they can create *acoustic feedback*.

In 2019, Arcondoulis et al. [61] studied a dual acoustic feedback mechanism. Based on their findings, they proposed a variation of the original feedback model of Arbey and Bataille (see Fig. 3.2):

$$f_n(Re, \alpha) = \frac{c_r(Re, \alpha)}{L_{Sp+s}(Re, \alpha)} \left(n + \frac{1}{2} \right) \left(1 + \frac{c_r(Re, \alpha)}{c_\infty - U_\infty} \right)^{-1} \quad (3.11)$$

They used the distance from the boundary-layer separation point to the trailing edge L_S as the feedback length. They also proposed an alternative empirical feedback length based on the primary measured frequency.

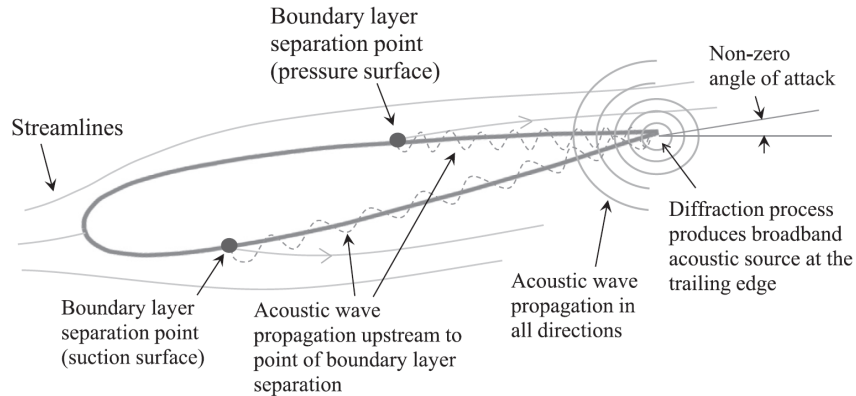


Figure 3.2: Dual-feedback model proposed by Arcondoulis et al. [61].

Gelot and Kim [62] performed a large-eddy simulation (LES) on a symmetric Joukowski airfoil to study the effects of the serrated trailing edge on acoustic feedback. They were able to extract the acoustic expansion wave from field fluctuations and describe the acoustic feedback loop. Their results were in agreement with the findings of Chong et al. [56].

Jaiswal et al. [63] experimentally investigated a controlled-diffusion airfoil using tomographic PIV and remote microphone probes. Based on the remote microphone probe measurement, they verified the existence of an acoustic feedback loop.

Redonnet et al. [64] carried out measurements on a NACA 0021 airfoil in a hard-walled closed-vein wind tunnel at Hong Kong University. They found that the effects of the installation could affect the aeroacoustic analysis, and that the acoustic feedback might be influenced, for example, by the side plates³ of an airfoil.

Laminar Boundary Layer—Instability Noise

The laminar boundary-layer vortex-shedding noise is directly connected to the instabilities in the laminar boundary layer (Tollmien–Schlichting waves). These instabilities are amplified by the laminar separation bubble. The boundary layer eventually reattaches to the surface, and as the instability moves past the trailing edge, it generates an omnidirectional noise source with a phase shift, which affects the point of boundary-layer separation and the boundary-layer instabilities. However, the actual primary acoustic source may not be located directly at the trailing edge, but a short distance downstream [52]. The transition in the boundary layer to the turbulent state causes the acoustic feedback of the Tollmien–Schlichting waves to break.

3.2.2 Turbulent Boundary-Layer Trailing-Edge Noise

Ffowcs Williams and Hall [65] discussed the importance of edge scattering. They showed that the acoustic field generated from edge scattering is more powerful than the acoustic field defined by Lighthill (Eq. (3.1)), even after incorporating reflections from the solid wall [65]. This makes the edge scattering (or trailing-edge noise) the most important component of the noise generation around the airfoil in most practical situations.

Chase [66] calculated the acoustic spectrum and intensity caused by diffraction at the trailing edge. The acoustical properties were obtained on the basis of the wall-pressure spectrum of the turbulent boundary layer. Christopher Tam [67] showed that, based on the knowledge of an empirical wall-pressure cross-correlation function, it is possible to find the directivity pattern and the noise power spectrum in the acoustic far field.

Amiet [68] proposed a theoretical method to estimate the spectral density of the acoustic power emitted from a solid surface in a turbulent stream based on the Kármán spectrum of turbulence. Amiet also studied the influence of the trailing edge and extended his previous paper in [69], using a method similar to that of Chase [66] but with different assumptions: a non-zero mean flow assumption, a different response function, and an assumption of equal radiation to the upper and lower regions from the trailing edge.

Schlinker and Amiet [70] performed an experimental and analytical study of trailing-edge noise. They assumed the boundary-layer thickness to be

³The most common experimental setup for airfoil testing is with the parallel side plates and the ends of the airfoil to avoid the three-dimensional effects caused by the different pressures on the suction and pressure surfaces. In all the reviewed research papers, there was no indication of a different setup.

an important quantity that controls noise generation in the boundary layer. They also proposed a scaling law based on the Strouhal number for the overall SPL.

Marsden et al. [71] conducted a large-eddy simulation of NACA 0012 for a chord-based Reynolds number of 500 000. For noise computations conducted directly, without using an acoustic analogy, their results are comparable to the experimental results of Brooks et al. [41]. Since a transition to a turbulent state was present, they observed no discrete tone connected with the previously described vortex shedding.

Another numerical simulation of the Navier–Stokes equations for compressible fluid and a large-eddy simulation were performed by Gloerfelt and Berland [72, 73, 74]. Their results indicate a strong potential for direct noise calculation (DNC) with large-eddy simulation.

Devenport et al. [75] conducted experimental research on the noise generated by turbulent flow on a rough surface. They found that even smooth surfaces produce noise, implying the presence of scattering as a source mechanism. The wall-pressure fluctuations were measured using microphones embedded in pinholes in the rough surface. They stated that the roughness noise is of a dipole nature.

Küçüksöğüt et al. [76] performed a RANS simulation incorporating Amiet’s theory with different empirical models of wall-pressure fluctuations. Furthermore, they investigated the sensitivity of the acoustic model to the boundary-layer thickness, finding that two out of six investigated spectral models are insensitive to the boundary-layer thickness. In a recent study, Glegg et al. [42, 77] discussed a different approach to modeling the source term. They showed that the surface pressure can be estimated based on the vorticity outside the viscous sublayer.

■ 3.2.3 Summary

The aeroacoustics of the boundary layer is a rapidly evolving field. The range of computational methods is still limited. There are established approaches of large-eddy simulations for direct noise calculations, or RANS simulation using Curle’s solution (i.e., based on pressure fluctuations on the boundary surface).

It has been shown that a non-negligible part of the boundary layer noise is the trailing-edge noise. The trailing edge is important regardless of whether the noise mechanism is based on linear disturbances or non-linear turbulence–turbulence interaction noise. Some of the noise generation mechanisms are not yet fully understood, and there is still room for further improvement and development, not only in the computational and experimental methods but also in the theoretical and analytical approaches.

3.3 Objectives of the Thesis

This chapter summarizes key findings on the subject of boundary-layer aeroacoustics. Based on this literature survey, the following **hypothesis** is formulated:

In a laminar boundary-layer regime, the acoustic source is created by a velocity perturbation. If the perturbation is assumed to be of a single mode, the linear Orr–Sommerfeld equation can be used to estimate the acoustic source term of Lighthill’s equation for the boundary layer to obtain the peak tone emitted by the laminar boundary layer.

To validate this hypothesis, the following constituent **objectives** of the thesis are formulated:

- Description of the aeroacoustic footprint of a boundary layer experiencing linear instabilities in a laminar regime before the transition to a turbulent regime
 - Theoretical description of the aeroacoustic sources caused by linear instabilities in the boundary layer
 - Proposal of a frequency model for the prediction of laminar boundary-layer instability noise
- Experimental investigation of the boundary-layer instability noise
 - Design of an experiment to validate the obtained theoretical results
 - Further examination of the experimental data—using the experimental data to determine the acoustic feedback length
- Validation of the proposed model and experimental results
 - Validation of the proposed theoretical frequency model and experimental results on the NACA 0012 airfoil with the empirical model

These objectives can be divided into two parts, **the extension of the current theoretical findings** and **the setup of the experimental method**. The theoretical part of this thesis should bring new insight into the frequency of sound emitted by a laminar boundary layer with linear instabilities.

For a turbulent boundary layer, methods have already been established, as described in Section 3.2.2, so the thesis is focused only on the laminar boundary layer (with separation).

Methods for Achieving the Objectives

The theoretical description of the acoustic footprint of the boundary layer will be based on studying linear instabilities in the boundary layer, i.e., the spatial

solution of the Orr-Sommerfeld equation. The solution of the Orr-Sommerfeld equation will be used with the source term of Lighthill's equation for the boundary layer to obtain the point acoustic source. These acoustic sources will then be evaluated to obtain the frequency footprint of the boundary layer. For the case study, the NACA 0012 airfoil is chosen, due to the availability of an empirical model of Brooks, Pope, and Marcolini [41]. The BPM empirical model of NACA 0012 is quite extensive and will be used for the validation and comparison of the proposed frequency model.

The experimental part will include measurement of acoustic pressure using built-in microphones on the NACA 0012 airfoil. These results will be used to confirm the theoretical frequency model and analyze the instability feedback length.



Chapter 4

Laminar Boundary-Layer Instability Noise

The common conception of the laminar boundary layer does not incorporate disturbances. From the point of view of fluid dynamics, this assumption causes no problems and is an adequate simplification of the flow in the boundary layer. However, regarding the aeroacoustic footprint, this is not an entirely valid assumption. A laminar boundary layer without disturbances does not generate any noise, and even with a small perturbation (a perturbation that is damped and does not cause a transition to a turbulent boundary layer) in the flow field, the laminar boundary layer emits a very weak acoustic wave.

These disturbances become more important when they grow in space, i.e., when they are spatially unstable. To analyze the stability of the disturbances, the velocity profile in the boundary layer is required. In Section 2.5.2, the Falkner–Skan boundary layer velocity model was introduced. Kingan et al. [53] proposed a promising method based on solving the spatial instability problem of the Orr–Sommerfeld equation using Falkner–Skan velocity profiles based on knowledge of the shape factor of the boundary layer. The shape factor can be obtained experimentally or by using a computational approach, such as XFOIL. Kingan originally proposed this method in his thesis [78]; however, a detailed analysis of the solution was not presented. A minor objective of this thesis is to validate Kingan’s approach to obtaining the frequency of maximal spatial growth. Another approach to prediction of boundary-layer instability noise is based on the empirical model of Brooks, Pope, and Marcolini [41] (the BPM model). The comparison of the BPM model to experimental results was presented in [A1]; however, this paper does not compare the BPM model to the solution based on maximal spatial growth of Tollmien–Schlichting waves.

To utilize the general approach to the boundary-layer instability noise, first, the velocity profiles along a flat plate or airfoil need to be obtained. For this task, the Falkner–Skan boundary-layer model is used as a function of the shape factor. With knowledge of the velocity profile, the standard spatial stability equation is solved. However, due to the lack of data in the literature for validation of the spatial stability problem, the neutral curve obtained from the spatial stability analysis is compared to the neutral curve obtained from the temporal stability. With the verified solution method for the Orr–Sommerfeld equation of spatial stability, it is possible to obtain the

most amplified frequency along the airfoil or flat plate. This solution is also accompanied by a novel approach that utilizes the linear disturbances in the boundary layer as acoustic sources.

4.1 Falkner–Skan Laminar Velocity Profiles

The Falkner–Skan boundary layer has already been briefly introduced. Equation (2.34) is an ordinary differential equation with parameter β , which defines the velocity profile and is related to the shape factor H . According to Hartree [28], and also discussed in [21], when the parameter β is greater than zero, there is only one solution for the shape factor H , but when β is negative, there are two solutions—one for positive shear stress and one for negative shear stress. Hartree [28] stated that the Falkner–Skan velocity profiles are also valid in laminar separation, where there is a negative shear stress:

$$\left(\frac{du}{dy}\right)_w = \frac{1}{\mu}\tau_w \quad (4.1)$$

Based on Eq. (4.1) and the previously stated conditions for shear stress on the wall in laminar separation, the solution of the Falkner–Skan equation can be divided into two parts:

- $\left(\frac{du}{dy}\right)_w > 0$: For given β , the first derivative of the velocity on the wall must be found by enforcing the boundary conditions.
- $\left(\frac{du}{dy}\right)_w < 0$: The (negative) first derivative of the velocity on the wall is given and β is found by enforcing the boundary conditions.

These require partially different approaches to obtain the Falkner–Skan velocity profile based on the shape factor. These approaches are discussed in more detail in Section 4.1.1.

For the interpretation of the velocity profile in the following analysis, the length scale δ_L of the boundary-layer thickness must be precisely defined. The well-defined boundary layer thickness is the displacement thickness, as given by Eq. (2.24). The length scale δ_L can be defined as follows:

$$\eta_{\delta^*} = \frac{\delta^*}{\delta_L} \quad (4.2)$$

where η_{δ^*} is the non-dimensional boundary-layer thickness based on the Falkner–Skan velocity profile and δ^* is the boundary-layer displacement thickness based on an experimental measurement or computer simulation. Using the properties of function $f(\eta)$ (see Eq. 2.31) of Falkner–Skan equation, the length scale is

$$\delta_L = \frac{\delta^*}{\int_0^\infty (1 - \partial f / \partial \eta) d\eta} = \frac{\delta^*}{\eta_{\delta^*}} \quad (4.3)$$

The velocity profile of the boundary layer is now given by three well-defined parameters: the non-dimensional shape factor H [1], the dimensional displacement thickness δ^* [m], and the velocity outside the boundary layer U_e [$\text{m} \cdot \text{s}^{-1}$].

■ 4.1.1 Solution of the Falkner–Skan Equation

The Falkner–Skan equation (2.34) is an ordinary differential equation, and it can be reduced to a system of first-order differential equations by making the following substitution:

$$f(\eta) = a_1(\eta) \quad (4.4a)$$

$$\frac{\partial f(\eta)}{\partial \eta} = a_2(\eta) \quad (4.4b)$$

$$\frac{\partial^2 f(\eta)}{\partial \eta^2} = a_3(\eta) \quad (4.4c)$$

The corresponding system of first-order ordinary differential equations (to Eq. (2.34)) is as follows:

$$f_1(\eta, a_1, a_2, a_3) = \frac{\partial a_1}{\partial \eta} = a_2 \quad (4.5a)$$

$$f_2(\eta, a_1, a_2, a_3) = \frac{\partial a_2}{\partial \eta} = a_3 \quad (4.5b)$$

$$f_3(\eta, a_1, a_2, a_3) = \frac{\partial a_3}{\partial \eta} = -a_1 \cdot a_3 - \beta \cdot (1 - a_2^2) \quad (4.5c)$$

The boundary conditions are then $a_1(0) = 0$, $a_2(0) = 0$ (the no-slip condition), and $a_2(\eta \rightarrow \infty) = 1$. The latter condition means that the velocity has reached the freestream velocity; for a practical solution, the infinity is replaced with $\eta = 25$. In the following sections, it will be shown that the conventional non-dimensional boundary-layer thickness δ_η is usually below 10. Since the boundary condition for a_3 is not known, this is not an initial value problem, but a boundary value problem.

The function a_3 is directly proportional to the shear stress. For a positive Hartree parameter β , there exists only one solution for $a_3(0)$ [28], and the shear stress (i.e., $a_3(0)$) is positive. On the other hand, for a negative Hartree parameter β , there exist two solutions for $a_3(0)$, one negative and one positive [28, 79]. Stewartson [79] provided a proof that there is no solution to the Falkner–Skan equation with the given boundary conditions for $\beta < \beta_0$. Here, β_0 is the Hartree parameter for zero shear stress at the wall, i.e., for $a_3(0) = 0$. This parameter can be computed or taken from the literature: according to [79], $\beta_0 = -0.1988$.

The Falkner–Skan velocity profile is needed for a full solution of the boundary-layer stability. Therefore, it is essential to find a map between the shape factor H and the Hartree parameter β . The shape factor H provides a unique Falkner–Skan velocity profile, unlike the Hartree parameter β .

■ Positive Shear Stress

The solution for **positive shear stress** at the wall (i.e., $a_3(0) > 0$) for a known Hartree parameter β is found using the *shooting method* to obtain a_3 and reduce the boundary value problem to an initial value problem, which is solved using the Runge–Kutta method (RK4).

Negative Shear Stress

The solution for **negative shear stress** at the wall (i.e., $a_3 < 0$) for the unknown (negative) Hartree parameter β is slightly different. Instead of using the shooting method to reduce the boundary value problem to an initial value problem, the system of ODEs is solved directly as an initial value problem with given negative $a_3(0)$. The boundary condition at the edge of the boundary layer, $[1 - a_2(\eta \rightarrow \infty)] = 0$, is enforced by finding the corresponding β . This can be done using an appropriate root-finding algorithm. For the following results, the *trust region reflective method* is used to obtain the parameter β , as implemented in the SciPy Python package. This approach seems to be robust; however, the solution is sensitive to the initial guess for the Hartree parameter [80]. For a given negative a_3 , it is possible to obtain more than one solution for β and thus more than one value of the shape factor (see Fig. 4.1).

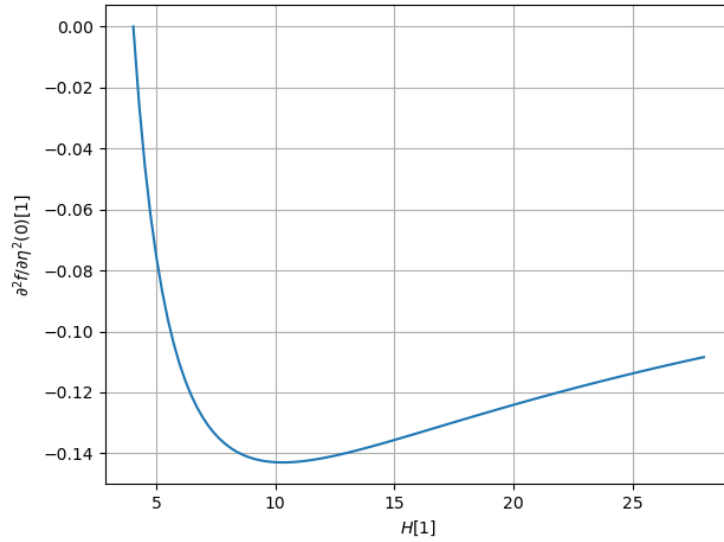


Figure 4.1: Detail at local minimum of $\frac{\partial^2 f}{\partial \eta^2}(0)$ as a function of shape factor.

Based on the discussion above, it can be hypothesized that the shear stress at the wall as a function of shape factor is not monotonic and that a local minimum value of a_3 must exist.

Using the method described above, it was found that the minimum possible value of $a_3 = \frac{\partial^2 f}{\partial \eta^2}(0)$ is -0.142978 , which corresponds to a value of $H = 10.308351$ for the shape factor. This local minimum is shown in Fig. 4.1 and in Fig. 4.2. This also explains why the solution is sensitive to the initial guess.

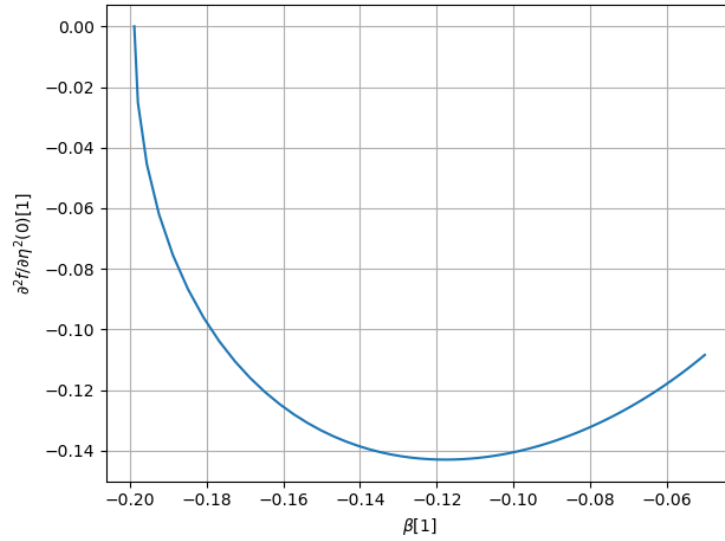


Figure 4.2: Local minimum of $\frac{\partial^2 f}{\partial \eta^2}(0)$ as a function of Hartree parameter β .

These findings are in agreement with the partial solutions of Stewartson [79], Cebecci and Keller [80], and Christian et al. [81]. However, they did not provide this deeper insight into the local extremum of the negative shear stress.

4.1.2 Summary

Based on the described method, the mapping between the Hartree parameter β and the shape factor H has been established. In Fig. 4.3, an H – β plot is shown as a graphical representation of this relationship.

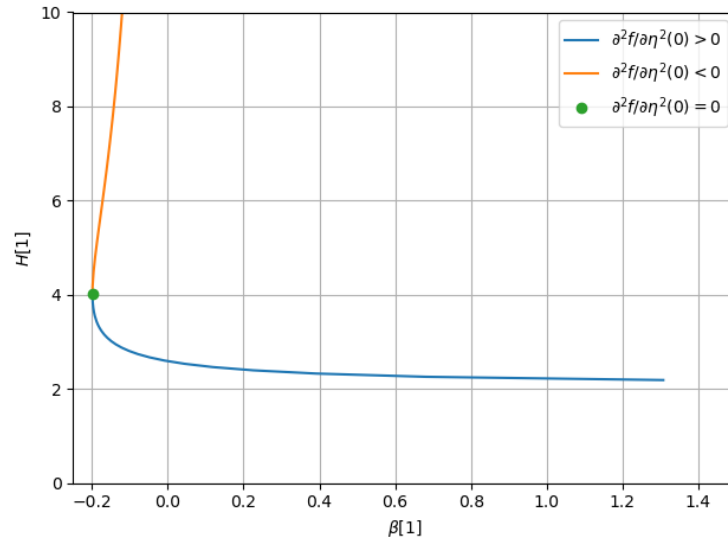


Figure 4.3: The H – β plot for the Falkner–Skan boundary layer.

Some selected points of interest of the solution for different Falkner–Skan velocity profiles are listed in Table 4.1.

Table 4.1: Selected parameters of the Falkner–Skan equation for different shape factors.

H	β	$\frac{\partial^2 f}{\partial \eta^2}(0)$
2.190	1.307	1.3880
2.591	0	0.4696
3.800	-0.197657	0.029936
4.029226	-0.198838	0
4.100	-0.198747	-0.007966
5.000	-0.188724	-0.075630
10.308351	-0.117706	-0.142978

In Fig. 4.4, the second derivative of the solution of the Falkner–Skan equation is plotted, providing an intuitive understanding of the parameter's value. A shape factor H below $H_0 = 4.029226$ corresponds to an attached laminar boundary layer, and a value above H_0 is characteristic of a local velocity profile in the laminar separation bubble. The solution for the shape factor above H_0 can be found based on further splitting the range at the value of the shape factor 10.308351. It is subject to further discussion whether the solution for a shape factor above 10.308351 is required. Since this value of the shape factor would mean long laminar separation, it is not expected that velocity profiles with a shape factor above 10.308351 are needed.

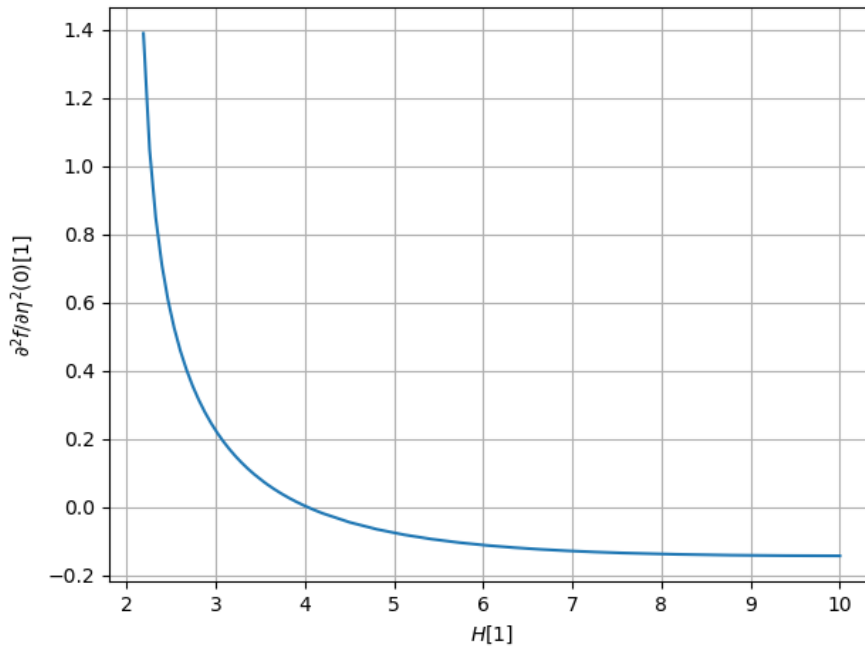


Figure 4.4: Dependency of $\frac{\partial^2 f}{\partial \eta^2}(0)$ on the shape factor H .

The solution of the Falkner–Skan equation based on the shape factor has been established. This solution was designed to be robust, sacrificing computational time. This method has been validated against values from the literature and is an appropriate way to obtain the velocity profile, which will be required for elucidation of the aeroacoustic characteristics of the laminar boundary layer.

4.2 Stability: Orr–Sommerfeld Equation

When the velocity profile is known, a solution of spatial stability (i.e., a solution of the Orr–Sommerfeld equation) can be obtained. To solve the Orr–Sommerfeld equation, the parameter scale based on the scaling factors of the Falkner–Skan equation described in Section 4.1 is used. Due to this scale, the Orr–Sommerfeld equation can be solved non-dimensionally in general (non-dimensional values are denoted by subscript η). For some basic analysis, the variables related to the displacement thickness δ^* are used, and are denoted with the corresponding subscript:

$$k_\eta = k \cdot \delta_L = \frac{k\delta^*}{\eta\delta^*} \quad (4.6a)$$

$$\omega_\eta = \omega \cdot \frac{\delta_L}{U_e} = \omega\delta^* \cdot \frac{1}{U_e \cdot \eta\delta^*} \quad (4.6b)$$

$$U_\eta = f' = \frac{U}{U_e} \quad (4.6c)$$

$$c_\eta = \frac{c}{U_e} \quad (4.6d)$$

A similar scaling can be applied to the variables that are already non-dimensional, such as the Reynolds number:

$$Re_{\delta^*} = \frac{U_e \cdot \delta^*}{\nu} = Re_{\eta\delta^*} \cdot \eta\delta^* \quad (4.7)$$

The Orr–Sommerfeld equation (2.39) multiplied by δ_L^2/U_e , and with the substitutions introduced in equations (4.6), is then

$$(U_\eta - c_\eta) \left(\frac{\partial^2 \Phi}{\partial \eta^2} - k_\eta^2 \Phi \right) - \Phi \frac{\partial^2 U_\eta}{\partial \eta^2} + \frac{i}{Re_{\eta\delta^*} \cdot k_\eta} \left(\frac{\partial^4 \Phi}{\partial \eta^4} - 2k_\eta^2 \frac{\partial^2 \Phi}{\partial \eta^2} + k_\eta^4 \Phi \right) = 0 \quad (4.8)$$

The solution of the Orr–Sommerfeld equation (4.8) described in the following sections is based on a global approach using the Chebyshev matrix method [82].

4.2.1 Chebyshev Method

The amplitude function Φ can be approximated by a Chebyshev expansion [30].

$$\Phi(\eta) = \sum_{n=0}^N a_n \cdot T_n(\hat{\eta}) \quad (4.9)$$

where $T_n(\hat{\eta})$ are Chebyshev polynomials. Chebyshev polynomials can have different forms, of which the best-known definition is as follows [30]:

$$T_n(\hat{\eta}) = \cos(n \cdot \cos^{-1}(\hat{\eta})) \quad (4.10)$$

The N Chebyshev collocation points are defined in the domain $[-1, 1]$ and are unevenly spaced according to the cosine function (4.11). These points are also known as *Gauss–Lobatto points*, and are defined as follows [30]:

$$\hat{\eta}_k = \cos\left(\frac{k \cdot \pi}{N}\right), k = 0, \dots, N \quad (4.11)$$

The Chebyshev domain is then the finite domain $\hat{\eta} \in [-1, 1]$, while the boundary layer is the semi-infinite domain $\eta \in [0, +\infty)$. The rational map based on [30, p. 486] is introduced:

$$\hat{\eta} = \frac{b \cdot \eta - a}{\eta + a} \quad (4.12a)$$

$$\eta = \frac{a(1 + \hat{\eta})}{b - \hat{\eta}} \quad (4.12b)$$

where a and b are constants based on the required domain resolution,

$$a = \frac{\eta_h \eta_{\max}}{\eta_{\max} - 2 \cdot \eta_h} \quad (4.13a)$$

$$b = 1 + \frac{2a}{\eta_{\max}} \quad (4.13b)$$

and η_{\max} is a point far enough from the surface. The variable η_h defines the range $[0, \eta_h]$ in which half of the points are distributed. Based on the Falkner–Skan velocity profiles analyzed in Section 4.1, the following values of these variables were chosen: $\eta_{\max} = 25$ and $\eta_h = 15$.

The k th derivatives of the approximated amplitude function can be found using the Chebyshev derivative operator $\mathcal{D}^{(k)}$:

$$\Phi^{(k)}(\eta_i) = \sum_{j=0}^N \mathcal{D}_{ij}^{(k)} a_j \cdot T_j(\hat{\eta}_i) \quad (4.14)$$

The derivative operator $\hat{\mathcal{D}}_{ij}$ in the Chebyshev domain is defined as follows:

$$\hat{\mathcal{D}}_{00}^{(1)} = -\hat{\mathcal{D}}_{NN}^{(1)} = \frac{2N^2 - 1}{6} \quad (4.15a)$$

$$\hat{\mathcal{D}}_{ii}^{(1)} = -\frac{\hat{\eta}_i}{2(1 - \hat{\eta}_i^2)} \quad (4.15b)$$

$$\hat{\mathcal{D}}_{ij}^{(1)} = -\frac{c_j}{c_i} \cdot \frac{(-1)^{i+j}}{\hat{\eta}_j - \hat{\eta}_i}, i \neq j, c_0 = c_N = 2, c_i = 1 \quad (4.15c)$$

To transform the derivative operator $\hat{\mathcal{D}}^{(k)} = \hat{\mathcal{D}}^k$ from the Chebyshev domain $\hat{\eta} \in [-1, 1]$ to the semi-infinite domain $\eta \in [0, +\infty]$, the chain rule for derivatives must be applied:

$$\mathcal{D}_{ij}^{(1)} = \frac{d\hat{\eta}}{d\eta} \hat{\mathcal{D}}_{ij}^{(1)} \quad (4.16a)$$

$$\mathcal{D}_{ij}^{(2)} = \left(\frac{d\hat{\eta}}{d\eta}\right)^2 \hat{\mathcal{D}}_{ij}^{(2)} + \frac{d^2\hat{\eta}}{d\eta^2} \hat{\mathcal{D}}_{ij}^{(1)} \quad (4.16b)$$

$$\mathcal{D}_{ij}^{(3)} = \left(\frac{d\hat{\eta}}{d\eta}\right)^3 \hat{\mathcal{D}}_{ij}^{(3)} + 3 \frac{d^2\hat{\eta}}{d\eta^2} \frac{d\hat{\eta}}{d\eta} \hat{\mathcal{D}}_{ij}^{(2)} + \frac{d^3\hat{\eta}}{d\eta^3} \hat{\mathcal{D}}_{ij}^{(1)} \quad (4.16c)$$

$$\mathcal{D}_{ij}^{(4)} = \left(\frac{d\hat{\eta}}{d\eta}\right)^4 \hat{\mathcal{D}}_{ij}^{(4)} + 6 \frac{d^2\hat{\eta}}{d\eta^2} \left(\frac{d\hat{\eta}}{d\eta}\right)^2 \hat{\mathcal{D}}_{ij}^{(3)} + \left(3 \left(\frac{d^2\hat{\eta}}{d\eta^2}\right)^2 + 4 \frac{d^3\hat{\eta}}{d\eta^3} \frac{d\hat{\eta}}{d\eta}\right) \hat{\mathcal{D}}_{ij}^{(2)} + \frac{d^4\hat{\eta}}{d\eta^4} \hat{\mathcal{D}}_{ij}^{(1)} \quad (4.16d)$$

The derivatives of the transformation function are then

$$\frac{d\hat{\eta}}{d\eta} = \frac{a(b+1)}{(a+\eta)^2} \quad (4.17a)$$

$$\frac{d^2\hat{\eta}}{d\eta^2} = -2 \cdot \frac{a(b+1)}{(a+\eta)^3} \quad (4.17b)$$

$$\frac{d^3\hat{\eta}}{d\eta^3} = 6 \cdot \frac{a(b+1)}{(a+\eta)^4} \quad (4.17c)$$

$$\frac{d^4\hat{\eta}}{d\eta^4} = -24 \cdot \frac{a(b+1)}{(a+\eta)^5} \quad (4.17d)$$

Using the derivative operators on the amplitude function, the Orr–Sommerfeld equation (4.8) is

$$\left((U_\eta - c_\eta) (\mathcal{D}^2 - k_\eta^2) - \frac{\partial^2 U_\eta}{\partial \eta^2} + \frac{i}{Re_{\eta\delta^*}} (\mathcal{D}^4 - 2k_\eta^2 \mathcal{D}^2 + k_\eta^4) \right) \Phi = 0 \quad (4.18)$$

In Section 2.7.1, it was stated that there exists a trivial solution $\Phi = 0$, which can be confirmed as a solution of Eq. (4.18). For non-trivial solutions, the following boundary conditions are defined:

$$\Phi(0) = \Phi(\eta_{\max}) = \mathcal{D}\Phi(0) = \mathcal{D}\Phi(\eta_{\max}) = 0 \quad (4.19)$$

The amplitude function is expanded using the Chebyshev series (Eq. (4.9)); this discretization leads to a system of $N + 1$ equations, while four equations are modified for the boundary conditions. Since the boundary conditions are linearly independent (and independent of wave number), it is reduced to a system of $N - 3$ equations. This approach of implementing boundary conditions is described by Danabasoglu and Biringen [83].

■ Implementing the Boundary Conditions

The other way to implement the boundary conditions, without modifying equations, is to directly remove the first and last equations, while the differentiation matrix is modified. This method was proposed by Huang and Sloan [84] and was further described by Trefethen [85]. The principal idea of this method is the assumption that the eigenfunction is interpolated by polynomial of order $\leq N + 1$.

Using the boundary condition $\mathcal{D}\Phi(0) = \mathcal{D}\Phi(\eta_{\max}) = 0$, the modified fourth derivative operator $\hat{\mathcal{D}}^{(4)*}$ is obtained:

$$\hat{\mathcal{D}}_{ij}^{(4)*} = \left[\delta_{ikl}(1 - \hat{\eta}_l^2)(\hat{\mathcal{D}}^4)_{km} - 8\delta_{ikl}\hat{\eta}_l(\hat{\mathcal{D}}^3)_{km} - 12(\hat{\mathcal{D}}^2)_{im} \right] \cdot \left(\frac{\delta_{mjn}}{1 - \hat{\eta}_n^2} \right) \quad (4.20)$$

The symbol δ_{ijk} is a modified version of the Kronecker delta, defined to be zero except when $i = j = k$. Equation (4.20) is valid only for $0 < i, j < N$ and this fourth derivative is used in Eq. (4.16d) instead of the original $\hat{\mathcal{D}}^{(4)}$. To impose the boundary condition $\Phi(0) = \Phi(\eta_{\max}) = 0$ on the system, the first and last rows are removed from the matrices (4.16), so there is no problem with the range of validity of this modified derivative operator. The resulting system of equations is of order $N - 1$.

■ 4.2.2 Temporal Stability

Even though the problem of temporal stability is not essential to obtaining the footprint of the boundary-layer instability noise, it is crucial for the validation of the computational method. The temporal stability results for the Orr–Sommerfeld equation are well known (for example, for the Poiseuille flow [86, 30] and the Blasius boundary layer [30]).

For the temporal stability problem, the wave number $k \in \mathbb{R}$ is given, and the angular velocity $\omega \in \mathbb{C}$ is to be solved. Specifically, the complex phase velocity c is found as an eigenvalue of the Orr–Sommerfeld equation with corresponding eigenfunction Φ . The discretized equation (4.18) can be rewritten in the following matrix form:

$$(\mathbf{C}_1 - c_\eta \cdot \mathbf{C}_0) \Phi = 0 \quad (4.21)$$

where

$$\mathbf{C}_1 = \frac{i}{k_\eta \cdot Re_{\eta_\delta}^*} \left(\mathcal{D}^{(4)} - 2 \cdot k_\eta^2 \cdot \mathcal{D}^{(2)} + k_\eta^4 + U(\mathcal{D}^{(2)} - k_\eta^2 \mathbf{I}) - \frac{d^2 U}{d\eta^2} \mathbf{I} \right) \quad (4.22a)$$

$$\mathbf{C}_0 = \mathcal{D}^{(2)} - k_\eta^2 \mathbf{I} \quad (4.22b)$$

Equation (4.21) can be solved using the *QZ method*¹ for the general eigenvalue problem [87].

¹In this thesis, the described computational methods are implemented using Python and the SciPy module, in which the low-level LAPACK library is interfaced. Therefore, for the solution of a general eigenvalue problem, the function *zgeev* is used.

The implemented temporal stability solver was first validated for the Poiseuille flow. This was chosen because the computational domain $[-1, 1]$ of the Poiseuille flow corresponds to that of the Chebyshev method, so there is no need for domain mapping. However, a more important test is to validate the solution for the Blasius boundary layer with a velocity profile defined via the Falkner–Skan equation. In this way, not only is the solution of the eigenvalue problem checked, but also the domain mapping and the solution to the Falkner–Skan equation.

■ Temporal Stability of the Blasius Boundary Layer

The Blasius boundary-layer profile can be defined as a special case of the Falkner–Skan equation with the Hartree parameter $\beta = 0$. The shape factor of the Blasius boundary layer is $H = 2.56$. In Fig. 4.5, eigenmodes of the Orr–Sommerfeld equation are shown for the Blasius boundary layer with wave number $k_{\delta^*} = 1$ and Reynolds number $Re_{\delta^*} = 800$. These conditions were chosen due to the possibility of comparison with the solution provided by Schmid [30, p. 507]. Solutions based on different orders of polynomials N are also shown.

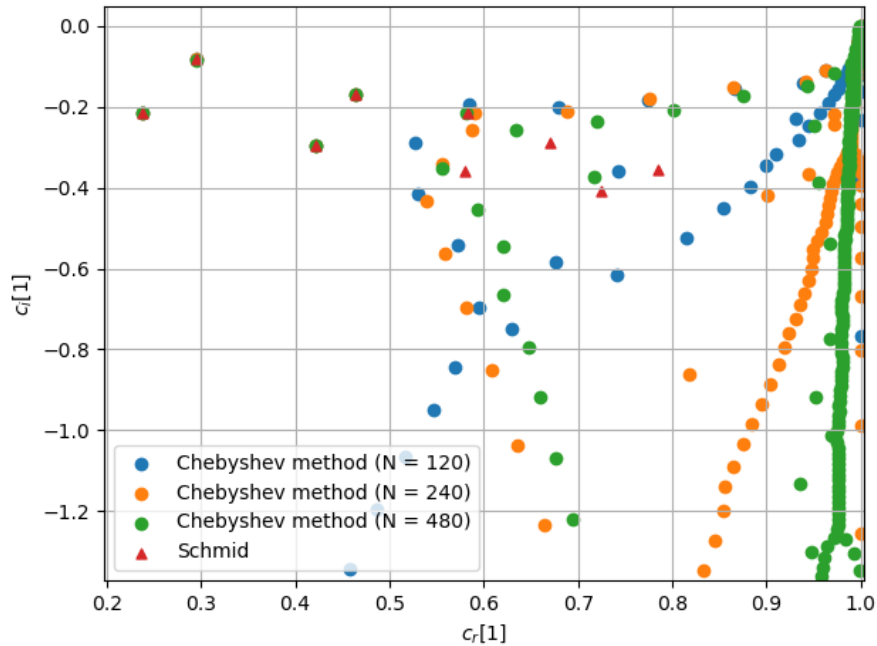


Figure 4.5: Argand diagram of the complex phase velocity as a solution to the temporal stability problem.

According to Schmid [30], the eigenvalues (complex phase velocities) of the Blasius boundary layer, shown in Fig. 4.5, can be divided into two groups. The first group is the *A branch* of the modes, which are also called *wall modes*. The second group is a combination of the *P and S branches* and depends strongly on the numerical method and discretization [30]. The important

properties of A mode are the small phase velocity c_r and the fact that the mode of the Tollmien–Schlichting wave is always A mode.

The leftmost A branch of the eigenmodes in Fig. 4.5 shows agreement between all three tested orders of polynomials (N) and the results from the literature. The boundary-layer flow is stable under these conditions because all modes in the A branch have a negative imaginary part c_i .

The second part (or branch) of this Argand diagram is formed of the continuous spectrum around $c_r \rightarrow 1$. It can be seen that, for a high value of N , the rightmost modes form an almost vertical line. Since the goal is to obtain modes of Tollmien–Schlichting waves, these rightmost modes are not especially important in this thesis; therefore, it should be sufficient to use 120 as the order of the Chebyshev polynomial.

A computational procedure can be used to obtain the mode with the highest growth rate (c_i) in the A branch. The method used to find this eigenmode is based on the phase speed c_r of the modes. Since, in the second branch of the eigenmodes, the phase speed is close to one (or the growth rate has a larger negative value), the condition used to choose the correct mode can be formulated as follows: *The most unstable/least stable mode of the boundary flow is the mode with the highest growth or the lowest decay rate c_i and a phase velocity lower than 0.9 ($c_r < 0.9$).*

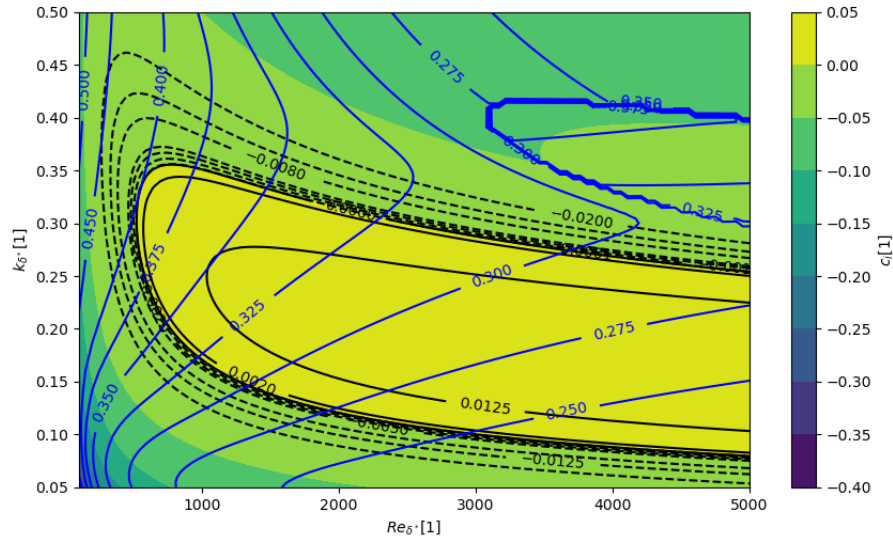


Figure 4.6: Temporal stability of the Blasius boundary layer, i.e., $H = 2.56$, $\beta = 0$. The curves are iso-curves of constant phase velocity (blue) and constant growth/decay rate (black).

In Fig. 4.6, the modes for the range of wave numbers k_{δ^*} and Reynolds numbers Re_{δ^*} are shown. This plot is well known due to the neutral curve that lies between the region of modes with $c_i > 0$ and $c_i < 0$. This neutral curve is also important for validating the method used. The numerical values can be found in Appendix B.1, which are comparable to the results in the literature.

4.2.3 Spatial Stability

The spatial stability problem concerns the growth of disturbances in space. For the solution of this problem, the frequency (or angular velocity ω) is given, and the wave number k (or phase speed c) is assumed to be determined by the solution of the eigenvalue problem. Unfortunately, there is a lack of data in the literature that could be used to validate this. However, the points of the neutral curve are the same for the solution of the temporal and spatial stability problems, and so validation can be performed against the previously obtained neutral curve.

The angular velocity $\omega \in \mathbb{R}$ is given and the wave number $k \in \mathbb{C}$ is found based on the solution of the eigenvalue problem (4.18). In this equation, the wave number k is raised to the fourth power. This complicates the solution because the eigenvalue problem has a fourth-order characteristic polynomial. Haj-Hariri [88] proposed a transformation to reduce the order of the eigenvalue problem, as follows:

$$\Phi = \phi \cdot e^{-k \cdot \eta} \quad (4.23)$$

where ϕ is the *reduced amplitude function*. Substituting Eq. (4.23) into Eq. (4.18) and applying the chain rule for derivatives leads to the new discretized Orr–Sommerfeld equation with a reduced power of k :

$$\left((k_\eta U_\eta - \omega_\eta) (\mathcal{D}^2 - 2k_\eta \mathcal{D}) - k_\eta \cdot \frac{\partial^2 U_\eta}{\partial \eta^2} + \frac{i}{Re_{\eta\delta^*}} (\mathcal{D}^4 - 4k_\eta \mathcal{D}^3 + 4k_\eta^2 \mathcal{D}^2) \right) \phi = 0 \quad (4.24)$$

The unknown wave number k_η now occurs in the Orr–Sommerfeld equation raised to the second power. This leads to a second-order characteristic polynomial (with redefined coefficients \mathbf{C}_0 , \mathbf{C}_1 , and \mathbf{C}_2):

$$\mathbf{C}_2 \cdot k_\eta^2 + \mathbf{C}_1 \cdot k_\eta + \mathbf{C}_0 \quad (4.25)$$

The redefined coefficients of the characteristic polynomial are as follows:

$$\mathbf{C}_2 = 2i \cdot \mathbf{U} \cdot \mathcal{D} + \frac{4\mathcal{D}^2}{Re_{\eta\delta^*}} \quad (4.26a)$$

$$\mathbf{C}_1 = -2i \cdot \omega_\eta \mathcal{D} - i\mathbf{U}\mathcal{D}^2 + i\mathbf{U}'' - \frac{4\mathcal{D}^3}{Re} \quad (4.26b)$$

$$\mathbf{C}_0 = i \cdot \omega_\eta \mathcal{D}^2 + \frac{\mathcal{D}^4}{Re} \quad (4.26c)$$

where \mathbf{U}'' is the matrix of second derivatives of base velocity \mathbf{U} with respect to η . Following the approach proposed by Bridges and Morris [82], the *companion matrix* method is used:

$$(\mathbf{A} - k_\eta \mathbf{B}) = \begin{bmatrix} -k_\eta \phi \\ \phi \end{bmatrix} \quad (4.27)$$

where the matrices \mathbf{A} and \mathbf{B} are constructed based on the coefficient matrices \mathbf{C}_0 , \mathbf{C}_1 , and \mathbf{C}_2 :

$$\mathbf{A} = \begin{bmatrix} -\mathbf{C}_1 & -\mathbf{C}_0 \\ \mathbf{I} & \mathbf{0} \end{bmatrix} \quad (4.28a)$$

$$\mathbf{B} = \begin{bmatrix} -\mathbf{C}_2 & \mathbf{0} \\ \mathbf{0} & \mathbf{I} \end{bmatrix} \quad (4.28b)$$

The solution to the generalized eigenvalue problem (Eq. (4.27)) with matrices \mathbf{A} and \mathbf{B} can be obtained using the same computational method as for the temporal problem, i.e., the QZ algorithm.² The obtained eigenfunction ϕ is then transformed, using Eq. (4.23), to the complex amplitude function Φ .

■ Spatial Stability of the Blasius Boundary Layer

The spatial stability of the Blasius boundary layer is solved in a similar manner to the temporal stability. Using the Falkner–Skan boundary-layer solver with the corresponding parameters, the velocity profile (and the second derivative) is obtained.

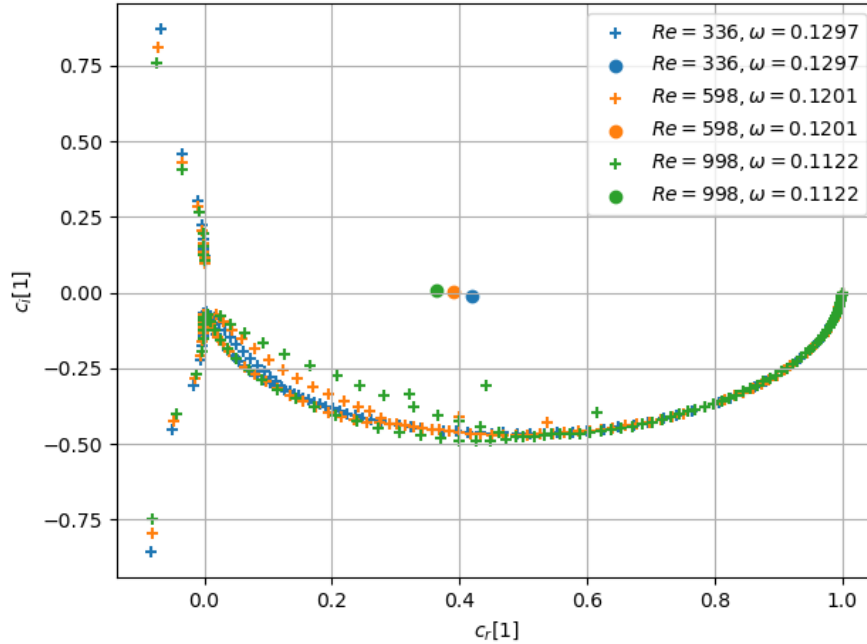


Figure 4.7: Argand diagram of complex phase velocity for the Blasius boundary layer (i.e., $H = 2.56$, $\beta = 0$) for three different cases.

The validation cases were chosen based on the results of Jordinson [89] for three different Reynolds numbers and angular velocities. Solutions of spatial

²The same method *zggeev* of the LAPACK library is used to obtain the results. However, the size of the matrices is $2(N - 1) \times 2(N - 1)$, so the solution requires more computational time than in the case of temporal stability.

stability for these cases are shown in Fig. 4.7 in the Argand diagram of the normalized complex phase velocity c .

In Fig. 4.7, all the computed modes are shown. In all three cases, there is a distinct point (marked by a filled circle in the plot) that corresponds to the most unstable ($c_i > 0$), or least stable ($c_i < 0$) mode.

It is possible to create a diagram with the maximum growth/decay rate of the most unstable (or least stable) disturbance in a manner similar to that used for the temporal stability case. Ranges of ω_{δ^*} and Re_{δ^*} were chosen and this diagram is shown in Fig. 4.8 for the Blasius boundary layer. This diagram can also be obtained for different shape factors, even for the shape factor of the separated laminar boundary layer. Gleyzes et al. [90] predicted marginal stability for values of the shape factor up to 35.94.

The selection of the most unstable (or least stable) mode, which is important to establish the marginal stability, is based on the phase velocity c_r . The real part of the phase velocity of the disturbance is assumed to be in the range $c_r \in (0, 0.9)$.

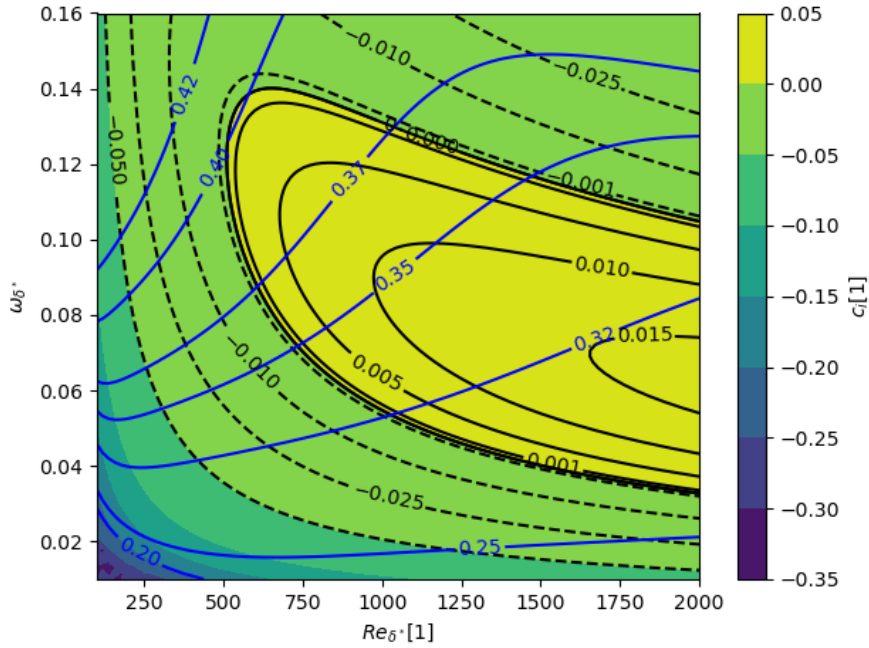


Figure 4.8: Spatial stability of the Blasius boundary layer, i.e., $H = 2.56$, $\beta = 0$. The curves shown are iso-curves of constant phase velocity (blue) and constant growth/decay rate (black).

The corresponding eigenfunctions (or amplitude functions) are also obtained. However, the amplitude functions are not so well-defined. The Orr–Sommerfeld equation (2.39) is a homogeneous linear ordinary differential equation, which means that if $\Phi(y)$ is a solution, then $\kappa \cdot \Phi(y)$ is also a solution, where κ is an arbitrary non-zero constant $\kappa \in \mathbb{C}$. For the rest of this thesis, the notation $\Phi(y)$ is used to refer to the solution for which the condition

$\max |\Phi(y)| = 1$ is satisfied (i.e., it is the eigenfunction normalized to its maximum absolute value³). For example, Jordinson [89] chooses the maximum value of the real part of the eigenfunctions to be one; however, this choice is ambiguous because an arbitrary complex number $x + i \cdot y$ can be multiplied by a complex constant κ such that the equation $x + i \cdot y = \kappa \cdot (y + i \cdot x)$ is satisfied, which swaps the magnitudes of the real and imaginary parts. However, by using the absolute value for subsequent calculations, this ambiguity is removed, because the absolute value of the complex number $x + i \cdot y$ is the same as that of $y + i \cdot x$.

The normalized absolute value of the amplitude function for the Blasius boundary layer is shown in Fig. 4.9. The eigenfunctions correspond to the least stable/most unstable modes of disturbance, which are shown in the Argand diagram in Fig. 4.7. Jordinson [89] obtained a similar result with the maximum value of the amplitude functions slightly below $2\delta^*$.

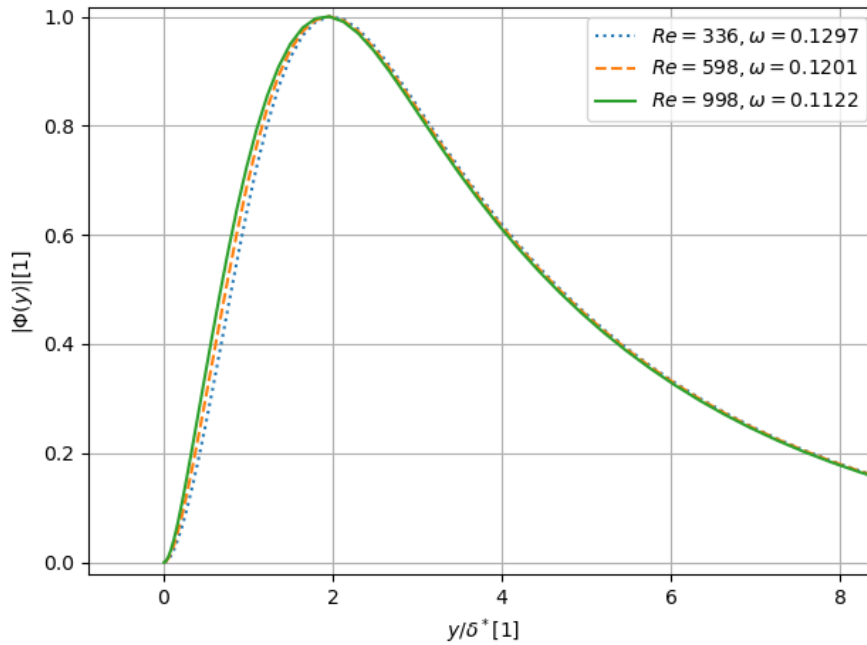


Figure 4.9: Amplitude functions of the least stable/most unstable modes of the Blasius boundary layer, i.e., $H = 2.56$, $\beta = 0$, for three different cases (with the same conditions as in Fig. 4.7).

4.2.4 Conclusion

With the knowledge of the velocity profile (or the parameters of the Falkner–Skan velocity profile—the shape factor H , the displacement thickness δ^* , and the velocity outside the boundary layer U_e) the spatial stability can be solved at a given point of the flat plate (or airfoil). This method to solve the spatial stability problem is designed using the Chebyshev collocation method. The

³Since $\Phi(y) \in \mathbb{C}$, the absolute value refers to the absolute value of the complex number.

results are validated against the available data. The neutral modes of the Blasius boundary layer calculated from the temporal and spatial problem are compared, which is important to validate the chosen approach (the comparison is presented in Appendix B.1). The relative difference between the temporal and spatial solutions is below 0.2%, which is mostly caused by the rounding error.

The method of selecting the most unstable mode (i.e., selecting the mode of the Tollmien–Schlichting wave) or the least stable mode is proposed. This approach is based on the value of the phase velocity of the disturbance. The method of normalizing the amplitude function is described to avoid ambiguity in the following solutions.

■ 4.3 Spatial Instability in the Boundary Layer of an Airfoil

In the previous section, the local stability of the boundary layer was solved. In real scenarios, the boundary layer develops from the leading edge to the trailing edge of a streamlined body.⁴ The airfoil is of finite length, and the usual convention is to use the symbol c to represent the chord length; however, to avoid confusion with the complex phase velocity (and the speed of sound), the symbol L will be used instead.

The values of the three local parameters described in Section 4.2 must be obtained along the contour of the streamlined body, which is assumed to be an airfoil. For airfoils, the widely used and validated software package XFOIL is available [25]. This software uses a panel method with a coupled boundary-layer model [91] to obtain the characteristics of the airfoil and the parameters of the boundary layer.

For validation and demonstration purposes, the well-known NACA 0012 airfoil will be used. For this airfoil, empirical relations are available for aeroacoustic noise [41] and many of the airfoil’s characteristics are also known.

■ 4.3.1 Boundary-Layer Development

The boundary layer on the leading edge is always in a laminar state. Under normal conditions, the laminar boundary layer increases in thickness along the surface. The transition of the boundary layer to the turbulent state was described in Section 2.6. An example of the development of the boundary-layer parameters of NACA 0012 at zero angle of attack is shown in Figs. 4.10, 4.11, and 4.12.

In Fig. 4.10, the distribution of the shape factor along the NACA 0012 airfoil (at zero angle of attack) is shown. With the reference to Section 4.1.1, it can be seen that for all Reynolds numbers displayed, the laminar separation

⁴A streamlined body is assumed because, in the aeroacoustics of a bluff body, the boundary-layer noise is negligible in comparison to the noise caused by the wake.

bubble is present (i.e., $H > 4$). The Reynolds number 5 000 is very low, and corresponds approximately to the freestream velocity $0.7 \text{ m} \cdot \text{s}^{-1}$ for an airfoil of 0.1 m chord length under standard atmospheric conditions.

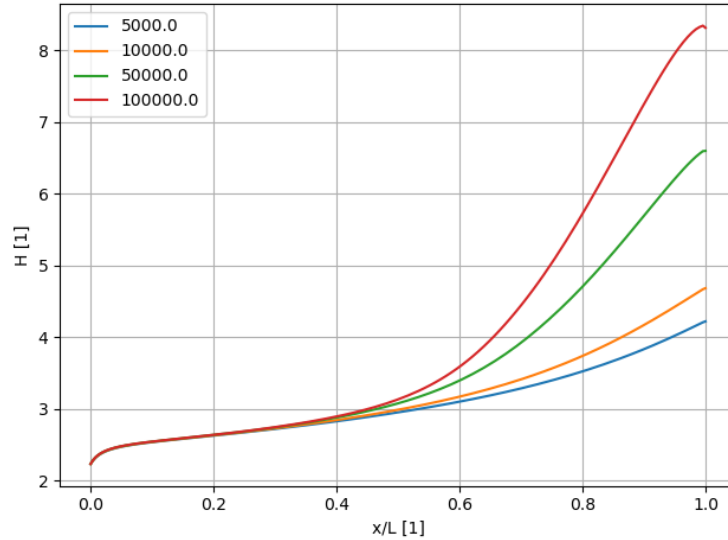


Figure 4.10: Shape factor along NACA 0012 for four different Reynolds numbers (5 000, 10 000, 50 000, and 100 000) based on the chord length L . Obtained using *XFOIL*.

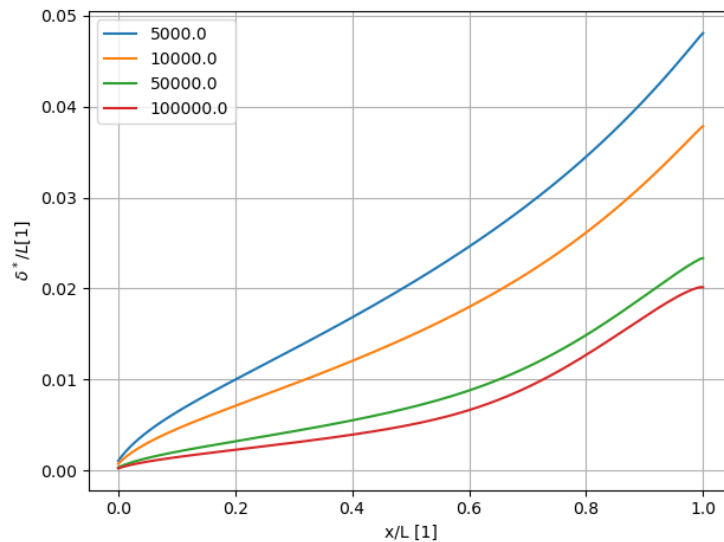


Figure 4.11: Displacement thickness along NACA 0012 for four different Reynolds numbers (5 000, 10 000, 50 000 and 100 000). Obtained using *XFOIL*.

The other input parameter needed for the aeroacoustic analysis of the boundary layer is the distribution of displacement thickness along an airfoil. An example of such a distribution for the NACA 0012 airfoil is shown in

Fig. 4.11.

The last important parameter, according to the discussion in Section 4.2, is the distribution of the velocity outside the boundary layer $U_e(x)$. For the range of low Reynolds numbers used in the previous examples, this distribution does not change significantly with Reynolds number; therefore, in Fig. 4.12, a distribution of the velocity along the airfoil is shown only for one Reynolds number.

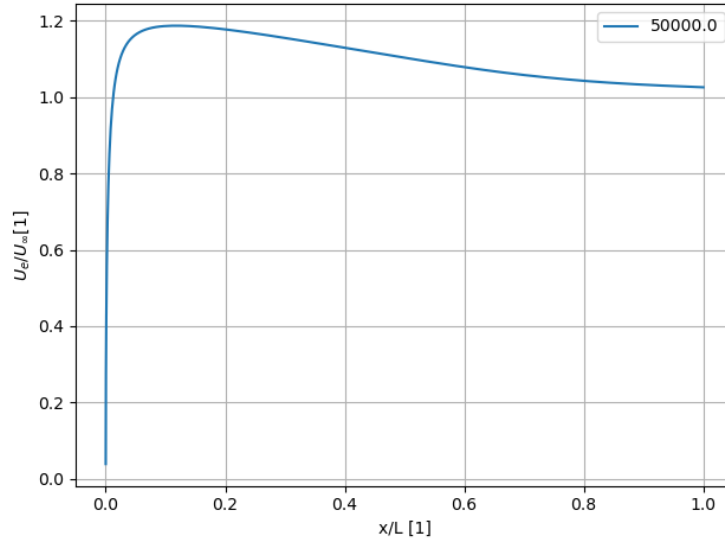


Figure 4.12: Velocity outside the boundary layer along NACA 0012 for a Reynolds number of 50 000. *Obtained using XFOIL.*

Using XFOIL to obtain the input parameter for the method described in Section 4.1 is not only viable, but convenient and reliable [92]. The other approach is to obtain these data using different boundary layer solvers or experimental measurements. This is also the case for the Falkner–Skan velocity profiles. While it is convenient to use them, the following procedures and derivations are independent of the source of the boundary-layer parameters and velocity profiles.

4.3.2 Linear Perturbation

It is assumed that the disturbance moves slowly along the parallel axis, so that some derivatives can be neglected. The perturbation stream function (Eq. (2.36)) can be modified for a non-constant wave number:

$$\Psi(x, y, t) = \Phi \cdot e^{i\left(\int_{x_0}^x k \cdot dx - \omega t\right)} \quad (4.29)$$

where Φ is the local amplitude function, k is the complex wave number, and ω is the angular velocity, which is related to the frequency f by

$$\omega = 2 \cdot \pi \cdot f \quad (4.30)$$

4.3.3 Growth Rate

Jaffe et al. [93] proposed an amplification factor for the fixed frequency disturbance as a means to predict the transition to the turbulent state. This is commonly known as the e^N method. In this approach, when the growth rate reaches some defined value (i.e., $e^{N_{\text{crit}}}$), the boundary layer's state is no longer considered to be laminar.

The amplification factor for a constant ω is given by the following equation (which involves the real part of the exponential function in Eq. (4.29)):

$$\mathcal{A} = \exp\left(-\int_a^b k_i(x) dx\right) \quad (4.31)$$

where $k_i(x)$ is the imaginary part of the local wave number, obtained using the method described in Section 4.2.3. In a similar manner, Schubauer [94] defined an amplification rate for a fixed (real) wave number (i.e., for the temporal growth rate).

4.3.4 Transition in a Laminar Separation Bubble

As discussed in the previous chapters, the boundary-layer transition can occur in a laminar separation bubble. This means that the Falkner–Skan velocity profiles can no longer be used, and neither can the linear instability solution. Predicting the behavior of the initially linear disturbance after passing to the turbulent part of the boundary layer could be the subject of a future study.

Kingan and Pearse [53] proposed using XFOIL and Falkner–Skan velocity profiles to predict the peak frequency based on the maximum growth rate \mathcal{A} at the trailing edge, and other tonal frequencies based on acoustic feedback model of Tollmien-Schlichting waves. They presented four case studies of NACA airfoils; however, these case studies have relatively high velocities (over 20 m/s, while the chord length is around 0.1 m) and it is unclear if there was a transition to a turbulent boundary layer or whether their measurement stayed in the region of linear instabilities. There is no further description of how the potential occurrence of a turbulent boundary layer was handled in their work.

4.4 Noise Source in a Laminar Boundary Layer

The noise source in the boundary layer itself can be described using Eq. (3.9). This can be written in terms of velocities u and v , and spatial coordinates x and y , as

$$Q(x, y, t) = 2\rho_\infty \frac{\partial U}{\partial y} \frac{\partial v'}{\partial x} + \rho_\infty \left(\frac{\partial u'}{\partial x}\right)^2 + 2 \cdot \rho_\infty \frac{\partial u'}{\partial y} \frac{\partial v'}{\partial x} + \rho_\infty \left(\frac{\partial v'}{\partial y}\right)^2 \quad (4.32)$$

Jordinson [89] evaluated the Reynolds stress in terms of amplitude functions of the perturbation stream function. The value of the acoustic source term

Q can be evaluated in a similar manner. According to Schlichting and Gersten [21, p. 428], only the real part Ψ_r of the perturbation stream function $\Psi(x, y) = \Psi_r(x, y) + i \cdot \Psi_i(x, y)$ has a physical meaning. Substituting the perturbation velocities u' and v' as functions of the perturbation stream function, Eq. (2.37), into Eq. (4.32) leads to the following equation:

$$Q(x, y, t) = -2\rho_\infty \frac{\partial U}{\partial y} \frac{\partial^2 \Psi_r}{\partial x^2} + 2\rho_\infty \left[\left(\frac{\partial^2 \Psi_r}{\partial x \partial y} \right)^2 - \frac{\partial^2 \Psi_r}{\partial x^2} \frac{\partial^2 \Psi_r}{\partial y^2} \right] \quad (4.33)$$

The complex amplitude function is $\Phi(x, y) = \Phi_r(x, y) + i \cdot \Phi_i(x, y)$. For the spatial stability problem, the components of the complex wave number are $k(x) = k_r(x) + i \cdot k_i(x)$.

This first major simplification relies on the assumption that the changes in the amplitude function $\Phi(x, y)$ and wave number $k(x)$ with the coordinate x are negligible, and therefore their partial derivatives with respect to x are zero. Then, the second derivatives of the stream function are as follows:

$$\begin{aligned} \frac{\partial^2 \Psi_r}{\partial x \partial y} = \mathcal{A} \cdot & \left[\left(-k_r \cdot \frac{\partial \Phi_i}{\partial y} - k_i \cdot \frac{\partial \Phi_r}{\partial y} \right) \cos(\omega t - \varphi(x)) \right] + \\ & \mathcal{A} \cdot \left[\left(k_r \cdot \frac{\partial \Phi_r}{\partial y} - k_i \cdot \frac{\partial \Phi_i}{\partial y} \right) \sin(\omega t - \varphi(x)) \right] \end{aligned} \quad (4.34a)$$

$$\begin{aligned} \frac{\partial^2 \Psi_r}{\partial x^2} = \mathcal{A} \cdot & \left[\left(k_r^2 \Phi_r - k_i^2 \Phi_r - 2k_i k_r \Phi_i \right) \cos(\omega t - \varphi(x)) \right] + \\ & \mathcal{A} \cdot \left[\left(k_r^2 \Phi_i - k_i^2 \Phi_i + 2k_i k_r \Phi_r \right) \sin(\omega t - \varphi(x)) \right] \end{aligned} \quad (4.34b)$$

$$\begin{aligned} \frac{\partial^2 \Psi_r}{\partial y^2} = \mathcal{A} \cdot & \left[\left(\frac{\partial^2 \Phi_r}{\partial y^2} \right) \cos(\omega t - \varphi(x)) \right] + \\ & \mathcal{A} \cdot \left[\left(\frac{\partial^2 \Phi_i}{\partial y^2} \right) \sin(\omega t - \varphi(x)) \right] \end{aligned} \quad (4.34c)$$

Here, two substitutions have been made for the phase change $\varphi(x)$ of the perturbation wave and the amplification factor \mathcal{A} :

$$\varphi(x) = \int_{x_0}^x k_r(x) dx \quad (4.35)$$

$$\mathcal{A}(x) = e^{-\int_{x_0}^x k_i(x) dx} \quad (4.36)$$

where x_0 is the position of the first instability (i.e., the first occurrence of $c_i > 0$ from the leading edge). The disturbance travels with velocity c_r , which is always greater than zero. This means the points of decay are only important downstream from the initial disturbance. (If there is a region after the initial disturbance in which $c_i < 0$, it can eventually lead to mitigation of the original disturbance.)

The boundary layer is under steady boundary conditions and the spatial stability analysis is established for a given frequency $2\pi\omega$. The root-mean-square value of the expressions (4.34) for one corresponding period can be found:

$$\left(\frac{\partial^2\Psi_r}{\partial x\partial y}\right)_{\text{RMS}} = \frac{1}{\sqrt{2}} \cdot \mathcal{A} \cdot \left|\frac{\partial\Phi}{\partial y}\right| \cdot |k| \quad (4.37a)$$

$$\left(\frac{\partial^2\Psi_r}{\partial x^2}\right)_{\text{RMS}} = \frac{1}{\sqrt{2}} \cdot \mathcal{A} \cdot |\Phi| \cdot |k| \quad (4.37b)$$

$$\left(\frac{\partial^2\Psi_r}{\partial y^2}\right)_{\text{RMS}} = \frac{1}{\sqrt{2}} \cdot \mathcal{A} \cdot \left|\frac{\partial^2\Phi}{\partial y^2}\right| \quad (4.37c)$$

Equations (4.37) differ from each other by the derivative of the absolute value of the amplitude function. Using this RMS analysis to obtain some insight into the terms in the source equation (4.33) leads to the following proportionality assumptions:

$$\frac{\partial^2\Psi_r}{\partial x\partial y} \propto \mathcal{A} \cdot \left|\frac{\partial\Phi}{\partial y}\right| \cdot |k| \quad (4.38a)$$

$$\frac{\partial^2\Psi_r}{\partial x^2} \propto \mathcal{A} \cdot |\Phi| \cdot |k| \quad (4.38b)$$

$$\frac{\partial^2\Psi_r}{\partial y^2} \propto \mathcal{A} \cdot \left|\frac{\partial^2\Phi}{\partial y^2}\right| \quad (4.38c)$$

The complex amplitude function is normalized by its maximum absolute value $|\Phi|$, and the absolute values of the first and the second derivatives of the amplitude function are considered to be of similar magnitude to $|\Phi|$. The amplification factor \mathcal{A} depends on its exponent, which is negative for $k_i > 0$ (i.e., a stable mode) and positive for $k_i < 0$ (i.e., an unstable mode). This is significant because $\mathcal{A} < 1$ for stable modes and $\mathcal{A} > 1$ for unstable modes. The first term of Eq. (4.33) depends on the first power of \mathcal{A} , so it is the dominant term of the equation for the stable region, whereas the second and third terms are the dominant terms for the unstable modes. The first term is in fact the linear instability version of the mean shear–turbulence interaction term of Eq. (3.9), so it is more appropriate to call it the *mean shear–linear instability interaction term*.

To obtain a time-dependent value of the simplified source term $Q(x, y, t)$, the equations (4.34) can be substituted into Eq. (4.33). The time-dependent source term can be used to obtain information on the acoustic pressure in the far field (for example, using the nonfield method of Kulish et al. [A2]). However, such a solution also requires taking into account sound reflection on the surface and scattering at the trailing edge, which would require further computational models to be established. To evaluate the frequency footprint, it could be helpful to obtain a comparable value for the source.

The root-mean-square value of $Q(x, y, t)$ for one period corresponding to a given frequency can be found:

$$Q(x, y)_{\text{RMS}} = \sqrt{\frac{\omega}{2\pi} \int_0^{\frac{2\pi}{\omega}} (Q(x, y, t))^2 dt} \quad (4.39)$$

By substituting the derivatives of the stream function into Eq. (4.39), a full expression of the point source strength is obtained. There is no analytical solution for this integral in the general form, so the solution must be obtained numerically for each point in the discretized boundary layer. However, this is a key result of this thesis: it expresses the linear instability noise of the boundary layer in the form of a *point acoustic source* in the boundary layer.

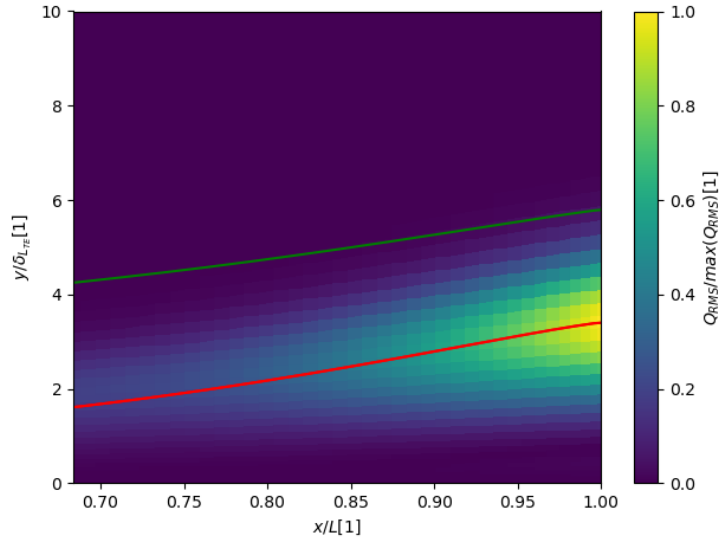


Figure 4.13: Field of acoustic sources in the boundary layer $Q(x, y)_{\text{RMS}}$ of NACA 0012 with 6.62 m/s freestream velocity and perturbation frequency 293 Hz. The red curve is the local boundary-layer displacement thickness ($\delta^*/\delta_{L_{\text{TE}}}$) and the green curve is the local conventional boundary-layer thickness ($\delta/\delta_{L_{\text{TE}}}$). The displacement and conventional thicknesses are both normalized to the boundary-layer length scale at the trailing edge ($\delta_{L_{\text{TE}}}$).

In Fig. 4.13, results are presented for the solution of the acoustic source field defined by Eq. (4.39) under one of the specified boundary conditions. The boundary-layer length scale at the trailing edge (as defined by Eq. (4.3)) is used as the length scale for this figure. The results show, as expected, that the most important acoustic source is near the trailing edge. The displacement (red curve) and conventional (green curve) boundary-layer thicknesses are also shown. The displacement thickness is very similar to the position of the maximum value of the acoustic source (Q_{RMS}) for each span station, while the conventional thickness behaves as an envelope curve for the location of the significant part of the acoustic source field. This could explain the finding of Brooks et al. [41] that using the conventional thickness for the

Strouhal frequency scaling produces better results than with the displacement thickness.

For comparison of the different boundary-layer states (e.g., solutions of the Orr–Sommerfeld equation for different frequencies), the following approach is established. The influence of acoustic sources on each other is neglected. However, the RMS value of the source strength cannot be summarized over the entire boundary layer, because with the x -coordinate there is also a phase shift (based on Eq. (4.35)). A comparison method could be established using some artificial variable that summarizes the RMS value only over the y -coordinate (i.e., the thickness of the boundary layer). This would provide some insight into the strength of the ideal acoustic source, though without direct physical meaning.

4.4.1 Tonal Noise Frequency Model

To find the peak frequency of boundary-layer instability noise, it is necessary to evaluate Eq. (4.39) for a range of frequencies. This requires evaluating the spatial instability Orr–Sommerfeld problem to obtain the wave number k , the amplitude of the growth of the instability \mathcal{A} , and the amplitude function Φ for the number of span stations along the surface and the discretized boundary layer.

Proposed Frequency Model of Laminar Boundary-Layer Noise

For the given boundary-layer conditions and constant frequency, the maximum value of the acoustic source term in the boundary layer can be found:

$$\max_x \left(\sum_y Q(x, y)_{\text{RMS}} \Delta y \right)_{\omega} = \mathcal{F}(\omega) \quad (4.40)$$

The peak frequency of the boundary layer instability is the frequency for which the expression in (4.40) is maximized.

This model is derived without any assumptions regarding refraction, reflection, or scattering of the sound wave due to the presence of the solid boundary. Hence, the magnitudes of the RMS values from the source-term model are not directly comparable to the measured spectrum. It is also important to note that the function \mathcal{F} has no physical meaning and is only used to predict the frequency with the strongest source terms.

Fig. 4.14 compares the method of maximal amplification of Tollmien–Schlichting waves at the trailing edge (i.e., the maximum of $\mathcal{A}(x_{\text{TE}})$) and the proposed method (Eq. (4.40)) based on the acoustic sources. The proposed method predicts a higher dominant frequency.

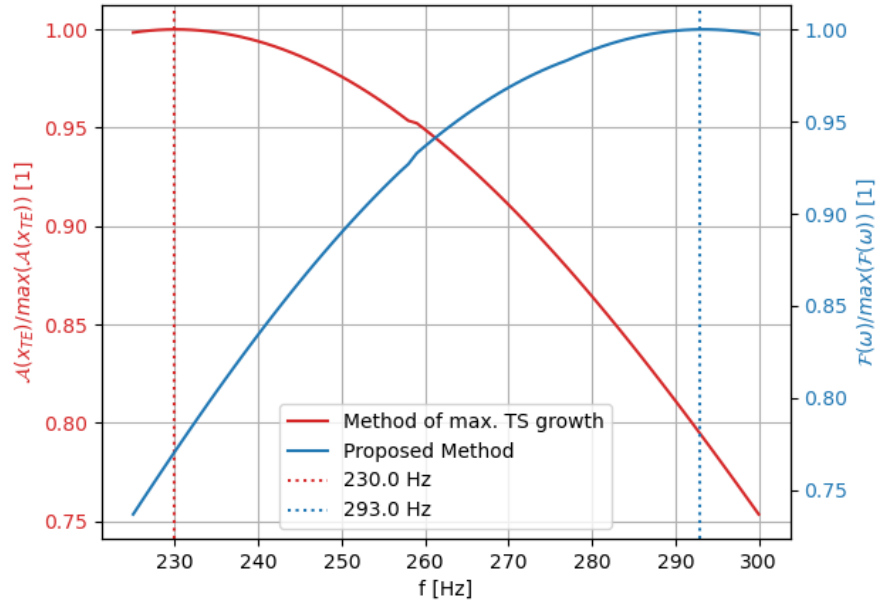


Figure 4.14: Comparison of the proposed tonal model with the model of the maximal growth of Tollmien–Schlichting waves for velocity 6.62 m/s (Reynolds number $Re_L = 44143$).

It is also important to note that the model of point sources cannot be used directly to evaluate the acoustic pressure in the far field (i.e., the sound pressure level), to determine whether the emitted noise is audible. This is due to one of the properties of the *homogeneous* Orr–Sommerfeld equation (described in Section 4.2.3), that any multiple of a non-trivial solution is also a solution. This leads to the problem of the magnitude of the initial disturbance, i.e., the magnitude of the emitted sound depends on the magnitude of the velocity perturbation. Therefore, it is suitable to use this method for the frequency comparison; however, it cannot be used to evaluate the acoustic pressure in the far field and determine whether the sound is audible.

In Section 3.2.1, the acoustic feedback caused by a sound source near the trailing edge was described. According to that literature survey, the acoustic feedback drives the generation of multiple discrete tones connected to the main tone.

■ 4.4.2 Conclusion

The source model for the noise in the boundary layer based on the perturbation stream function are proposed in Eq. (4.39). This equation only describes the source of noise, without any acoustic effects caused by the presence of the solid wall. This means that there is no verification that the sound source is audible and is present in the acoustic far-field noise spectrum. This acoustic source model is used to predict the dominant acoustic frequency of the boundary layer caused by linear instabilities. Although the aerodynamically generated

noise could be connected to the Tollmien–Schlichting waves, this does not necessarily mean that the frequency of the dominant sound source is the same as the frequency of the most amplified Tollmien–Schlichting waves. As Eq. (4.39) shows, the noise source depends not only on the amplification factor of the Tollmien–Schlichting waves, but also on their wave number and the magnitude of the perturbation. In the proposed model, the magnitude of the perturbation is normalized to its maximum absolute value (the motivation for this normalization was explained in Section 4.2.3). This magnitude of perturbation is influenced by the outer flow (i.e., by the turbulence intensity of the freestream) and cannot be expressed directly.

This model of the acoustic sources incorporates only the acoustic source above the surface. An acoustic source behind the trailing edge can be more powerful than those in the proposed boundary-layer model. An acoustic source in the wake is expected to be connected with acoustic sources in the boundary layer by frequency; i.e. the sources in the boundary layer are the origin of the acoustic source in the wake (for the laminar boundary-layer instability noise). This assumption makes the proposed model consistent with the findings of Desquesnes et al. [52], or with the trailing-edge treatment in the experimental measurement of Chong et al. [56]. This is also another reason why the exact value of the magnitude of the acoustic sources in the boundary layer is not the primary focus of the proposed model. This theory can also offer an extension of the proposed model to incorporate the other side of the airfoil. In that case, the acoustic source in the wake should be influenced by the acoustic sources from both the pressure and suction sides of the airfoil.

A further validation of the proposed method is presented in Chapter 6, where it is compared with the method of maximal amplification of Tollmien–Schlichting waves, the empirical model of Brooks, Pope, and Marcolini, and experimental data obtained using the method described in the following Chapter 5.

4.5 Acoustic Feedback

As an acoustic feedback model, the equation proposed by Arcondoulis et al. [61] is used,

$$f_n(Re, \alpha) = \frac{c_r(Re, \alpha)}{L_F(Re, \alpha)} \left(n + \frac{1}{2} \right) \left(1 + \frac{c_r(Re, \alpha)}{c_\infty - U_\infty} \right)^{-1} \quad (4.41)$$

The convective velocity c_r can be obtained from the solution of the stability problem as the real part of the complex phase velocity corresponding to the main frequency. The convective velocity depends not only on the Reynolds number and the angle of attack, but also on the frequency.

The freestream velocity U_∞ is known, as is the speed of sound c_∞ . However, the feedback length L_F is subject to further discussion. Arbey and Bataille [47] assumed it to be the distance between the maximum velocity point and the trailing edge. Arcondoulis et al. [61] theorized that this length should be the

distance between the laminar boundary-layer separation point and the noise source behind the trailing edge. They proposed an empirical method to predict *ladder* frequencies based on guessing n as an integer with feedback-length constraints below the length of the chord.

The empirical method can also be based on the frequency difference because, based on the Tam feedback model (which is the foundation for the other feedback models), the difference between frequencies is the same for a given velocity. This frequency difference can be described using Eq. (4.41) and the definition of $\Delta f = f_{n+1} - f_n$:

$$\Delta f = \frac{c_r}{L_F} \left(1 + \frac{c_r(Re, \alpha)}{c_\infty - U} \right)^{-1} \quad (4.42)$$

However, the feedback length is still not well defined. Equation (4.42) is used in Section 6.2 in an inverted way to obtain the feedback length based on the measured frequency difference.

Chapter 5

Experiment

The experimental validation of the theoretical findings of the aeroacoustic (frequency) signature of the boundary layer is carried out on the well-known NACA 0012 airfoil. This choice of airfoil is based on the possibility of validating the simulated solution and eventually extending the set of measured data for future use.

Aeroacoustic measurements are usually conducted in a special wind tunnel, which is designed to produce low background noise and to be anechoic [12]. However, for the required wind speed (up to 15 m/s, which is based on the Reynolds number for chord length 0.1 m), such a facility is not available in the Department of Fluid Dynamics and Thermodynamics at FME CTU in Prague, so a *substitute measurement method* is proposed in this chapter.

The main goal is to obtain the frequency footprint of one NACA 0012 airfoil for different freestream speeds. These measurements should be sufficient to obtain a comparison with simulated data and with the empirical model of Brooks, Pope, and Marcolini [41]. The chord length of the designed test model is 100 mm and the span is 390 mm. The airfoil has end plates to minimize the velocity in the third direction.

5.1 Wind Tunnel

Measurements are conducted in the low-speed wind tunnel at the Department of Fluid Dynamics and Thermodynamics at FME CTU in Prague. This wind tunnel was built in 2015 and has no special modification for acoustic measurement. An analysis of the possibility of some limited acoustic measurement was published in 2019 by Suchý [A3]. This analysis shows higher low-frequency background noise in the wind tunnel with an empty test section; however, by using the method of spectral subtraction, it should be possible to obtain reliable frequency values and estimates of the corresponding magnitudes [95]. Another problem is the presence of background noise at 4 kHz and its harmonic frequencies, probably caused by the fluctuating core of the electric engine that drives the wind tunnel (the frequency of 4 kHz is the switching frequency of the variable-frequency drive) [A3]. These factors must be taken into consideration during the design of the experiment and in processing and evaluating the results.

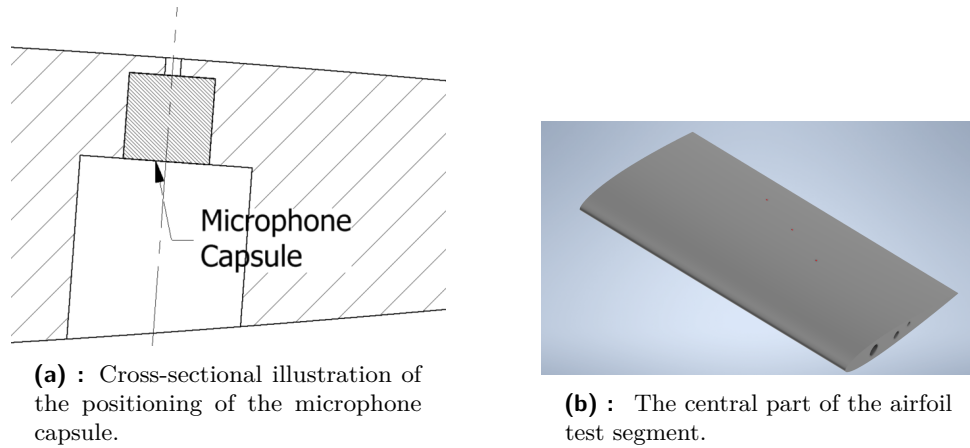
5.2 Measurement Methods

The main requirements for the desired measurement are to capture very small, weak, and rapid changes in either the velocity or the pressure flow field. Methods based on hot-wire anemometry can provide sufficiently fast responses and sensitivity to small changes in the velocity field. However, placing a hot-wire anemometry probe (or any probe) inside the flow field near the trailing edge causes a break-down of the tonal noise emitted by the airfoil. This leads to the conclusion that a non-intrusive method must be used, because the effects of intrusive methods on acoustic emission are not fully understood.

The second method considered is the measurement of static pressure fluctuations on the airfoil surface. Using a small electret microphone, preliminary tests were conducted that showed promising results; therefore, further measurements were conducted using this approach.

5.3 Measurement Setup

The measurement of static pressure fluctuations was performed using electret microphones. Due to the background noise in the wind tunnel, a modified measurement approach was established based on measuring the acoustic pressure on the airfoil surface, similar to pinhole measurement of the fluctuating turbulence pressure [12]. A small electret microphone is placed directly below the surface of the airfoil, which has a hole matching the diameter of the hole in the microphone capsule. This microphone setup is shown in Fig. 5.1a. The pinhole diameter is 0.9 mm, which should yield a lower frequency resolution for low-wavelength waves, so the microphone should primarily capture the acoustic noise. It is assumed that the wavelength of the sound is much longer than the scale of the originating structures. This assumption is based on the structure's convective velocity, which is assumed to be around half the freestream velocity. So, for freestream velocities up to $15 \text{ m} \cdot \text{s}^{-1}$, the convective velocity is approximately 100 times slower than the speed of sound. If the frequency of the flow structure is the same as the frequency of the sound, the sound wavelength should be 100 times higher than the scale of the flow structure. For the purpose of this measurement, it is desirable to obtain acoustic waves, rather than fluctuating static pressure in the boundary layer. In the proposed measurement method, three microphones are placed in the surface of an airfoil test segment; see Fig. 5.1b. These microphones are placed in the top surface of the airfoil at 55 %, 68 %, and 80 % of the chord length from the leading edge.



(a) : Cross-sectional illustration of the positioning of the microphone capsule.

(b) : The central part of the airfoil test segment.

Figure 5.1: Positioning of the microphones inside the airfoil.

To verify that the captured frequency spectrum is of acoustic origin, two reference microphones are placed outside the airflow. (They are also important for the evaluation of the potential effects of the airflow on the microphone itself.) The positioning of the microphones is also important because, in some locations, a dominant frequency could be distorted by the effects created on the other side of an airfoil. This is similar, for example, to vortex shedding behind a cylinder, for which there is a dominant frequency twice as high in the centerline downstream than elsewhere [A4].

■ List of Main Components

The main data acquisition (DAQ) unit is NI cDAQ-9174, which provides slots for 4 NI DAQ modules. The raw electrical signal acquired is the voltage (from microphone probes), so the first two modules are chosen to capture the voltage with a high sampling rate per channel. The third slot is used for a module dedicated to recording the current electrical signal from the pressure transducer of a Pitot-static tube (also known as a Prandtl probe). The Pitot-static tube is used to calibrate the airspeed in the wind tunnel.

An overview of the modules used in the NI cDAQ-9174 chassis is as follows:

- NI 9250: 2-channel, 102.4 kS/s/ch, ± 5 V
- NI 9230: 3-channel, 12.8 kS/s/ch, ± 30 V
- NI 9203: 200 kS/s, ± 20 mA

The setup consists of 5 microphones. Three electret microphones are built inside the airfoil surface, and two are placed outside the air stream as reference microphones. In the remainder of this thesis, the microphones are referred to as follows:

- **Mic A:** Microphone in the airfoil surface at 55 % of the chord length
- **Mic B:** Microphone in the airfoil surface at 68 % of the chord length

- **Mic C:** Microphone in the airfoil surface at 80 % of the chord length
- **Ref A:** Free-field microphone above the leading edge outside the airflow
- **Ref B:** Free-field microphone outside the airflow

■ 5.3.1 Free-Field Microphones Setup

For the reference sound measurement outside the airflow, the Microtech Gefell M370 was chosen. This is a free-field omnidirectional constant-current power electret microphone. The nominal sensitivity of this microphone model is 12.5 mV/Pa. The microphone with its casing is shown in Fig. 5.2.



Figure 5.2: Free-field Microtech Gefell M370 microphone.

Both NI modules, NI 9250 and NI 9230, can power this type of microphone, and therefore it is possible to connect this microphone directly to the data acquisition module. Field microphone sensitivity calibration was performed using the Microtech Gefell Kalibrator 4011, which conforms to IEC 60942 Class 1, and the CM-C200 SPL Meter Calibrator, which conforms to IEC 60942 Class 2.

■ 5.3.2 Airfoil Microphones Setup

Particular attention was given to the choice of microphones within the airfoil. One of the criteria was price, because it is assumed that the microphone is permanently mounted to the airfoil and cannot be removed without damaging the airfoil section or the microphone itself. The technical criteria were the dimensions, frequency response, and sensitivity. Based on all these criteria, the small electret microphone CMC-4015-25L100 was chosen; see Fig. 5.3. This microphone was first applied to measurements of surface pressure spectra by Suchý et al. [A5].



Figure 5.3: CMC-4015-25L100 microphone.

The manufacturer, CUI Devices, provides information [96] on the nominal sensitivity -25 dB with reference value 0 dB = 1 V/Pa and standard operating voltage 3 V, which can be easily converted to the units of mV/Pa by analogy to Eq. (2.46):

$$S \text{ [mV/Pa]} = 10^{\frac{S \text{ [dB]}}{20}} \quad (5.1)$$

Using this equation, the nominal sensitivity of this microphone is found to be 50.12 mV/Pa, which is relatively high for such a device. Using the microphone calibrator, it was found that the value from the datasheet is not correct. The correct sensitivity lies in the range of 32 mV/Pa to 35 mV/Pa, which is still high enough for use without a preamplifier between the microphone and the NI DAQ module.

The datasheet [96] also contains information on the microphone's RMS self-noise, which is 32 dBa, which can be converted to an acoustic pressure of 10^{-4} Pa. This value is low enough to be undetectable against the background noise. The maximum value is not given; however, it can be reasonably assumed that the maximum value is at least 114 dB (i.e., 10 Pa).

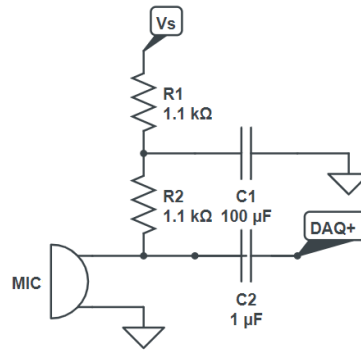


Figure 5.4: The electrical circuit used to power the electret microphones with a low-pass filtered power supply.

The chosen electret microphone requires a bias voltage. The basic electrical measurement circuit is provided by the manufacturer in the datasheet [96]; this is a standard circuit used to supply a bias voltage to electret microphones. The bias voltage should be as free from electrical noise as possible because any noise in the bias voltage would be measured in the output signal. A modified measurement circuit was designed; see Fig. 5.4. This extended circuit was originally designed for the measurement of the turbulence pressure spectra in [A5]. To reduce the noise in the supply voltage, a low-pass filter with a cutoff frequency of approximately 1 Hz was used ($R_1 = 1.1$ k Ω and $C_1 = 100$ μ F):

$$f_c = \frac{1}{2\pi R_1 C_1} = 1.45 \text{ Hz}$$

The capacitor $C_2 = 1$ μ F was chosen based on the original circuit in the datasheet [96]. This capacitor acts with the resistances R_1 and R_2 as a

high-pass filter with cutoff frequency

$$f_c = \frac{1}{2\pi(R_1 + R_2)C_2} = 72.34 \text{ Hz}$$

The high-pass filter does not cut off the frequency signal sharply below f_c ; rather, it gradually attenuates the frequency signal below the cutoff frequency. Therefore, the measurement should be reliable for frequencies above 72 Hz.

The measurement circuit was built four times on a stripboard for four measurement channels; see Fig. 5.5. Tantalum capacitors were used and the circuits were powered with a 3 V battery pack to avoid electrical noise from a switching power supply¹ or any other transformer connected to the laboratory electrical network.

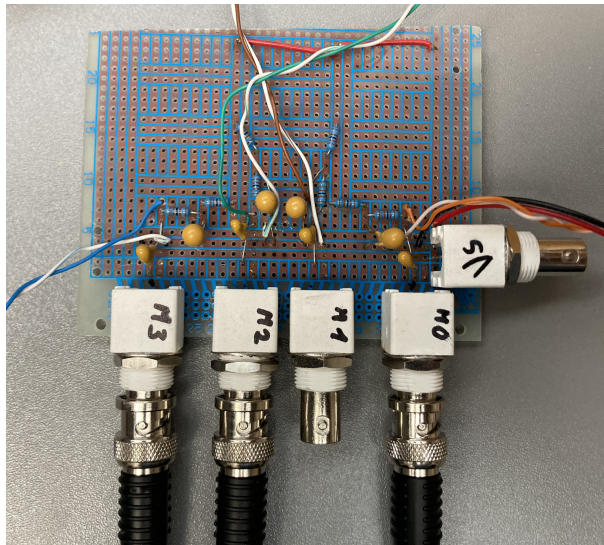


Figure 5.5: The stripboard with the electrical circuit for the electret microphones.

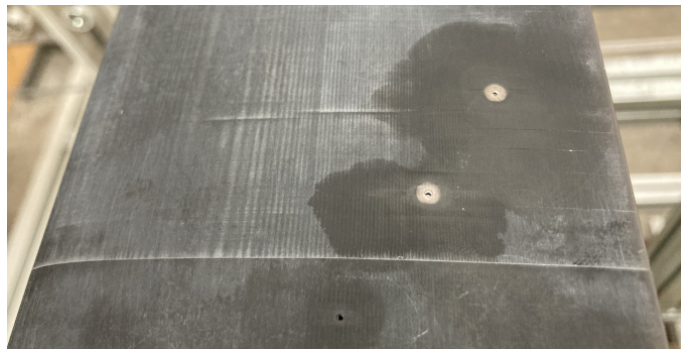


Figure 5.6: Electret microphones inside the test airfoil segment.

¹A switching power supply, which are now quite common, would be a poor choice. As the name suggests, the supply power is switching, so there would be some unwanted frequencies caused by the power supply.

The whole measurement chain was calibrated using the field microphone calibrator with RMS pressure fluctuations of 1 Pa and 10 Pa at 1 kHz. The microphones were built inside the tested airfoil segment; see Fig. 5.6. The surface of the tested segment seems to have some roughness in the figure; however, this is only a visual artifact, and the surface was smoothed out. The airfoil segment was printed using a Prusa SLA 3D Printer.

■ 5.3.3 Velocity Calibration

The used wind tunnel provides information on the airspeed inside the test section by measuring the change in static pressure at the contraction before the test section. The speed obtained from this measurement is not entirely accurate, so for each measurement point, additional velocity calibration was performed using the Pitot-static probe. The pressure difference of the Pitot-static probe (i.e., dynamic pressure) was measured using a 984Q.353D differential pressure transmitter from Beck Sensors. The obtained dynamic pressure was acquired using NI hardware and recorded for the airspeed evaluation. Since the Pitot-static probe was placed upstream of the leading edge of the tested airfoil section (see Fig. 5.7), the measured airspeed can be used as a reference value for the measured point.



Figure 5.7: The calibration of the airspeed with the Pitot-static probe.

5.4 Processing of Measured Data

The measured data are obtained in the form of time series. To find the frequency spectrum, Welch's [97] method is used. This method was chosen due to its ability to reject non-periodic arbitrary noise. A comprehensive study of this method is provided, for example, by Solomon [98]. Welch's method is based on splitting data into overlapping segments and calculating a modified periodogram for each, and then averaging these periodograms. In this thesis, this method is used only as a tool to obtain results in the frequency domain. The key parameters of this method are the length of each time segment, which affects the frequency resolution of the output spectrum, and the number of overlapping points between segments.

During the measurement campaign, the interim results showed that a 90-second data acquisition interval for each measured point was enough to obtain information about the frequency peaks. This preliminary study is shown in Fig. 5.8, where the amplitude–frequency spectra calculated for four different lengths of the input data from the same test case are presented. The sampling rate of this measurement is 102.4 kHz. A 1-second interval is not enough to obtain clear peaks from the recorded noise data. This same effect of averaging was observed by Solomon [98]. With a longer time interval, the averaging in Welch's method would produce less noisy results. This requires more resources, i.e., more disk space for the measured data and a longer run in the wind tunnel, and there would be no new information in the produced data. Therefore, longer measurements are not justified for determining the peak frequencies.

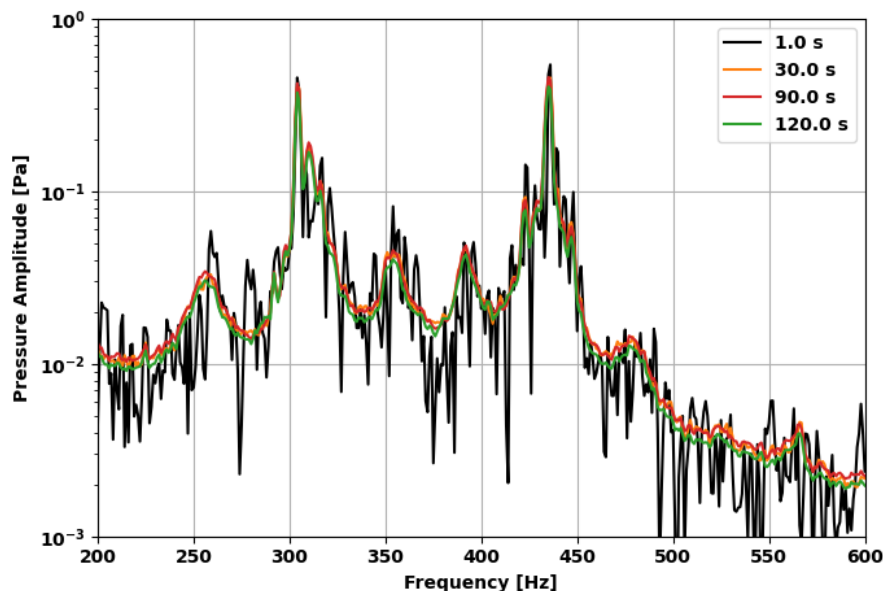


Figure 5.8: Study of the effect of time interval length for data recording.

The length of each segment in Welch's method is chosen based on the

sampling frequency to obtain a resolution of 1 Hz in the frequency domain.

■ 5.4.1 Selected Measured Spectra

The most important information obtained from the proposed measurement method is an amplitude spectrum under given measurement conditions. From the amplitude spectrum, it should be possible to evaluate the dominant frequency. There are three built-in microphones inside the tested segment. The results from these microphones can be compared not only to each other but also to the reference microphones outside the airflow.

The main measurement of the previously defined NACA 0012 segment at zero angle of attack was conducted at 59 velocity points between $2.74 \text{ m} \cdot \text{s}^{-1}$ and $30.89 \text{ m} \cdot \text{s}^{-1}$. For lower velocities below $7.59 \text{ m} \cdot \text{s}^{-1}$, only the dominant frequency peak is clear in the acoustic pressure fluctuation spectrum. For higher velocities, it is also possible to analyze the difference between the main frequency and the secondary tones, as described in Section 4.5.

For a detailed discussion of the main features of the obtained amplitude spectra, a few results are now selected. The first selected spectrum is shown in Fig. 5.9. There is a main frequency of 363 Hz, which is dominant in both the reference and airfoil microphones. There are also some secondary peaks in the signal from Mic A–C; however, there is no peak in Ref A. The tone of 266 Hz can be considered as the secondary peak.

In the second selected spectrum in Fig. 5.10 at freestream velocity $8.56 \text{ m} \cdot \text{s}^{-1}$, there is a primary peak at 289 Hz, and a secondary peak at 410 Hz. These peaks are of similar magnitude, which creates uncertainty about which of the tones is the dominant one. The peaks could also be contaminated by the background noise and echoes, so for a more precise examination, an aeroacoustic facility would be needed.

The spectrum in Fig. 5.11, with the primary dominant frequency at about 522 Hz, was selected for this discussion as it shows significant differences from the first two selected spectra. There is no sharp dominant frequency peak; rather, the peak is surrounded by several other peaks. It is also not possible to determine the secondary tonal peak.

In Fig. 5.12, there is a selected spectrum measured with a freestream velocity of $14.87 \text{ m} \cdot \text{s}^{-1}$. There is a primary peak frequency at about 686 Hz, and also a second dominant tone at 863 Hz, with pressure fluctuations of similar magnitude to the dominant frequency.

The last selected spectrum was chosen above the velocity, for which XFOIL predicted an occurrence of boundary-layer transition (see Section B.2). The amplitude spectrum of the pressure fluctuations is shown in Fig. 5.13. The peak frequency in this case is 1429 Hz; there is also a secondary tone with frequency 1263 Hz.

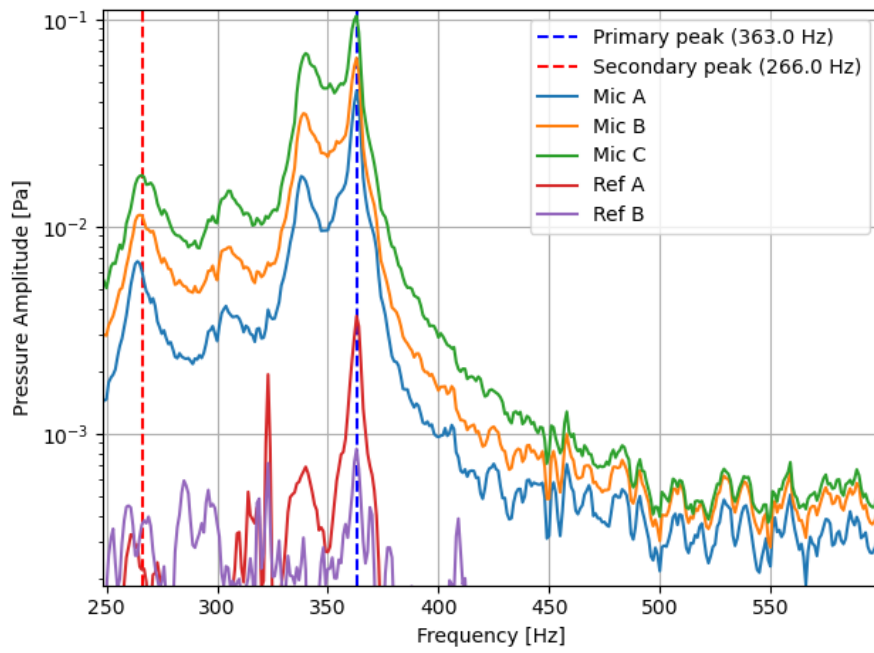


Figure 5.9: First selected spectrum at freestream velocity 7.59 m/s.

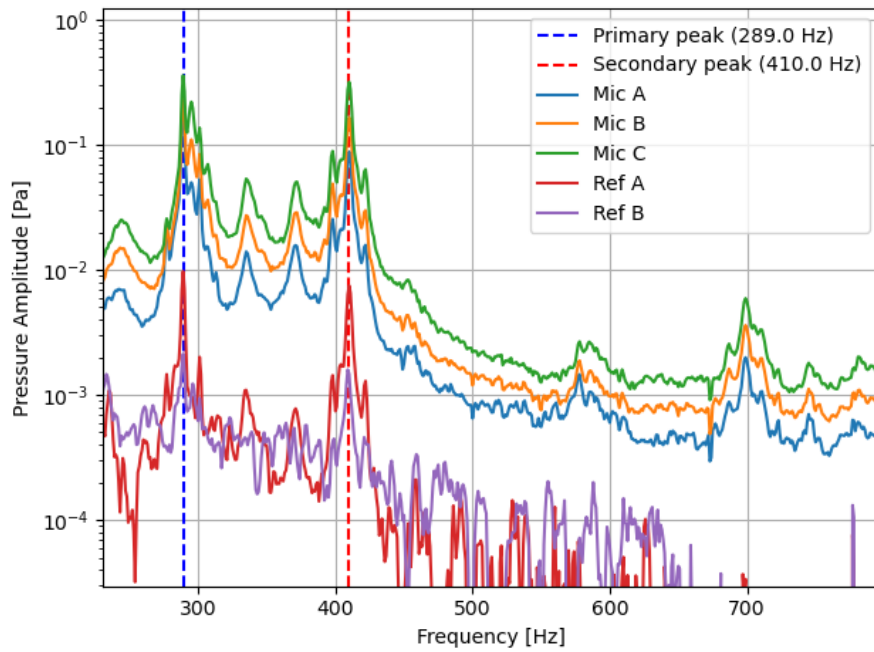


Figure 5.10: Second selected spectrum at freestream velocity 8.56 m/s.

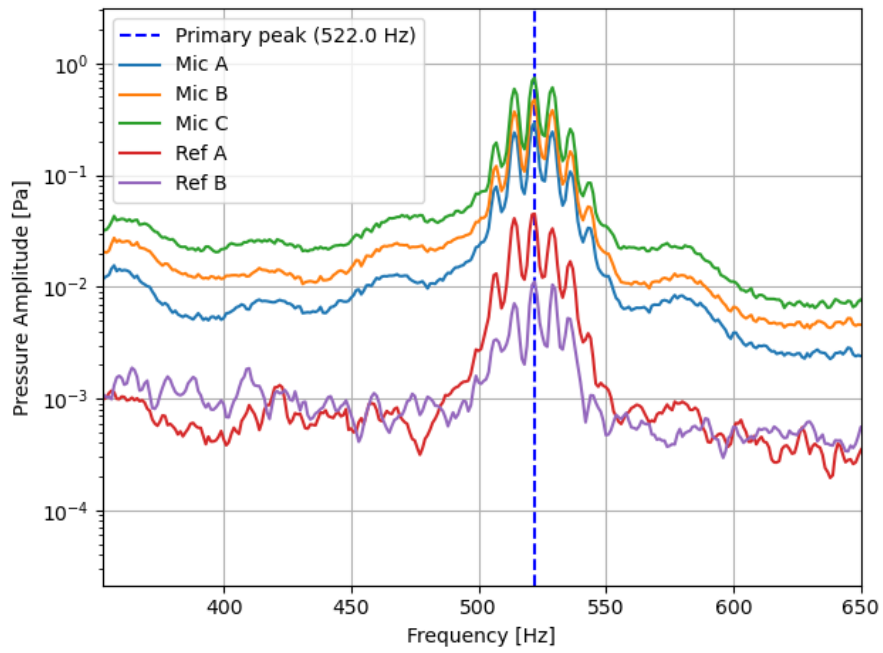


Figure 5.11: Third selected spectrum at freestream velocity 10.99 m/s.

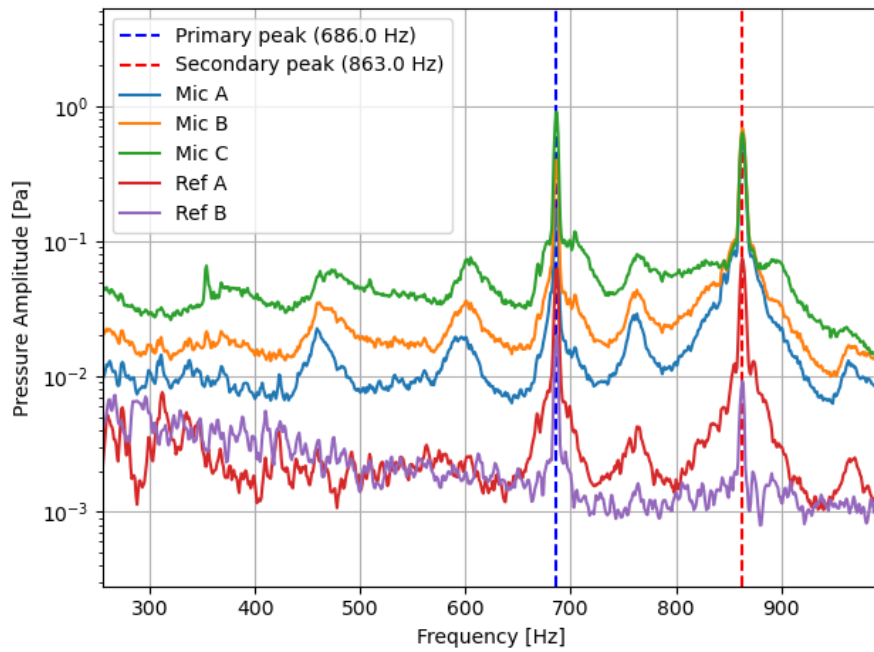


Figure 5.12: Fourth selected spectrum at freestream velocity 14.87 m/s.

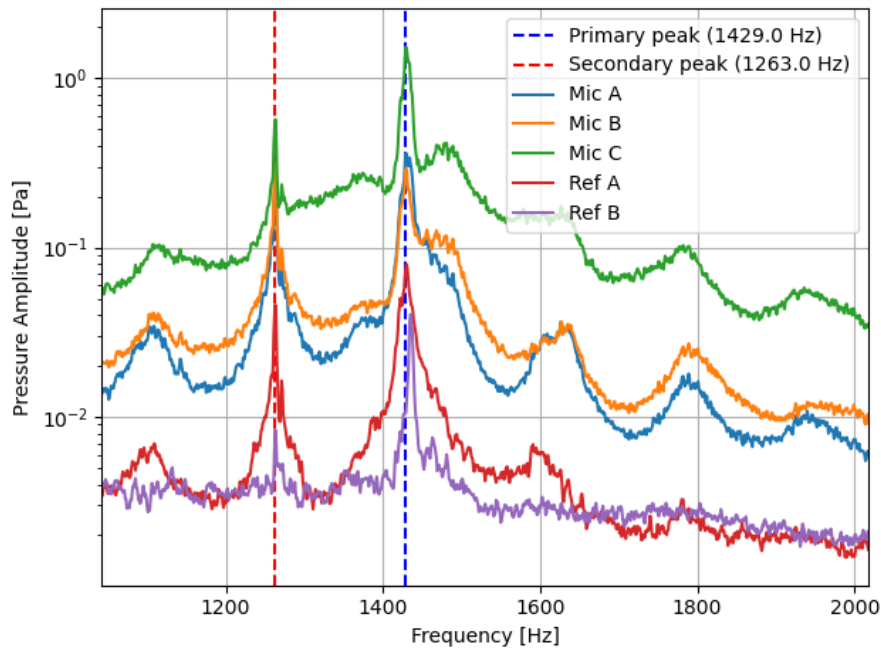


Figure 5.13: Fifth selected spectrum at freestream velocity 22.64 m/s.

5.5 Conclusion

The measurement method proposed and used in this thesis mainly provides information on the peak/main tones in the sound emitted by an airfoil placed in the wind tunnel test section. This method was designed to be a substitute method for the measurement method in a special aeroacoustic facility; therefore, very accurate results are not expected. However, the main results of this measurement method are information about the dominant frequency, not its magnitude (the magnitude is highly contaminated by the sound produced by the running wind tunnel), so these results can be compared with those obtained from the theoretical approach described in Chapter 4. This comparison will be presented in the following chapter.

The obtained spectra can also be used to determine the length scale of the acoustic feedback, which could be considered as a minor result of this thesis. The determination of the length scale will also be addressed in the following chapter, which presents and discusses the obtained results.

Chapter 6

Results and Discussion

This chapter presents the computational results based on the method described in Chapter 4 and the results of measurements based on the method described in Chapter 5. The first results presented are the peak/dominant frequencies with a comparison between the measurements, the theoretical calculations, and the results based on the empirical method of Brooks, Pope, and Marcolini [41].

6.1 Dominant Frequency of NACA 0012

Dominant frequencies of the laminar boundary-layer instability were obtained using a novel method of acoustic sources (Section 4.4.1), the method of maximum instability amplification factor [53], and experimental measurements (Chapter 5). These results are compared to the empirical model proposed by Brooks, Pope, and Marcolini (the BPM model).

6.1.1 BPM Empirical Model

The empirical model of peak frequency for the laminar vortex-shedding noise of NACA 0012 proposed by Brooks, Pope, and Marcolini [41] is as follows:

$$St = \frac{f \cdot \delta}{U_\infty} \quad (6.1a)$$

$$St = \begin{cases} 0.18 & (Re_L \leq 1.3 \cdot 10^5) \\ 0.001756 \cdot Re_L^{0.3931} & (1.3 \cdot 10^5 < Re_L \leq 4 \cdot 10^5) \\ 0.28 & (4 \cdot 10^5 < Re_L) \end{cases} \quad (6.1b)$$

This empirical model probably assumes that up to a Reynolds number of $1.3 \cdot 10^5$, the boundary layer is in a laminar state. This assumption is based on the expectation of frequency characteristics change when the boundary-layer transition occurs. It will be assumed that the prediction of the Strouhal number of 0.18 from the BPM method is valid only in the Reynolds number range for which there is *only* a laminar boundary-layer state present. The previously used XFOIL calculation of the boundary-layer parameters predicts the transition to a turbulent boundary layer in the laminar separation bubble at a Reynolds number based on the e^N criterion. It is possible to set this

criterion (to at least $N_{\text{crit}} = 11$) to obtain the laminar boundary-layer state up to a Reynolds number of $1.3 \cdot 10^5$. For the Reynolds number, the chord length is used as the characteristic length, while the conventional boundary-layer thickness (where 99% of the velocity is reached) is used for the Strouhal number. A short discussion on this length scale was presented in Section 4.4 and there is another short discussion in Section 6.1.3.

6.1.2 Tonal Frequency Comparison

Fig. 6.1 presents one of the major results of this thesis. Peak frequencies of the NACA 0012 laminar boundary-layer instability noise are plotted, obtained using four different methods (of which two are newly proposed in this thesis).

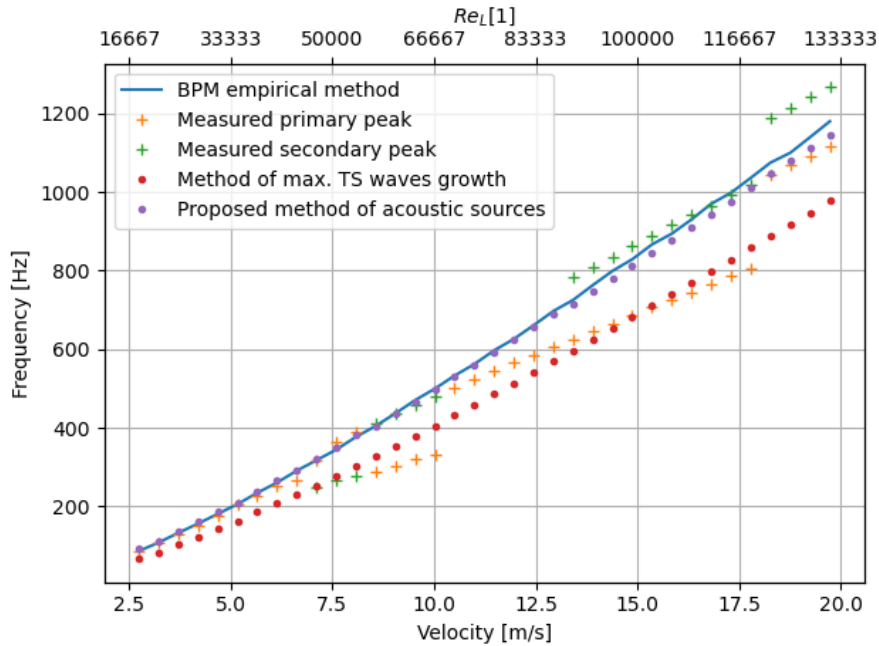


Figure 6.1: Measured, empirical, and simulation peak frequency for velocities below the predicted transition in the laminar separation bubble.

The results from the proposed method of acoustic sources match the frequencies based on the BPM empirical method better than the method of maximal amplification of Tollmien–Schlichting waves. The experimentally obtained tones are also plotted in Fig. 6.1. In the range of velocities from $8.56 \text{ m} \cdot \text{s}^{-1}$ to $10.02 \text{ m} \cdot \text{s}^{-1}$, there are secondary peaks at lower frequencies than the primary peaks. In the range from $10.50 \text{ m} \cdot \text{s}^{-1}$ to $12.93 \text{ m} \cdot \text{s}^{-1}$, it is not possible to clearly determine the secondary peaks. From the velocity of $13.42 \text{ m} \cdot \text{s}^{-1}$, secondary peaks can again be identified. Except for the range from $10.50 \text{ m} \cdot \text{s}^{-1}$ to $12.93 \text{ m} \cdot \text{s}^{-1}$, the measured tones (either the primary peak or the secondary peak) match the empirical model of BPM sufficiently (i.e., the difference is below 8%).

The frequency can be scaled to the non-dimensional Strouhal number, using the conventional boundary-layer thickness as the characteristic length. Scaled frequency peaks based on the calculated boundary-layer thickness are shown in Fig. 6.2. The proposed acoustic sources method again shows a smaller difference from the BPM model than the method of maximal amplification of Tollmien–Schlichting waves.

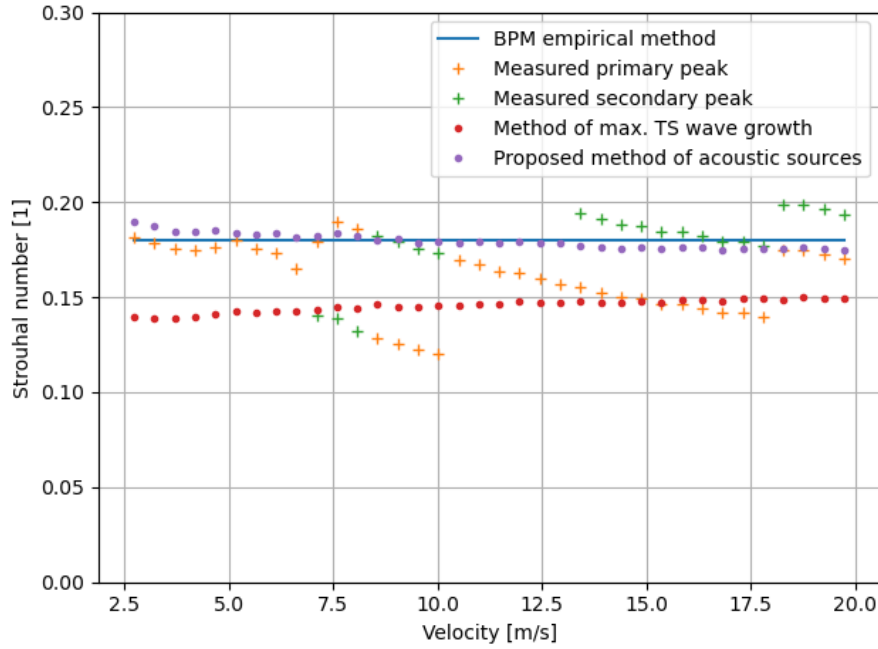


Figure 6.2: Measured, empirical, and simulation peak Strouhal number for velocities below the predicted transition in the laminar separation bubble. The characteristic length used to define the Strouhal number is based on the conventional boundary-layer thickness.

The experimentally obtained tones (primary and secondary) in Fig. 6.2 have a similar structure to the ladder structure described by Arbey and Bataille [47]. Either the primary or secondary peak frequency is, in most cases, close to the constant Strouhal number of 0.18 predicted by the empirical model.

Table 6.1: The mean value and standard deviation of the obtained results in the predicted laminar boundary-layer state.

Method	Mean Strouhal number	Std. deviation
Measurement (primary peak)	0.1662	0.0140
Max. TS wave growth	0.1456	0.0032
Acoustic sources	0.1798	0.0039

To further compare the approaches, mean values and corresponding standard deviations of the results obtained using each method are presented in

Table 6.1. This comparison shows that the Strouhal number predictions from the method developed in this thesis have the lowest relative standard deviation (2.17 %) in this velocity range.

In Figs. 6.1 and 6.2, the results are shown only for those conditions for which the XFOIL software does not predict a transition to a turbulent boundary layer based on $e^{N_{\text{crit}}}$ criteria with $N_{\text{crit}} = 11$.

The measurement was carried out for even higher velocities (up to $30.89 \text{ m} \cdot \text{s}^{-1}$). However, there is no method available to treat linear instabilities in the turbulent boundary layer (even when assuming that only the linear instabilities that originated in the laminar state are present), so there are no computational results for comparison. In addition, no computational method was used to predict the turbulent boundary-layer thickness; therefore, only the peak frequency as a function of velocity is presented. In Fig. 6.3, measured peak frequencies are shown for the entire velocity range investigated, and the results are fitted to the function $a \cdot U_{\infty}^b$; this function is based on the findings of Paterson et al. [44].

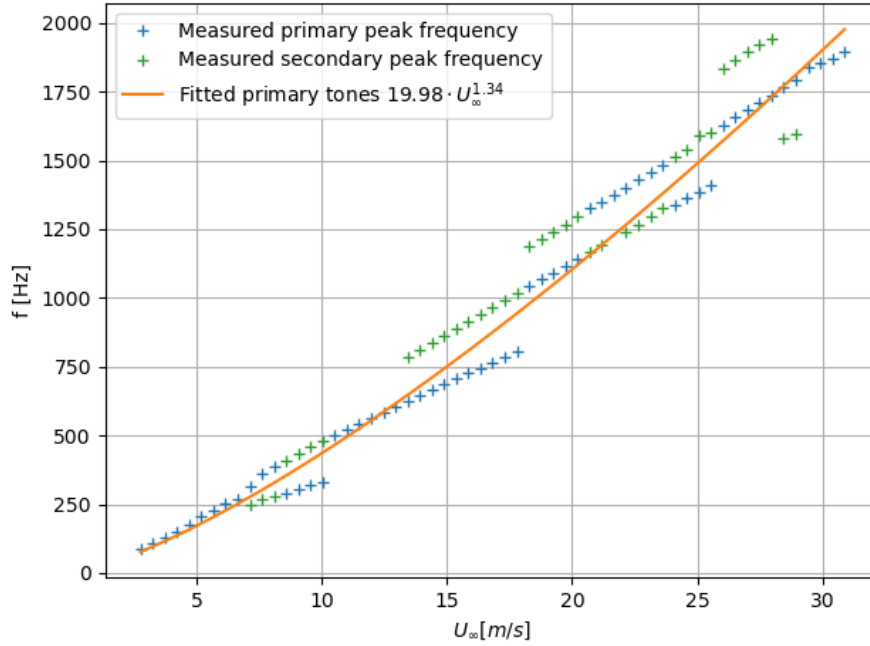


Figure 6.3: Primary and secondary tones in all measured points

In Fig. 6.3, some velocity ranges can be seen in which there is a swap between the primary (blue crosses) and secondary (green crosses) peaks (for example, for measured points between $24 \text{ m} \cdot \text{s}^{-1}$ and $26 \text{ m} \cdot \text{s}^{-1}$). The mechanism of the *dominant tone selection* could be explored in future work. Fig. 6.3 shows the ladder-type evolution of tonal peaks in the measured spectrum, similar to the findings of Arbey and Bataille [47].

6.1.3 Discussion on the Strouhal Number Length Scale

The non-dimensional similarity number used for the frequency scaling is the Strouhal number, which depends on the velocity, the frequency, and a characteristic length. As was mentioned in Section 4.4.1, the conventional boundary-layer thickness creates an envelope around the acoustic sources in the boundary layer, so this is a rather convenient length scale. However, the displacement thickness is often used as a length scale for scaling. (For example, Brooks et al. [41] used the displacement thickness as a length scale of the other mechanisms of airfoil self-noise.)

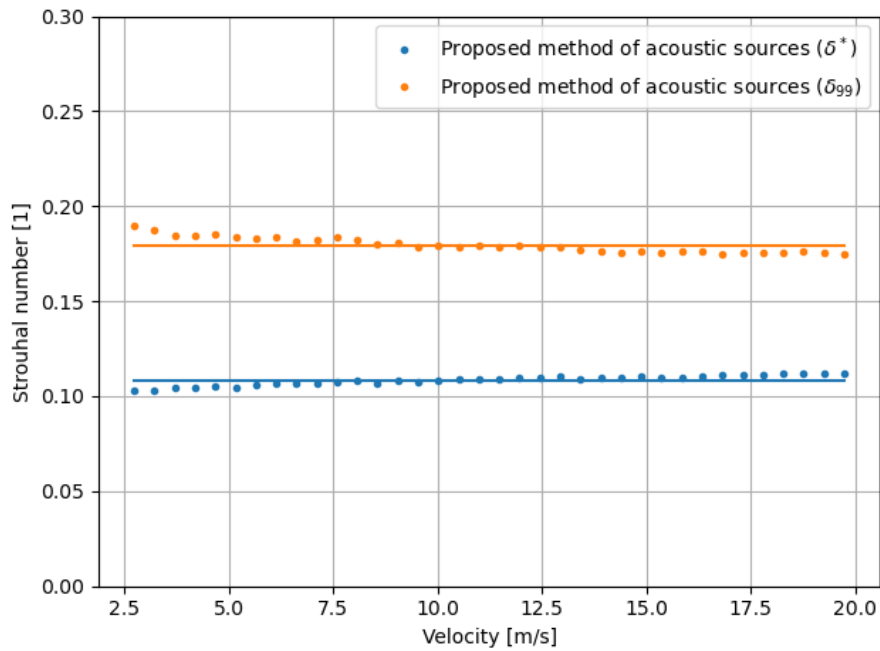


Figure 6.4: Dominant tones' Strouhal number based on two different length scales: the displacement thickness δ^* and the conventional thickness δ_{99} .

In Fig. 6.4, a comparison of the Strouhal numbers with two different length scales is shown. Using the displacement thickness, the mean value of the Strouhal number is 0.1, which is half the well-known Strouhal number 0.2 of vortex shedding behind bluff bodies [44].

There is no definite answer to the question of which length scale should be used for frequency scaling of the laminar boundary-layer instability noise. The conventional thickness is more closely related to the size of the acoustic source, while the displacement thickness is more closely related to the position of the strongest acoustic source (see Fig. 4.13).

6.2 Acoustic Feedback

The secondary results of the measurements presented in Chapter 5 are the differences between the dominant frequency and its secondary frequencies, which are generated by the acoustic feedback loop proposed notably by Arbey et al. [47]. The measured frequency differences are shown in Table 6.2. For low velocities, it was not possible to determine these results, and for the velocities above $20 \text{ m} \cdot \text{s}^{-1}$, the convective velocity is not known due to the presence of a turbulent boundary layer in the computational model. For further evaluation of the acoustic feedback, it is necessary to obtain the convective velocity of the instability, which is not possible with the present model in the case of a turbulent boundary layer.

Table 6.2: Measured difference Δf between the peak frequency and secondary frequency.

$U_\infty [\text{m} \cdot \text{s}^{-1}]$	$\Delta f [\text{Hz}]$	$U_\infty [\text{m} \cdot \text{s}^{-1}]$	$\Delta f [\text{Hz}]$
7.59	97	15.36	183
8.08	112	15.84	190
8.56	121	16.33	197
9.05	131	16.81	202
9.53	139	17.30	207
10.02	147	17.79	212
13.42	157	18.27	143
13.90	164	18.76	146
14.39	170	19.24	151
14.87	177	19.73	150

Equation (4.42) can be used to find an empirical value for the feedback length based on the measured Δf and the convective velocity c_r obtained as an average value between the point of the first occurrence of the unstable linear perturbation and the trailing edge. The predicted numerical values of the convective velocity are shown in Appendix B.3.

As was stated in Section 4.5, there are multiple theories about the determination of the acoustic feedback length. In Fig. 6.5, empirical values of the feedback length are presented based on the method proposed in Section 4.5. For comparison, the distance from the first occurrence of an instability in the boundary layer to the trailing edge is shown with blue dots. For cases with freestream velocity below $10 \text{ m} \cdot \text{s}^{-1}$, the experimentally obtained value of the feedback length is close to the proposed theoretical distance based on the occurrence of the first instability. In the range from $10.50 \text{ m} \cdot \text{s}^{-1}$ to $12.93 \text{ m} \cdot \text{s}^{-1}$, it was not possible to determine the secondary tones from the measured spectra. In the second part of this diagram, between velocities $13.42 \text{ m} \cdot \text{s}^{-1}$ and $17.79 \text{ m} \cdot \text{s}^{-1}$, the experimentally obtained value of the feedback length is approximately 6–7% of the chord length higher than the distance from the point of the first instability to the trailing edge. In the last obtained range of velocities between $18.27 \text{ m} \cdot \text{s}^{-1}$ and $19.73 \text{ m} \cdot \text{s}^{-1}$, the

feedback length is predicted to be approximately 55 % of the chord length.

Although XFOIL predicts (with $N_{\text{crit}} = 11$) the transition to the turbulent boundary layer for velocities above $20 \text{ m} \cdot \text{s}^{-1}$, it should be assumed that the transition in the experiment occurs at a lower velocity. It can be theorized that the change in feedback length could be a footprint of the boundary-layer transition.

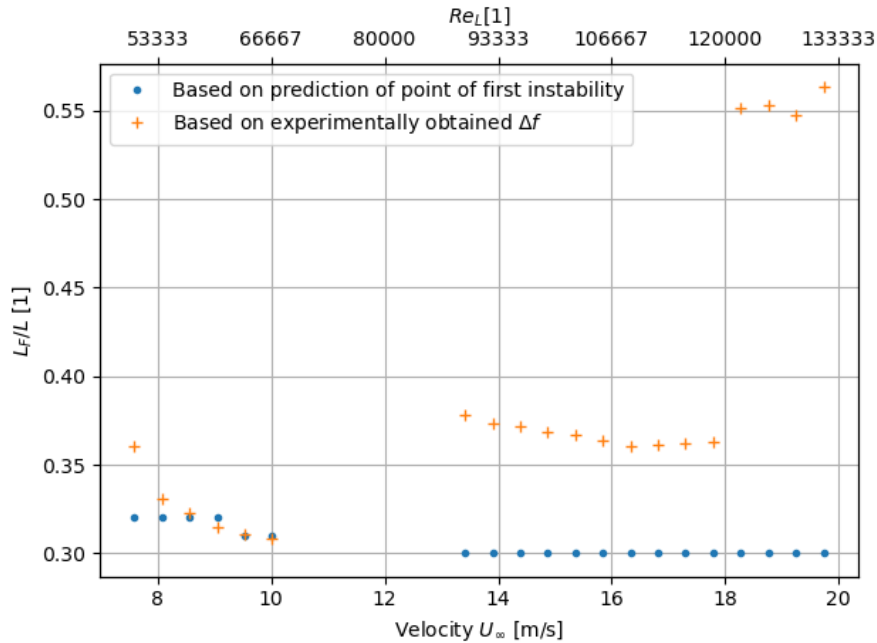



Figure 6.5: Feedback length based on experimentally obtained Δf and the theoretical feedback length, which is equal to the distance from the first occurrence of instability to the trailing edge.

Certainly, a possible direction for future work would be to investigate and validate the acoustic feedback with greater precision. This would require a specialized aeroacoustic facility to minimize contamination of the measured data with the background acoustic noise of the running wind tunnel. Measurements in such a facility could provide clearer information about the secondary tones and thus the Δf value used in the formula for the empirical prediction. This acoustic feedback could be used to develop a non-intrusive way of examining the boundary-layer state.



Chapter 7

Conclusions

This thesis is focused on fundamental research into the aeroacoustic characteristics of boundary-layer regimes. In the first part of the thesis, the main nomenclature and fundamental theory of fluid dynamics are introduced, followed by a literature survey and the goals of the thesis regarding the acoustic noise generated by linear instability in the boundary layer. The second part of the thesis first develops the relevant theory, including a novel theoretical model, then validates the proposed model using experimental results.

The novel theoretical model is based on the linear instability theory. The solution of the Orr–Sommerfeld equation is used to determine the acoustic source field of one mode within the boundary layer. Then, a method of comparison of acoustic fields for different frequencies is developed. The proposed model is compared with the solution of the method of maximal amplification of Tollmien–Schlichting waves.

For the experimental validation of the proposed theoretical model, a measurement method was established. Since it was not possible to use a specialized aeroacoustic facility (i.e., a wind tunnel with an anechoic chamber as a test section), a substitute method was proposed. This was based on measurements with electret microphones built into the surface of a test segment of a NACA 0012 airfoil. This airfoil was chosen as it offered the strongest prospects of comparing the theoretical and experimental results with the empirical model of Brooks, Pope, and Marcolini [41].

The experimental investigation showed that it is possible to obtain reliable results for the tonal noise even though there is a stronger background noise in the running wind tunnel. For the reference measurement, two microphones were placed outside the open test section of the wind tunnel. Since some of the measured tones were also detectable by the reference microphones, they were also used to confirm the measured main tones.

The proposed model of acoustic sources was successfully validated against the obtained experimental data. Furthermore, the proposed model was compared with the BPM empirical method. Regarding the results obtained using the theoretical method of acoustic sources, the characteristic length of the Strouhal number was discussed. The proposed model predicts a constant Strouhal number for the dominant-frequency solution with either the conventional or displacement boundary-layer thickness as a characteristic

length. When using the conventional boundary-layer thickness, the Strouhal number of the laminar boundary-layer instability noise is 0.18, whereas when using the displacement thickness, the Strouhal number of the dominant tone is 0.1. The result with the displacement thickness is rather interesting because it is half the well-known Strouhal number of the vortex shedding of a bluff body (e.g., a cylinder).

The experimental results were also used to analyze the acoustic feedback length. It was possible to obtain this quantity; however, it is rather difficult to compare these results. The feedback length (and the acoustic feedback overall) could be investigated in more detail in some future work using a different experimental approach in an aeroacoustic facility. For example, with a higher sampling rate, the phase delay between measurement points could be investigated; however, effort must be taken to prevent the results from being contaminated with the background noise and echoes.

7.1 Application of the Thesis Results

The main result of this thesis is an acoustic source model of the boundary-layer instability noise. This noise is essentially tonal noise, which is quite annoying for humans. The model could be used as the core of a computational software package for boundary-layer noise. The model could also be extended to an airfoil under an arbitrary angle of attack and then used as a part of a more complex computational approach to predict the noise of an arbitrary airfoil. This would bring the benefit of predicting the tonal noise, which could be used in an optimization process to avoid undesirable tones.

7.2 Brief Summary of the Thesis Objectives

Recalling the objectives of the thesis in Section 3.3, the following hypothesis was stated:

In a laminar boundary-layer regime, the acoustic source is created by a velocity perturbation. If the perturbation is assumed to be of a single mode, the linear Orr–Sommerfeld equation can be used to estimate the acoustic source term of Lighthill’s equation for the boundary layer to obtain the peak tone emitted by the laminar boundary layer.

This hypothesis was confirmed by successfully achieving the constituent thesis objectives:

- *Description of the aeroacoustic footprint of a boundary layer experiencing linear instabilities in a laminar regime before the transition to a turbulent regime*
 - *Theoretical description of the aeroacoustic sources caused by linear instabilities in the boundary layer*

A theoretical model of point acoustic sources (Eq. (4.33) and Eq. (4.39)) has been established.

- *Proposal of a frequency model for the prediction of laminar boundary-layer instability noise*

A tonal noise model has been proposed in Section 4.4.1.

- *Experimental investigation of the boundary-layer instability noise*

- *Design of an experiment to validate the obtained theoretical results*

The proposed experimental approach to obtaining tonal noise frequencies in a non-aeroacoustic facility is described in Section 5.

- *Further examination of the experimental data—the using the experimental data to determine the acoustic feedback length*

The experimental data were studied further. The ladder structure (in Fig. 6.3) is observed, and these results were utilized to obtain the acoustic feedback length, which was compared to the distance from the first occurrence of an instability to the trailing edge in Section 6.2.

- *Validation of the proposed model and experimental results*

- *Validation of the proposed theoretical frequency model and experimental results on the NACA 0012 airfoil with the empirical model*

An overall comparison of the proposed theoretical model with experimentally obtained data is presented in Section 6.1.2 together with a comparison to the BPM empirical model.

The initial hypothesis is confirmed. It is possible to use the linear Orr–Sommerfeld equation to estimate the source of Lighthill’s equation to estimate the peak frequency of the laminar boundary-layer instability noise.

The most important contribution of this thesis is the validated model of the acoustic sources of the laminar boundary layer instability noise, formulated in Section 4.4.

■ 7.3 Future Work

In the present work, the main focus was on the boundary layer as an acoustic source. Future work should combine these findings with other measured boundary-layer parameters (e.g., the boundary-layer thickness). This should lead to further confirmation of the proposed model of acoustic sources.

The proposed model could also be extended with a (perhaps empirical) model of the behavior of the linear instabilities when they reach the part of the boundary layer in the turbulent state. The impact of the linear instability noise on the overall noise in the presence of turbulent boundary-layer noise could be investigated.

Another extension of the proposed model of acoustic sources could be based on estimating the magnitude of the initial velocity perturbation. With this

estimation and by taking into account the presence of the solid surface, it should be possible to evaluate the emitted sound in the far field and determine whether it is audible.

Other future work could focus on acoustic feedback. It was mentioned at the end of the previous chapter that acoustic feedback has been theoretically proposed, but experimental data are lacking. Therefore, a new set of experimental data would be useful. The possible connection between the state of the boundary layer and the acoustic feedback length could also be explored.



Bibliography

- [1] H. Schlichting, *Boundary-Layer Theory*. McGraw-Hill Series in Mechanical Engineering, New York: McGraw-Hill, 7th ed., 1979.
- [2] M. Lighthill, “On sound generated aerodynamically I. General theory,” *Proceedings of the Royal Society of London. Series A. Mathematical and Physical Sciences*, vol. 211, pp. 564–587, Mar. 1952.
- [3] M. Lighthill, “On sound generated aerodynamically II. Turbulence as a source of sound,” *Proceedings of the Royal Society of London. Series A. Mathematical and Physical Sciences*, vol. 222, pp. 1–32, Feb. 1954.
- [4] N. Curle, “The influence of solid boundaries upon aerodynamic sound,” *Proceedings of the Royal Society of London. Series A. Mathematical and Physical Sciences*, vol. 231, pp. 505–514, Sept. 1955.
- [5] J. Ffowcs Williams and D. Hawkings, “Sound generation by turbulence and surfaces in arbitrary motion,” *Philosophical Transactions of the Royal Society of London. Series A, Mathematical and Physical Sciences*, vol. 264, pp. 321–342, May 1969.
- [6] B. R. Munson, T. H. Okiishi, and W. W. Huebsch, *Fundamentals of Fluid Mechanics*. Hoboken, NJ: J. Wiley & Sons, 6th ed., 2009.
- [7] R. J. Blackwell, “Descartes’ Laws of Motion,” *Isis*, vol. 57, pp. 220–234, July 1966.
- [8] I. Newton, *Philosophiæ Naturalis Principia Mathematica*. London: Royal Society of London, 1687.
- [9] G. Emanuel, *Analytical Fluid Dynamics, Third Edition*. CRC Press, Nov. 2015.
- [10] H. Lamb, *Hydrodynamics*. Cambridge: Cambridge University Press, 1895.
- [11] ISO Central Secretary, “Standard Atmosphere,” Standard ISO 2533:1975, International Organization for Standardization, May 1975.

- [12] S. A. L. Glegg and W. Devenport, *Aeroacoustics of Low Mach Number Flows: Fundamentals, Analysis, and Measurement*. London: Academic Press, 2017.
- [13] C. Pozrikidis, *Fluid Dynamics*. Boston, MA: Springer US, 2017.
- [14] H. Tennekes and J. L. Lumley, *A First Course in Turbulence*. The MIT Press, 1972.
- [15] O. Reynolds, “IV. On the dynamical theory of incompressible viscous fluids and the determination of the criterion,” *Philosophical Transactions of the Royal Society of London. (A.)*, vol. 186, pp. 123–164, Dec. 1895.
- [16] J. H. Ferziger and M. Perić, *Computational Methods for Fluid Dynamics*. Berlin: Springer, 3rd ed., 2002.
- [17] F. H. Harlow, “Turbulence Transport Equations,” *Physics of Fluids*, vol. 10, no. 11, p. 2323, 1967.
- [18] K. Hanjalić and B. E. Launder, “A Reynolds stress model of turbulence and its application to thin shear flows,” *Journal of Fluid Mechanics*, vol. 52, pp. 609–638, Apr. 1972.
- [19] J. A. D. Ackroyd, B. P. Axcell, and A. I. Ruban, *Early Developments of Modern Aerodynamics*. Reston, VA: AIAA, Butterworth-Heinemann, 2001.
- [20] J. D. Anderson, “Ludwig Prandtl’s Boundary Layer,” *Physics Today*, vol. 58, pp. 42–48, Dec. 2005.
- [21] H. Schlichting and K. Gersten, *Boundary-Layer Theory*. Berlin, Heidelberg: Springer, 2017.
- [22] J. D. Anderson, *Fundamentals of Aerodynamics*. McGraw-Hill Series in Aeronautical and Aerospace Engineering, New York: McGraw-Hill, 2nd ed., 1991.
- [23] J. Persh, “A Study of Boundary-Layer Transition From Laminar to Turbulent Flow,” tech. rep., Defense Technical Information Center, Fort Belvoir, VA, Nov. 1956.
- [24] M. M. O’Meara and T. J. Mueller, “Laminar separation bubble characteristics on an airfoil at low Reynolds numbers,” *AIAA Journal*, vol. 25, pp. 1033–1041, Aug. 1987.
- [25] M. Drela, “XFOIL: An Analysis and Design System for Low Reynolds Number Airfoils,” in *Low Reynolds Number Aerodynamics* (T. J. Mueller, ed.), vol. 54, pp. 1–12, Berlin, Heidelberg: Springer, 1989.
- [26] V. Falkner and S. Skan, “LXXXV. *Solutions of the boundary-layer equations,*” *The London, Edinburgh, and Dublin Philosophical Magazine and Journal of Science*, vol. 12, pp. 865–896, Nov. 1931.

- [27] F. M. White, *Viscous Fluid Flow*. McGraw-Hill Series in Mechanical Engineering, New York, NY: McGraw-Hill Higher Education, 3rd ed., 2006.
- [28] D. R. Hartree, “On an equation occurring in Falkner and Skan’s approximate treatment of the equations of the boundary layer,” *Mathematical Proceedings of the Cambridge Philosophical Society*, vol. 33, pp. 223–239, Apr. 1937.
- [29] F. M. White, *Fluid Mechanics*. McGraw-Hill Series in Mechanical Engineering, New York, NY: McGraw-Hill, 7th ed., 2011.
- [30] P. J. Schmid and D. S. Henningson, *Stability and Transition in Shear Flows*. No. 142 in Applied Mathematical Sciences, New York: Springer, 2001.
- [31] H. Horton, “A Semi-Empirical Theory for the Growth and Bursting of Laminar Separation Bubbles,” Tech. Rep. ARC/CP-1073, Aeronautical Research Council, 1967.
- [32] A. Dovgal, V. Kozlov, and A. Michalke, “Laminar boundary layer separation: Instability and associated phenomena,” *Progress in Aerospace Sciences*, vol. 30, pp. 61–94, Jan. 1994.
- [33] L. E. Kinsler, ed., *Fundamentals of Acoustics*. New York: Wiley, 4th ed., 2000.
- [34] M. E. Goldstein, *Aeroacoustics*. Washington, D.C.: NASA, 1974.
- [35] A. Powell, “Theory of Vortex Sound,” *The Journal of the Acoustical Society of America*, vol. 36, pp. 177–195, Jan. 1964.
- [36] M. S. Howe, *Theory of Vortex Sound*. Cambridge University Press, 1st ed., Oct. 2002.
- [37] I. Proudman, “The generation of noise by isotropic turbulence,” *Proceedings of the Royal Society of London. Series A. Mathematical and Physical Sciences*, vol. 214, pp. 119–132, Aug. 1952.
- [38] G. M. Lilley, “The radiated noise from isotropic turbulence,” *Theoretical and Computational Fluid Dynamics*, vol. 6, pp. 281–301, Oct. 1994.
- [39] W. C. Meecham, “Surface and Volume Sound from Boundary Layers,” *The Journal of the Acoustical Society of America*, vol. 37, pp. 516–522, Mar. 1965.
- [40] A. Powell, “Aerodynamic Noise and the Plane Boundary,” *The Journal of the Acoustical Society of America*, vol. 32, pp. 982–990, Aug. 1960.
- [41] F. Brooks, D. Pope, and A. Marcolini, *Airfoil Self-Noise and Prediction*. NASA Reference Publication, NASA, July 1989.

- [42] S. Glegg, S. Verma, and L. Denissova, “The Relationship Between Surface Pressure Spectra and Vorticity in a Turbulent Boundary Layer,” Aug. 2022.
- [43] M. T. Landahl, “Wave mechanics of boundary layer turbulence and noise,” *The Journal of the Acoustical Society of America*, vol. 57, pp. 824–831, Apr. 1975.
- [44] R. W. Paterson, P. G. Vogt, M. R. Fink, and C. L. Munch, “Vortex Noise of Isolated Airfoils,” *Journal of Aircraft*, vol. 10, pp. 296–302, May 1973.
- [45] C. K. W. Tam, “Discrete tones of isolated airfoils,” *The Journal of the Acoustical Society of America*, vol. 55, pp. 1173–1177, June 1974.
- [46] R. Longhouse, “Vortex shedding noise of low tip speed, axial flow fans,” *Journal of Sound and Vibration*, vol. 53, pp. 25–46, July 1977.
- [47] H. Arbey and J. Bataille, “Noise generated by airfoil profiles placed in a uniform laminar flow,” *Journal of Fluid Mechanics*, vol. 134, p. 33, Sept. 1983.
- [48] M. R. Fink, “Prediction of airfoil tone frequencies,” *Journal of Aircraft*, vol. 12, pp. 118–120, Feb. 1975.
- [49] M. Lawson, S. Fiddes, and E. Nash, “Laminar boundary layer aeroacoustic instabilities,” in *32nd Aerospace Sciences Meeting and Exhibit*, (Reno, NV), American Institute of Aeronautics and Astronautics, Jan. 1994.
- [50] E. C. Nash, M. V. Lawson, and A. McAlpine, “Boundary-layer instability noise on aerofoils,” *Journal of Fluid Mechanics*, vol. 382, pp. 27–61, Mar. 1999.
- [51] A. McAlpine, E. Nash, and M. Lawson, “On the Generation of Discrete Frequency Tones by the Flow around an Aerofoil,” *Journal of Sound and Vibration*, vol. 222, pp. 753–779, May 1999.
- [52] G. Desquesnes, M. Terracol, and P. Sagaut, “Numerical investigation of the tone noise mechanism over laminar airfoils,” *Journal of Fluid Mechanics*, vol. 591, pp. 155–182, Nov. 2007.
- [53] M. J. Kingan and J. R. Pearse, “Laminar boundary layer instability noise produced by an aerofoil,” *Journal of Sound and Vibration*, vol. 322, pp. 808–828, May 2009.
- [54] B. Plogmann, A. Herrig, and W. Würz, “Experimental investigations of a trailing edge noise feedback mechanism on a NACA 0012 airfoil,” *Experiments in Fluids*, vol. 54, p. 1480, May 2013.

- [55] T. Chong, P. Joseph, and M. Kingan, “An investigation of airfoil tonal noise at different Reynolds numbers and angles of attack,” *Applied Acoustics*, vol. 74, pp. 38–48, Jan. 2013.
- [56] T. P. Chong and P. F. Joseph, “An experimental study of airfoil instability tonal noise with trailing edge serrations,” *Journal of Sound and Vibration*, vol. 332, pp. 6335–6358, Nov. 2013.
- [57] V. V. Golubev, L. Nguyen, R. R. Mankbadi, M. Roger, and M. R. Visbal, “On Flow-Acoustic Resonant Interactions in Transitional Airfoils,” *International Journal of Aeroacoustics*, vol. 13, pp. 1–38, Apr. 2014.
- [58] S. Pröbsting, J. Serpieri, and F. Scarano, “Experimental investigation of aerofoil tonal noise generation,” *Journal of Fluid Mechanics*, vol. 747, pp. 656–687, May 2014.
- [59] S. Pröbsting, F. Scarano, and S. C. Morris, “Regimes of tonal noise on an airfoil at moderate Reynolds number,” *Journal of Fluid Mechanics*, vol. 780, pp. 407–438, Oct. 2015.
- [60] S. Pröbsting and S. Yarusevych, “Laminar separation bubble development on an airfoil emitting tonal noise,” *Journal of Fluid Mechanics*, vol. 780, pp. 167–191, Oct. 2015.
- [61] E. Arcondoulis, C. J. Doolan, A. C. Zander, L. A. Brooks, and Y. Liu, “An investigation of airfoil dual acoustic feedback mechanisms at low-to-moderate Reynolds number,” *Journal of Sound and Vibration*, vol. 460, p. 114887, Nov. 2019.
- [62] M. B. R. Gelot and J. W. Kim, “Effect of serrated trailing edges on aerofoil tonal noise,” *Journal of Fluid Mechanics*, vol. 904, p. A30, Dec. 2020.
- [63] P. Jaiswal, Y. Pasco, G. Yakhina, and S. Moreau, “Experimental investigation of aerofoil tonal noise at low Mach number,” *Journal of Fluid Mechanics*, vol. 932, p. A37, Feb. 2022.
- [64] S. Redonnet and T. G. Schmidt, “Experimental investigation of the laminar boundary layer vortex-shedding noise by an airfoil within a closed-vein wind tunnel,” *International Journal of Aeroacoustics*, vol. 21, pp. 658–683, Nov. 2022.
- [65] J. E. Ffowcs Williams and L. H. Hall, “Aerodynamic sound generation by turbulent flow in the vicinity of a scattering half plane,” *Journal of Fluid Mechanics*, vol. 40, p. 657, Mar. 1970.
- [66] D. M. Chase, “Sound Radiated by Turbulent Flow off a Rigid Half-Plane as Obtained from a Wavevector Spectrum of Hydrodynamic Pressure,” *The Journal of the Acoustical Society of America*, vol. 52, pp. 1011–1023, Sept. 1972.

- [67] C. K. W. Tam, “Intensity, spectrum, and directivity of turbulent boundary layer noise,” *Journal of the Acoustic Society of America*, vol. 57, no. 1, p. 11, 1975.
- [68] R. Amiet, “Acoustic radiation from an airfoil in a turbulent stream,” *Journal of Sound and Vibration*, vol. 41, pp. 407–420, Aug. 1975.
- [69] R. Amiet, “Noise due to turbulent flow past a trailing edge,” *Journal of Sound and Vibration*, vol. 47, pp. 387–393, Aug. 1976.
- [70] R. H. Schlinker and R. Amiet, “Helicopter rotor trailing edge noise,” NASA Contractor Report NASA-CR-3470, NASA, Nov. 1981.
- [71] O. Marsden, C. Bogey, and C. Bailly, “Direct Noise Computation of the Turbulent Flow Around a Zero-Incidence Airfoil,” *AIAA Journal*, vol. 46, pp. 874–883, Apr. 2008.
- [72] J. Berland and X. Gloerfelt, “Investigation of noise radiation from a turbulent boundary layer,” in *14th AIAA/CEAS Aeroacoustics Conference (29th AIAA Aeroacoustics Conference)*, (Vancouver, British Columbia, Canada), American Institute of Aeronautics and Astronautics, May 2008.
- [73] X. Gloerfelt and J. Berland, “Direct Computation of Turbulent Boundary Layer Noise,” in *15th AIAA/CEAS Aeroacoustics Conference (30th AIAA Aeroacoustics Conference)*, (Miami, Florida), American Institute of Aeronautics and Astronautics, May 2009.
- [74] X. Gloerfelt and J. Berland, “Turbulent boundary-layer noise: Direct radiation at Mach number 0.5,” *Journal of Fluid Mechanics*, vol. 723, pp. 318–351, May 2013.
- [75] W. J. Devenport, D. L. Grissom, W. Nathan Alexander, B. S. Smith, and S. A. Glegg, “Measurements of roughness noise,” *Journal of Sound and Vibration*, vol. 330, pp. 4250–4273, Aug. 2011.
- [76] Y. C. Küçüksoman, J. Christophe, and C. Schram, “Trailing edge noise prediction based on wall pressure spectrum models for NACA0012 airfoil,” *Journal of Wind Engineering and Industrial Aerodynamics*, vol. 175, pp. 305–316, Apr. 2018.
- [77] S. A. Glegg, S. Verma, and L. Denissova, “Trailing Edge Noise Prediction Based on Solutions to the Orr Sommerfeld Equation,” in *28th AIAA/CEAS Aeroacoustics 2022 Conference*, (Southampton, UK), American Institute of Aeronautics and Astronautics, June 2022.
- [78] M. J. Kingan, *Aeroacoustic Noise Produced by an Aerofoil*. PhD thesis, University of Canterbury, 2005.
- [79] K. Stewartson, “Further solutions of the Falkner-Skan equation,” *Mathematical Proceedings of the Cambridge Philosophical Society*, vol. 50, pp. 454–465, July 1954.

- [80] T. Cebeci and H. B. Keller, “Shooting and parallel shooting methods for solving the Falkner-Skan boundary-layer equation,” *Journal of Computational Physics*, vol. 7, pp. 289–300, Apr. 1971.
- [81] J. W. Christian, W. L. Hankey, and J. S. Petty, “Similar Solutions of the Attached and Separated Compressible Laminar Boundary Layer with Heat Transfer and Pressure Gradient,” tech. rep., Aerospace Research Laboratories, US Air Force, Feb. 1970.
- [82] T. Bridges and P. Morris, “Differential eigenvalue problems in which the parameter appears nonlinearly,” *Journal of Computational Physics*, vol. 55, pp. 437–460, Sept. 1984.
- [83] G. Danabasoglu and S. Biringen, “A Chebyshev matrix method for the spatial modes of the Orr-Sommerfeld equation,” *International Journal for Numerical Methods in Fluids*, vol. 11, pp. 1033–1037, Nov. 1990.
- [84] W. Huang and D. M. Sloan, “The Pseudospectral Method for Solving Differential Eigenvalue Problems,” *Journal of Computational Physics*, vol. 111, pp. 399–409, Apr. 1994.
- [85] L. N. Trefethen, *Spectral Methods in Matlab*. SIAM, 2000.
- [86] S. A. Orszag, “Accurate solution of the Orr–Sommerfeld stability equation,” *Journal of Fluid Mechanics*, vol. 50, pp. 689–703, Dec. 1971.
- [87] J. Dongarra, B. Straughan, and D. Walker, “Chebyshev tau-QZ algorithm methods for calculating spectra of hydrodynamic stability problems,” *Applied Numerical Mathematics*, vol. 22, pp. 399–434, Dec. 1996.
- [88] H. Haj-Hariri, “Transformations reducing the order of the parameter in differential eigenvalue problems,” *Journal of Computational Physics*, vol. 77, pp. 472–484, Aug. 1988.
- [89] R. Jordinson, “The flat plate boundary layer. Part 1. Numerical integration of the Orr–Sommerfeld equation,” *Journal of Fluid Mechanics*, vol. 43, pp. 801–811, Oct. 1970.
- [90] C. Gleyzes, J. Cousteix, and J. Bonnet, “Theoretical And Experimental Study Of Low Reynolds Number Transitional Separation Bubbles,” in *Proceedings of the Conference on Low Reynolds Number Airfoil Aerodynamics*, pp. 137–152, The University Of Notre Dame, June 1985.
- [91] M. Drela and M. B. Giles, “Viscous-inviscid analysis of transonic and low Reynolds number airfoils,” *AIAA Journal*, vol. 25, pp. 1347–1355, Oct. 1987.
- [92] O. Gunel, E. Koc, and T. Yavuz, “CFD vs. XFOIL of airfoil analysis at low Reynolds numbers,” in *2016 IEEE International Conference on Renewable Energy Research and Applications (ICRERA)*, (Birmingham, United Kingdom), pp. 628–632, IEEE, Nov. 2016.

- [93] N. A. Jaffe, T. T. Okamura, and A. M. O. Smith, “Determination of Spatial Amplification Factors and Their Application to Predicting Transition,” *AIAA Journal*, vol. 8, pp. 301–308, Feb. 1970.
- [94] G. Schubauer and H. Skramstad, “Laminar boundary-layer oscillations and transition on a flat plate,” *Journal of Research of the National Bureau of Standards*, vol. 38, p. 251, Feb. 1947.
- [95] S. V. Vaseghi, *Advanced Digital Signal Processing and Noise Reduction*. Chichester, U.K.: J. Wiley & Sons, 4th ed., 2008.
- [96] “CMC-4015-25L100 Datasheet - Electret Condenser Microphones,” Jan. 2020.
- [97] P. Welch, “The use of fast Fourier transform for the estimation of power spectra: A method based on time averaging over short, modified periodograms,” *IEEE Transactions on Audio and Electroacoustics*, vol. 15, pp. 70–73, June 1967.
- [98] O. M. Solomon, Jr., “PSD computations using Welch’s method. [Power Spectral Density (PSD)],” Tech. Rep. SAND-91-1533, 5688766, Sandia National Laboratories, Albuquerque, NM, USA, Dec. 1991.



Author's References

- [A1] Jakub Suchý. On prediction of laminar boundary vortex shedding noise. *AIP Conference Proceedings*, 2672(1):020019, February 2023. ISSN 0094-243X. <http://dx.doi.org/10.1063/5.0120026>.
- [A2] Vladimir Kulish, Jiří Nožička, and Jakub Suchý. A non-field analytical method for solving problems in aero-acoustics. *Scientific Reports*, 10(1):19688, December 2020. ISSN 2045-2322. <http://dx.doi.org/10.1038/s41598-020-76687-x>.
- [A3] Jakub Suchý. Measurement analysis of aerodynamic noise in low speed wind tunnel. *AIP Conference Proceedings*, 2118(1):030042, June 2019. ISSN 0094-243X. <http://dx.doi.org/10.1063/1.5114770>.
- [A4] Jakub Suchý, Jiří Nožička, and Václav Papež. Experimental Investigation of Unsteady Static Pressure Field Behind a Circular Cylinder. *EPJ Web of Conferences*, 269:01059, 2022. ISSN 2100-014X. <http://dx.doi.org/10.1051/epjconf/202226901059>.
- [A5] Jakub Suchý and Tomáš Hyhlík. Measurement of the Boundary Layer Surface Pressure Fluctuations Spectrum using Electret Microphones. In *Proceedings of the International Conference Experimental Fluid Mechanics 2022*, Dvůr Králové nad Labem, Czech Republic, November 2022.

Appendix A

Derivation of the Basic Aeroacoustic Equations of the Boundary Layer

A.1 Derivation of Lighthill's Equation

Lighthill's equation is derived by taking the time derivative of the continuity equation (Eq. (2.1)),

$$\frac{\partial}{\partial t} \left(\frac{\partial \rho}{\partial t} + \frac{\partial(\rho v_i)}{\partial x_i} \right) = 0 \quad (\text{A.1})$$

and subtracting the divergence of the balance of momentum (Eq. (2.2)),

$$\frac{\partial}{\partial x_i} \left(\frac{\partial(\rho v_i)}{\partial x_i} + \frac{\partial(\rho v_i v_j + P_{ij})}{\partial x_j} \right) = 0 \quad (\text{A.2})$$

where $P_{ij} = p \cdot \delta_{ij} - \tau_{ij}$, resulting in

$$\frac{\partial^2 \rho}{\partial t^2} = \frac{\partial^2(v_i v_j \rho)}{\partial x_j \partial x_i} + \frac{\partial^2 P_{ij}}{\partial x_j \partial x_i} \quad (\text{A.3})$$

Based on Eq. (2.42), the time derivative of the density fluctuations ρ' is

$$\frac{\partial \rho'}{\partial t} = \frac{\partial \rho}{\partial t} \quad (\text{A.4})$$

Substituting Eq. (A.4) into Eq. (A.3) and subtracting $c_\infty^2 \frac{\partial^2 \rho'}{\partial x_i^2}$ from both sides of the equations leads to

$$\frac{\partial \rho'}{\partial t} - c_\infty^2 \frac{\partial^2 \rho'}{\partial x_i^2} = \frac{\partial^2(v_i v_j \rho)}{\partial x_j \partial x_i} + \frac{\partial^2 P_{ij}}{\partial x_j \partial x_i} - c_\infty^2 \frac{\partial^2 \rho'}{\partial x_i^2}$$

The last term can be rewritten in the following form with the Kronecker symbol:

$$\frac{\partial^2 \rho'}{\partial x_i^2} = \frac{\partial^2(\rho' \delta_{ij})}{\partial x_i \partial x_j}$$

The final equation is then

$$\frac{\partial \rho'}{\partial t} - c_\infty^2 \frac{\partial^2 \rho'}{\partial x_i^2} = \frac{\partial^2(v_i v_j \rho)}{\partial x_i \partial x_j} + \frac{\partial^2 P_{ij}}{\partial x_i \partial x_j} - c_\infty^2 \frac{\partial^2(\rho' \delta_{ij})}{\partial x_i \partial x_j} \quad (\text{A.5})$$

Lighthill's stress tensor is then defined (based on the right-hand side of Eq. (A.5)):

$$T_{ij} = \rho v_i v_j - \tau_{ij} + (p' - c_\infty^2 \rho') \cdot \delta_{ij} \quad (\text{A.6})$$

where p' is the pressure fluctuation relative to the surrounding pressure. Then Lighthill's equation is as follows:

$$\frac{\partial \rho'}{\partial t} - c_\infty^2 \frac{\partial^2 \rho'}{\partial x_i^2} = \frac{\partial^2 T_{ij}}{\partial x_i \partial x_j} \quad (\text{A.7})$$

■ A.2 Source Term for the Boundary Layer

The source term of Lighthill's equation is as follows:

$$\frac{\partial^2 T_{ij}}{\partial x_i \partial x_j} = \frac{\partial}{\partial x_i \partial x_j} \left(\rho v_i v_j - \tau_{ij} + (p' - c_\infty^2 \rho') \cdot \delta_{ij} \right) \quad (\text{A.8})$$

For isentropic flow (based on the definition of the speed of sound, Eq. (2.14)),

$$(p' - c_\infty^2 \rho') = 0 \quad (\text{A.9})$$

For incompressible fluid flow, $\rho = \rho_0$,

$$\frac{\partial^2 T_{ij}}{\partial x_i \partial x_j} = \rho_0 \frac{\partial^2 (v_i v_j)}{\partial x_i \partial x_j} - \frac{\partial^2 \tau_{ij}}{\partial x_i \partial x_j} \quad (\text{A.10})$$

For incompressible fluid flow (i.e., $\frac{\partial v_i}{\partial x_i} = 0$, based on Eq. (2.3)),

$$\frac{\partial^2 \tau_{ij}}{\partial x_i \partial x_j} = 0 \quad (\text{A.11})$$

For isentropic incompressible fluid flow, the source term of Lighthill's equation is

$$\frac{\partial^2 T_{ij}}{\partial x_i \partial x_j} = \rho_0 \frac{\partial^2 (v_i v_j)}{\partial x_i \partial x_j} \quad (\text{A.12})$$

The following identity can be used:

$$\frac{\partial^2 (v_i v_j)}{\partial x_i \partial x_j} = \frac{\partial v_j}{\partial x_i} \cdot \frac{\partial v_i}{\partial x_j} \quad (\text{A.13})$$

The decomposition of the velocity to the mean velocity and fluctuating velocity is

$$v_i = V_i + v'_i \quad (\text{A.14})$$

The assumptions for the two-dimensional flow of the boundary layer (the x_1 -axis is in the direction parallel to the flow and x_2 is in the direction normal to the wall) are as follows:

- $V_2 \ll V_1$: the mean velocity in the normal direction is negligible

- $V_1 = V_1(x_2)$, $\partial V_1 / \partial x_1 = 0$: the mean velocity in the parallel direction is a function only of x_2

Based on this analysis, the components of v_i are

$$v_1(x_1, x_2) = V_1(x_2) + v'_1(x_1, x_2) \quad (\text{A.15})$$

$$v_2(x_1, x_2) = v'_2(x_1, x_2) \quad (\text{A.16})$$

Using these substitutions, Eq. (A.12) can be written in the following form:

$$\frac{\partial^2 T_{ij}}{\partial x_i \partial x_j} = 2 \cdot \rho_0 \cdot \frac{\partial V_1}{\partial x_2} \cdot \frac{\partial v'_2}{\partial x_1} + \rho_0 \cdot \frac{\partial v'_j}{\partial x_i} \cdot \frac{\partial v'_i}{\partial x_j} \quad (\text{A.17})$$

Appendix B

Supplementary Results

B.1 Neutral Curve of the Blasius Boundary Layer

Table B.1 was generated using the method of solving the Orr–Sommerfeld equation described in Section 4.2. The table presents a fundamental comparison of the solution of the marginal stability problem (i.e., $c_i = 0$) of the Blasius boundary layer (i.e., the Falkner–Skan boundary layer with Hartree parameter $\beta = 0$), and shows the relative difference between the spatial stability and temporal stability solutions (for each root; for the given Reynolds numbers, there exist two roots for neutral stability—see Fig. 4.6 and Fig. 4.8). The number of Chebyshev collocation points (see Section 4.2.1) for this comparison was chosen to be 120.

Table B.1: Flat plate marginal stability solution

Re_{δ^*}	Spatial solution		Temporal solution		Relative difference	
	c [1]	c [1]	c [1]	c [1]	Diff. [%]	Diff. [%]
650	0.36239	0.39524	0.36296	0.39471	0.159	0.134
800	0.34180	0.38457	0.34217	0.38426	0.109	0.080
950	0.32662	0.37501	0.32690	0.37479	0.087	0.057
1100	0.31462	0.36667	0.31485	0.36651	0.074	0.043
1250	0.30476	0.35936	0.30496	0.35923	0.065	0.034
1400	0.29643	0.35289	0.29660	0.35279	0.059	0.028
1550	0.28925	0.34710	0.28940	0.34702	0.053	0.023
1700	0.28296	0.34188	0.28310	0.34182	0.049	0.019
1850	0.27739	0.33714	0.27752	0.33708	0.046	0.015
2000	0.27240	0.33279	0.27252	0.33275	0.042	0.013
2150	0.26789	0.32879	0.26800	0.32876	0.040	0.010
2300	0.26380	0.32509	0.26390	0.32506	0.038	0.008
2450	0.26004	0.32164	0.26014	0.32162	0.036	0.007
2600	0.25659	0.31842	0.25668	0.31841	0.034	0.005
2750	0.25339	0.31541	0.25347	0.31539	0.033	0.004
2900	0.25042	0.31257	0.25050	0.31256	0.032	0.002

B.2 Boundary-Layer Thickness

The boundary-layer thickness values at the trailing edge shown in Table B.2 were generated using XFOIL and the Falkner–Skan equation solver described in Section 4.1.1. The boundary-layer thickness was obtained only for the laminar boundary layer (i.e., where the Falkner–Skan velocity profile is applicable). The Reynolds number Re_L is defined as

$$Re_L = \frac{U_\infty \cdot L}{\nu}$$

where L is the chord length of the airfoil.

Table B.2: NACA 0012 boundary-layer thickness at the trailing edge.

Re_L	δ_{99}/L	δ^*/L	Re_L	δ_{99}/L	δ^*/L
18267	0.057175	0.031095	76533	0.034595	0.021164
21467	0.053797	0.029587	79733	0.034432	0.020989
24733	0.050428	0.028356	83000	0.033883	0.020823
27933	0.048361	0.027361	86200	0.033376	0.020672
31200	0.046617	0.026496	89467	0.033276	0.020529
34467	0.045166	0.025755	92667	0.032820	0.020398
37667	0.043422	0.025127	95933	0.032380	0.020273
40933	0.042397	0.024567	99133	0.032343	0.020159
44133	0.041026	0.024082	102400	0.031943	0.020049
47400	0.040279	0.023643	105600	0.031933	0.019949
50600	0.039652	0.023257	108867	0.031566	0.019854
53867	0.038606	0.022903	112067	0.031224	0.019766
57067	0.038138	0.022588	115333	0.031242	0.019682
60333	0.037255	0.022296	118600	0.030920	0.019603
63533	0.036458	0.022034	121800	0.030618	0.019530
66800	0.036142	0.021787	125067	0.030664	0.019461
70000	0.035451	0.021565	128267	0.030384	0.019397
73267	0.035214	0.021356	131533	0.030110	0.019336

Note: To obtain these results, the criterion for the natural transition of the boundary layer must be set to $N_{\text{crit}} = 11$.

B.3 Instability Noise Peak Frequency for NACA 0012

In the results listed in Tables B.3 and B.4, the velocity c_r is the average value of the convective velocity of the unstable modes between their initial occurrence and the trailing edge.

Table B.3: NACA 0012 prediction of peak frequencies based on the method of maximal amplitude growth and associated properties of the linear stability analysis.

U_∞ [m · s ⁻¹]	f_{peak} [Hz]	c_r/U_∞ [1]	U_∞ [m · s ⁻¹]	f_{peak} [Hz]	c_r/U_∞ [1]
2.74	67	0.453	11.48	486	0.434
3.22	83	0.450	11.96	513	0.434
3.71	102	0.449	12.45	541	0.433
4.19	121	0.448	12.93	569	0.432
4.68	142	0.447	13.42	595	0.431
5.17	163	0.446	13.90	623	0.430
5.65	185	0.445	14.39	652	0.430
6.14	207	0.444	14.87	681	0.429
6.62	230	0.443	15.36	710	0.429
7.11	253	0.441	15.84	739	0.428
7.59	277	0.441	16.33	769	0.428
8.08	302	0.440	16.81	798	0.427
8.56	328	0.439	17.30	828	0.426
9.05	352	0.438	17.79	858	0.426
9.53	378	0.437	18.27	887	0.425
10.02	404	0.436	18.76	918	0.425
10.50	431	0.436	19.24	947	0.424
10.99	458	0.435	19.73	978	0.424

Table B.4: NACA 0012 prediction of peak frequencies based on the method of acoustic sources (the method proposed in this thesis) and associated properties of linear stability analysis.

U_∞ [m · s ⁻¹]	f_{peak} [Hz]	c_r/U_∞ [1]	U_∞ [m · s ⁻¹]	f_{peak} [Hz]	c_r/U_∞ [1]
2.74	91	0.485	11.48	592	0.455
3.22	112	0.481	11.96	624	0.454
3.71	136	0.479	12.45	656	0.453
4.19	160	0.477	12.93	690	0.453
4.68	186	0.475	13.42	714	0.450
5.17	210	0.473	13.90	746	0.449
5.65	238	0.472	14.39	779	0.448
6.14	266	0.470	14.87	811	0.447
6.62	293	0.468	15.36	844	0.447
7.11	322	0.467	15.84	876	0.446
7.59	351	0.465	16.33	909	0.445
8.08	381	0.464	16.81	942	0.444
8.56	405	0.462	17.30	975	0.443
9.05	438	0.461	17.79	1011	0.443
9.53	467	0.459	18.27	1046	0.442
10.02	498	0.458	18.76	1079	0.441
10.50	529	0.457	19.24	1112	0.441
10.99	560	0.456	19.73	1146	0.440